Quantum fields and machine learning

by

Irene Melgarejo Lermas

A thesis
presented to the University of Waterloo
in fulfillment of the
thesis requirement for the degree of
Master of Mathematics
in
Applied Mathematics (Quantum Information)

Waterloo, Ontario, Canada, 2020

Author's Declaration

This thesis consists of material all of which I authored or co-authored: see Statement of Contributions included in the thesis. This is a true copy of the thesis, including any required final revisions, as accepted by my examiners

I understand that my thesis may be made electronically available to the public.

Statement of Contributions

Irene Melgarejo Lermas was the sole author for Chapters 1 and 5, which were written under the supervision of Dr Eduardo Martín-Martínez and were not written for publication. This thesis consists in part of one manuscript written for publication and one manuscript in preparation.

Research presented in Chapter 3:

Irene Melgarejo Lermas and Abhisek Sahu are the leading authors, under the supervision of Eduardo Martín-Martínez of a manuscript in preparation, "Cancelling the harvesting of correlations in QFT". Abhisek Sahu derived the density matrix for N detectors interacting in the field (Eq. (3.20)). The rest of the work was lead by Irene Melgarejo Lermas, in collaboration with Abhisek Sahu and supervised by Eduardo Martín-Martínez. All the figures in Chapter 3 were created by Irene Melgarejo Lermas.

Research presented in Chapters 2, 4 :

Daniel Grimmer and Irene Melgarejo are the leading authors, under the supervision of Eduardo Martín-Martínez of the manuscript [51]. The theory for this paper is derived jointly by Daniel Grimmer and Irene Melgarejo Lermas, supervised by Eduardo Martínez, and appears in Chapter 4 and in Sections 2.4, 2.5, 2.6 and 2.7 of Chapter 2. done in collaboration. The code for the neural network was written by Daniel Grimmer. Irene Melgarejo Lermas and Daniel Grimmer jointly wrote the code for the numerical simulation of probes interacting with the field. Figures 4.1, 4.5, 4.7 and 4.8 were created by Daniel Grimmer. The rest of the figures in Chapter 4 were created by Irene Melgarejo Lermas.

Abstract

In this thesis, we use detector models to study various properties of quantum fields. One such property is the correlations present in fields. It is known that two uncorrelated detectors, upon coupling to a quantum field, can become correlated, i.e. they harvest correlations from the field. In this work, we study the effect of the presence of extra detectors in correlation harvesting protocols. Our first main result is that a single *interloper* detector can sabotage the harvesting of classical and quantum correlations.

The second main result in this thesis is that machines can learn to extract different features of a quantum field by processing the outcomes of local probes. As proof-of-principle, we show how a neural network can distinguish field's boundary conditions, predict the temperature of a field and of how it can distinguish between a Fock state and a phase-averaged coherent state.

Acknowledgements

I would like to like to thank Eduardo Martín-Martínez for being an extremely supportive and encouraging supervisor. Thank you to my collaborators Daniel Grimmer and Abhisek Sahu, excellent researchers and fantastic human beings. It has been a pleasure to work with both of you.

I would also like to thank the members of the Barrio RQI, Nicholas Funai, Daniel Grimmer, Richard Lopp, Nick Olsen, Maria Papageorgiou, Rick Perche, José de Ramón Rivera, Nayeli Rodríguez, Erickson Tjoa and Bruno Torres for useful feedback in many occasions. In particular, I would like to thank Pipo for many useful discussions and coffee breaks. Thank you to Jeremy and Supratik who made going to the office something to look forward to.

Thank you to my family in Canada: Manjit, Júlia, Rahul, Nachiket, Aditya, Jeremy, Dahlia and Nikhil. I appreciate each one of you and you make me a better person. A special thank you to Júlia, the personification of light and laughter and the reason I first landed in Canada.

A big thank you to my brother, my dad and my mom, who have always been supportive and great role models. Finally, the biggest thank you to Nikhil for all his patience, love and care.

Dedication

To my parents.

Table of Contents

List of Figures

List of Tables

Chapter 1

Preamble

1.1 Layman intro to RQI and detector models

1.1.1 Non-relativistic quantum mechanics

The development of non-relativistic quantum mechanics (commonly called just "quantum mechanics") in the XX century provided a common explanation to very different, previously non-understood phenomena. The photoelectric effect [37], the ultraviolet catastrophe [103, 36] or the Stern-Gerlach experiment [46] could be explained with the apparent "wave-particle duality" of light[1], a key feature in quantum physics.

Quantum systems, like atoms or subatomic particles, were now treated probabilistically. That means that any property that could be measured, any *observable* (like position, velocity), would have different outcomes with different probabilities. Unlike in classical physics, you could not predict accurately where an electron would move next even if you knew its equation of motion and its position at some time before. Many scientists guessed that the cause of this bizarre feature of the theory was due to our ignorance about quantum systems. They thought that this was a similar situation to throwing a coin: since it is extremely challenging to take into account all the variables to predict its result, we perceive that there is a 50 per cent chance of the coin landing in its tail or head. "If we knew the direction and strength of the wind", they thought, "and we controlled very well

[1] Interestingly, the explanation of the photoelectric effect does not actually need quantization of light. It is enough to consider classical light and to quantize the energy levels of the electrons. We have included it in this list because Einstein originally used the "wave-particle duality" of light to explain the photoelectric effect.

the force we apply to the coin we could have a hundred per cent chance of getting it right every single time"[2].

However, it turned out that this weird probabilistic behaviour of quantum systems was not due to ignorance in our part. There were no *hidden local variables* to make this theory deterministic, as the Bell-inequalities experiments proved for different quantum systems [15, 16, 11].

The most "mainstream" interpretation (and still most taught [117]) of this quantum weirdness was the Copenhagen interpretation: "Before measuring a certain property of a quantum system, the system is in a *superposition*[3] of different states with different values for that property. After the measurement (also called *projective measurement*), the system property would suddenly have a definite value". This "sudden transformation" interpretation is a bit tricky, and many physicists just use these *projective measurements* as a useful piece of math to predict how the system will behave. However, many believe that not all these mathematical tools may necessarily have a counterpart in nature.

If all this was not weird enough yet, there is one more concept of this theory that even Einstein found spooky [38]: *quantum entanglement*. Two quantum systems are *entangled* when one system cannot be described independently of the other. It is a type of correlation that cannot be explained classically. To understand how mind-blowing entanglement is, imagine that we have two quantum systems that are maximally entangled. We keep one with us and send the other $1203km$ away. Then we measure an observable of the system we kept, which will have some outcome with some probability. With this result, we can predict immediately and *exactly* the observable of the other system. When we measure that other system, $1203km$ away[4], the result of the experiments will always be the one we had predicted, with probability 1, even if the outcome of the measurement was supposed to be probabilistic!

Because of all these quirks, quantum physics has been very successful. Apart from providing an explanation to the phenomena mentioned above, it predicted the internal structure of atoms, which were validated by many experiments [21]. New phases of matter predicted using this theory were found, like Bose-Einstein condensates [10] or quantum

[2]This has been done, by the way [32]. And yes, we physicists can control a non-quantum coin well enough to cheat every time!

[3]Mathematically, this superposition just expressed the different *probability amplitudes* for each of the values of the properties (or, equivalently, for the states that had those values). These "probability amplitudes" turned out to be a key concept in quantum mechanics. Instead of ranging from 0 to 1, like normal probabilities, they could be any complex number with norm equal or smaller than 1.

[4]This random number, $1203km$, has been the longest distance we have been able to maintain this entanglement between two photons [146].

droplets [25]. Recently there has been a notable increase in interest (and funding) in the field of Quantum Information and, in particular, Quantum Computing [69]. The combination of the concept of *probability amplitudes* and *entanglement* poses a risk to our current encryption protocols [116], but it also allows for safer communication [19] or for faster computations [12].

1.1.2 Relativity problem in quantum mechanics

However, as useful as quantum mechanics is, it still has a major problem: it is not compatible with Einstein's Special Relativity (that is why it is called non-relativistic quantum mechanics!). Special Relativity says that light moves at a constant speed, independent of the inertial observer, and nothing can go faster than the speed of light, not even information.

To understand Special Relativity we have to think of a very fast train travelling at 100 km/s. You are standing outside the train and your really fast friend, Menganito, is inside the train. If Menganito starts to run inside the train (in the same direction of the movement of the train) at 10 km/s, you, from the outside, will see that Menganito is moving at $100 + 10 = 110$ km/s. Well, it turns out that if Menganito were massless and moving inside the train at speed $c \simeq 300000$ km/s (that is the speed of light), from the outside, you would **not** see that Menganito is travelling at speed $c + 10$ km/s, you see that **Menganito is still moving exactly at $\mathbf{c \simeq 300000}$ km/s**.

This relativistic sum is at the heart of relativity, which is present in our everyday life, even if sometimes we are not aware of it. The relativistic correction has to be taken into account, for example, to study cosmology [71] and to have accurate GPS [13]. We do not normally perceive this relativistic correction because the speeds we are used to are way lower than the speed of light. In that regime that "relativistic sum" is almost identical to the "normal sum" of velocities we usually experience. So one may wonder now why we care about relativity in the quantum world. We are not dealing with rockets, satellites or galaxies, why do we have to take into account relativity? Because photons (the "particles"[5] of light that travel at speed c) *are* quantum objects. And photons are everywhere in the quantum world: atoms and other subatomic particles do not stop interacting with light. Atoms absorb or emit photons as their internal configuration changes [65]. So we need a theory that is quantum and relativistic at the same time because the objects that we study belong to both realms.

[5] In relativistic settings, even the notion of particles is challenged and many claim that the whole concept breaks down [101].

So what are the non-relativistic[6] features of the theory so far? For starters, the *projective measurement* assumption creates a problem with causality. The most important equations in quantum mechanics, the *Schrödinger equation*, is not *Lorentz*-invariant. That means that it is not compatible with that "relativistic sum" of velocities. Using the *Schrödinger equation* and that "relativistic sum" you predict a situation that is incompatible with the outcome of experiments. To solve this issue, Dirac proposed what is now called *Dirac equation*, which was Lorentz-invariant, and one of the first equations of relativistic quantum mechanics. However, this effort did not solve all incompatibilities between quantum mechanics and Relativity. For example, both Schrödinger and Dirac equations had ill-defined behaviours when trying to predict what happened in smaller and smaller spaces [55].

Then, it was evident that a new theory had to appear to fix these compatibility issues with relativity. Arguably, the most successful one to tackle these problems has been Quantum Field Theory.

1.1.3 Quantum field theory

Quantum field theory (QFT) developed around 30 years later than non-relativistic quantum mechanics. It started as a natural generalization of the electromagnetic field. In mathematics, a field is just a map that assigns some quantity (scalar, vector or, in general, a tensor) to each point of space. In particular, the classical electromagnetic field can be easily understood from a physical point of view: imagine there is an electron in empty space. Since it has a negative charge, it will repel any negatively charged particle (like another electron) and will attract any positively charged particle (for example, a proton). Also, the closer a charged particle is to this electron, the more significant the effect will be. These effects can be encoded by writing the strength and direction of the "attraction" or "repulsion" that a test particle (the one we use to record these numbers) suffers at each point in space. These numbers assigned to each point of space would be the field created by that electron. A general configuration of charged particles would also cause some electric and magnetic properties at each point of space, and these properties could be encoded in what is called the electromagnetic field.

Since the second half of the XIX century, physicists were aware that light was a periodically changing electromagnetic field. Light could, then, be understood mathematically as periodically changing magnetic and electric properties assigned to each point in space.

[6] I want to make a disclaimer here: the spooky property, *entanglement*, does not cause a problem with relativity. *Entanglement* does not allow faster-than-light communication. Even in relativistic theories, you will have *entanglement*!

And then, in the XX century, with quantum mechanics, physicists realized that light could be excitations of the field or *photons*, which have been called "particles" of light. So the first task for QFT was to modify the model for the electromagnetic field (*second quantize* it [7]) so that changes in the electromagnetic field would account for the *photons*. This result was the first success of QFT, and this specific line of research was called *Quantum Electrodynamics*.

The genius question in QFT was: "what if all the other particles (not just the photons) were also changes of some *other* unknown fields?". In this case, the fields could not be *caused* by particles, like the electromagnetic field was caused by the charged particles. In this theory, the fundamental objects of nature would be these *quantum fields*! This mathematical description was very elegant, but some problems persisted.

Physicists had found many divergences in their theory: some quantities that were known to be finite were now predicted to be infinite. Fortunately, in the 1950s, they were able to tame the tough mathematics that quantum field theory involved: *renormalization* [35, 142]. After applying this *renormalization theory*, QFT became a wildly successful theory. It predicted the existence of many particles that were later found in many "particle" accelerators [1]. And that is how now, the Standard Model (the theory that describes the known fundamental forces) includes an *electron* field, a *quark* field, a *muon* field, and so on, at least 17 of them!

Despite its great predictive power and its consistency with Special Relativity, Quantum Field Theory is not perfect. It breaks down near black holes and at large energies. Despite these drawbacks, it could still work, in theory, in most experimental setups. Unfortunately, there is still a significant hurdle linked to experimentation: how do we model the measuring process of the fields? We discussed before that the *projective measurement* prescription violated Special Relativity. So how do we translate this critical feature of quantum physics, those probabilistic outcomes, into quantum field theory?

1.1.4 Measurement problem in QFT

One way to find a measurement theory in QFT is to try and extend the framework in non-relativistic quantum mechanics. However this is not simple: local projective measurements on the field introduce ill-defined behaviour [99] and faster-than-light signalling [123, 34, 18]. In fact, it has been strongly argued that projective measurements should be rejected in any relativistic field theory [123].

[7] *First quantization* consisted on using quantum mechanics to describe electrons and atoms but still treat the electromagnetic field classically

But we still want to be able to measure quantum fields. Otherwise, how are we going be able to check our predictions experimentally? So we have to find a way to measure fields indirectly that obeys certain rules:

1. It is consistent with our theory and, in particular, relativity
2. Produces values that match experiments
3. Determines what happens after the measurement

One ingenious solution to tackle this problem is the use of detector models[8], which provide operational measurement protocols on the field and obeys the above-listed properties.

In this framework, a detector (also called a probe) is a system that can be described with non-relativistic quantum mechanics, for example, an atom. This probe interacts with the field for a while, and it collects some information about the field (just like a thermometer in a warm room gathers information about the temperature of the room). Then, to measure this non-relativistic probe, we can use *projective measurements* to obtain values from the probe (obeying rule 2). The whole evolution of the probe-field system can remain consistent with relativity [84, 85] (rule 1), even though the detector is a non-relativistic object. This measurement on the probe effectively induces what is called a *positive operator value measure* on the field (rule 3).

With detector models we have an operational prescription of how to measure interesting properties of the QFT: correlations among different parts of the field [137, 121, 22], negative energy densities [59] or entanglement [109, 110, 124, 81, 75, 112, 105, 86, 68, 111]. In particular in this thesis we consider the Unruh-DeWitt detector model, which allows for entanglement harvesting in different settings [109, 110, 124, 75, 112, 111] or quantum energy teleportation [66] or Unruh effect detection [136].

1.1.5 Relativistic Quantum Information

One may wonder why we should go through all this trouble to obtain a measurement theory for quantum field theory or why detector models are useful at all. Two of the main reasons to be interested in this area of relativistic quantum information (RQI):

[8] Alternatively, the *FV framework* has been proposed to tackle this local measurement problem using quantum fields to probe other fields [40].

1. **Fundamental research**: understanding quantum field theory is an important step to understand the fundamental properties of nature. With this theory, physicists have been able to predict the existence of new particles [1]. One important example was the prediction and detection of the Higgs Boson, which helped understand why particles have mass.

2. **Communication and computing**: In the section of non-relativistic mechanics, we talked about how we could use quantum properties, like entanglement or superposition, to find safe communication protocols and boost computations. In the same way, we could use these special properties of the quantum field (correlations and entanglement) for communication and computation.

Let us elaborate a little bit in the second argument. How can we use correlations or entanglement of quantum fields, and what does that even mean? Do we not need two different objects in order for us to talk about them being correlated, like the two photons at 1023 km example? The answer is no: the values of the field at different spacetime points can be correlated.

It seems weird, but think of it this way: if we throw a stone into a perfectly still pond, we will see a small circular wave travelling on the surface of the water. We recall that a field is just defined as some numbers associated with every position. In this case, the numbers we encode in our field are the heights of water at every position. The height of the water at time t will be the same at all of the points that are one meter away from the stone. Then, if we have the information of that height at one particular point at one meter away, we know the height of the water at any other point of a circle with a one-meter radius. In that sense, we can say that the field at one particular point is correlated to any other point situated at the same distance away from the stone. In a similar way, if we know the weight of the stone, we can predict how the height changes with time, we can say the height of the wave at a particular point at time t_1 and at another time t_2 are correlated.

Similarly, there can be correlations in a particular state (or configuration) of a quantum field. But then, how is that useful for computing or communication? It turns out that two different detectors can pick up those correlations in the fields. Typically this is stated in terms of Alice and Bob, which control two different uncorrelated detectors. Once Alice and Bob let their detectors interact with the quantum field, these become correlated, even before enough time passes for them to communicate with each other [104]. That means that Alice and Bob have really *harvested* the correlation present in the field. And this ability to correlate two distant detectors - i.e. two non-relativistic quantum systems - is one of the holy grails of quantum computing and safe communication.

1.2 In this thesis:

Now that we understand better the context for detector models in quantum field theory, we are prepared to explain the content of this thesis. This thesis consists of two main projects in which we use detector models to study different properties of the field. In the first project, we study the sabotage of correlation harvesting protocols. In the second project, we use machine learning to learn from outcomes of probes coupled to a quantum field. We now outline the motivation and content of each of the chapters.

In Chapter 2, we provide some mathematical tools to deal with quantum fields, which we shall use in both projects. We describe the field that we study, how to discretize a quantum field, how to impose a UV-cutoff in a field without inducing superluminal signalling and how to use the Gaussian formalism to study the probe-field system.

The first project, done in collaboration with Abhisek Sahu[9] and Eduardo Martín-Martínez[10], is detailed in Chapter 3. In this project, we analyze a typical harvesting correlation protocol between Alice and Bob in the presence of extra detectors, also called *interlopers*. We calculate the final state of an arbitrary number of detectors analytically after they have interacted instantaneously with a quantum field. We explain what happens to the field and how various correlation measures are affected by different parameters and their physical significance. Most importantly, we study how one single *interloper*, placed in a conveniently evil way, can prevent Alice's and Bob's detectors from harvesting correlations.

The second project, in collaboration with Daniel Grimmer[11] and Eduardo Martín-Martínez, is detailed in Chapter 4. In this chapter, we show how we can use machine learning to learn features from local probes coupled to a quantum field. Usually, one needs to purposefully choose detectors characteristics, coupling parameters and measurement protocols adapted to the target feature of the field that one wishes to study. For example, in Chapter 3, we had to use quite problem-dependent choices for detectors and operations in the field to be able to obtain analytical results. What would happen if a probe-field system was not so tunable? Or if there existed restrictions on the design of the measurement protocol? What if every single parameter was out of our hands and we only had outcomes of local probes connected to the quantum field? Is there anything we could do with that information? The answer is yes: we believe that, by using machine learning techniques to process this information, we could make claims about different features of the field. As proof-of-principle, we consider a harmonic oscillator probe coupled to a scalar

[9]Department of Physics, Indian Institute of Technology-Bombay, Powai, Mumbai 400076, India
[10]Dept. Applied Math, University of Waterloo, Waterloo, ON, N2L 3G1, Canada
[11]Dept. Physics and Astronomy, University of Waterloo, Waterloo, ON, N2L 3G1, Canada

quantum field. We propose a simple measurement protocol for the probe and a common type of neural network to analyze the outcomes of the probe. Both of these choices are not adapted to study any particular feature of the field. To show the broad applicability of these techniques, we show how we can distinguish 1) field's boundary conditions before "light" from the boundaries reaches the probe and 2) temperatures of the state before thermalization time. In both these cases, we discretize the field and impose a UV-cutoff. For completeness, we include an example without such approximations. We show how using slightly different measurement protocol but the same type of neural network we can distinguish a Fock state and a phase-averaged coherent state.

Chapter 2

Toolkit for Quantum Field Theory

In this Chapter, Section 2.7 is verbatim from an unpublished version of [51].

2.1 Klein-Gordon Equation Solution

In this thesis, we are only going to consider real scalar fields whose free dynamics is determined by the Klein-Gordon equation. We will consider a $n+1$ dimensional massive field, ϕ, with mass m. The Klein-Gordon (KG) equation is defined as

$$\frac{1}{c^2}\frac{\partial^2}{\partial t^2}\phi - \nabla^2\phi + \frac{mc^2}{\hbar^2}\phi = 0 \tag{2.1}$$

and is one of the first Lorentz-invariant (i.e. relativistic) equations in Quantum Mechanics. This KG equation can be obtained from the following Lagrangian density:

$$\mathcal{L}_\psi = \frac{1}{2}\left(\frac{1}{c^2}\dot{\phi}^2 - \nabla\phi\cdot\nabla\phi - \frac{m^2c^2}{\hbar^2}\phi^2\right). \tag{2.2}$$

From this Lagrangian we can obtain the conjugate momentum as $\pi = \frac{\partial\mathcal{L}_\phi}{\partial\dot{\phi}} = \dot{\phi}$. We can *second-quantize* the field by promoting both the field, ϕ, and momentum, π, to operators, i.e. adding the hats $\phi \longrightarrow \hat{\phi}$ and $\pi \longrightarrow \hat{\pi}$ and imposing the commutation relations

$$[\hat{\phi}(t,\boldsymbol{x}),\hat{\phi}(t,\boldsymbol{y})] = 0 = [\hat{\pi}(t,\boldsymbol{x}),\hat{\pi}(t,\boldsymbol{y})], \tag{2.3}$$

$$[\hat{\phi}(t,\boldsymbol{x}),\hat{\pi}(t,\boldsymbol{y})] = \mathrm{i}\delta^n(\boldsymbol{x}-\boldsymbol{y}). \tag{2.4}$$

Using these operators we can then obtain Hamiltonian formulation of the Klein Gordon equation:

$$\hat{H}_\phi = \frac{1}{2}\int \mathrm{d}\boldsymbol{x}\; c^2\hat{\pi}(t,\boldsymbol{x})^2 + \nabla\hat{\phi}(t,\boldsymbol{x})\cdot\nabla\hat{\phi}(t,\boldsymbol{x}) + \frac{m^2c^2}{\hbar^2}\hat{\phi}(t,\boldsymbol{x})^2. \tag{2.5}$$

This field operator $\hat{\phi}$, can be written in terms terms of plane wave solutions to the Klein-Gordon equation, $\hat{\phi}_\pm = e^{\pm \mathrm{i}(\omega_{\boldsymbol{k}} t - \boldsymbol{k}\cdot\boldsymbol{x})}$ as

$$\hat{\phi}(\boldsymbol{x},t) = \int \mathrm{d}^n\boldsymbol{k}\frac{1}{\sqrt{2(2\pi)^n\omega_{\boldsymbol{k}}}}\left[\hat{a}^\dagger_{\boldsymbol{k}} e^{\mathrm{i}(\omega_{\boldsymbol{k}} t - \boldsymbol{k}\cdot\boldsymbol{x})} + \hat{a}_{\boldsymbol{k}} e^{-i(\omega_{\boldsymbol{k}} t - \boldsymbol{k}\cdot\boldsymbol{x})}\right], \tag{2.6}$$

where the frequency is given by $\omega_{\boldsymbol{k}} = \sqrt{c^2\boldsymbol{k}^2 + \frac{mc^4}{\hbar^2}}$. By imposing the commutation relations in in Eq. (2.3) and (2.4) we obtain that the operators $\hat{a}^\dagger_{\boldsymbol{k}}$ $\hat{a}_{\boldsymbol{k}}$, are in fact creation and anhilation operators and they obey the canonical commutation relations

$$[\hat{a}_{\boldsymbol{k}}, \hat{a}_{\boldsymbol{k}'}] = [\hat{a}^\dagger_{\boldsymbol{k}}, \hat{a}^\dagger_{\boldsymbol{k}'}] = 0, \qquad [\hat{a}_{\boldsymbol{k}}, \hat{a}^\dagger_{\boldsymbol{k}'}] = \delta^n(\boldsymbol{k} - \boldsymbol{k}'). \tag{2.7}$$

Each pair of operators $\hat{a}^\dagger_{\boldsymbol{k}}$ $\hat{a}_{\boldsymbol{k}}$ defines a mode of the field with frequency $\omega_{\boldsymbol{k}}$.

2.2 Coherent, squeezed, thermal and Fock states

The vacuum or ground state of a field, denoted as $|0\rangle$, is an eigenvector of the Hamiltonian operator (for example, $\hat{\mathcal{H}}_\phi$ in (2.5)). Its defining property is that this state has the lowest energy (its corresponding eigenvalue is the smallest). This state obeys the property $\hat{a}_{\boldsymbol{k}}|0\rangle = 0$ for all $\boldsymbol{k}$. One interesting thing about ground states is that they can undergo quantum fluctuations of energy, which is a purely quantum phenomenon. In the ground of classical fields, one would not expect energy fluctuations. This quantum phenomenon is often interpreted as a manifestation of the Heisenberg uncertainty principle. Interestingly, these quantum fluctuations only appear locally: there is no global energy fluctuation. In other words, in seemingly "empty" states of a field you have particles shortly appearing and disappearing in certain spacetime positions in some correlated fashion. These correlations present in the fluctuations can be exploited by a correlation harvesting protocol, where detectors detect these particles and thus become correlated [137, 109].

The vacuum state $|0\rangle$ is a particular example of what is called a coherent state. A

general coherent state $|\alpha(\boldsymbol{k})\rangle$ is defined as

$$|\alpha(\boldsymbol{k})\rangle = e^{\left(\int d^n\boldsymbol{k}\left[\alpha(\boldsymbol{k})\hat{a}^\dagger_{\boldsymbol{k}} - \alpha(\boldsymbol{k})^*\hat{a}_{\boldsymbol{k}}\right]\right)}|0\rangle \tag{2.8}$$

The unitary operator that acts on the vacuum state to produce a coherent state is called a displacement operator,

$$D_{\alpha(\boldsymbol{k})} = \exp\left[\int d^n\boldsymbol{k}(\alpha(\boldsymbol{k})\hat{a}^\dagger_{\boldsymbol{k}} - \alpha(\boldsymbol{k})^*\hat{a}_{\boldsymbol{k}})\right], \tag{2.9}$$

where $\alpha(\boldsymbol{k})$ is called the coherent amplitude distribution, which is the continuous equivalent to the coherent amplitude. The geometric interpretation and the reason why the state is often called a "displaced state" for a single mode will be given in Section 2.8.

The inverse of a displacement operator with amplitude $\alpha(\boldsymbol{k})$ is its Hermitian conjugate, which turns out to be another displacement operator with amplitude $-\alpha(\boldsymbol{k})$. Moreover, we know that the creator and annihilator operators satisfy the commutation relation in Eq. (2.7), $[\hat{a}_{\boldsymbol{k}}, \hat{a}^\dagger_{\boldsymbol{k'}}] = \delta^{(n)}(\boldsymbol{k} - \boldsymbol{k'})$. We can rewrite the displacement operator using the above commutation relation, which will help us to calculate several properties needed in Chapter 3:

$$D_{\alpha(\boldsymbol{k})} = \exp\left[\int d^n\boldsymbol{k}\alpha(\boldsymbol{k})\hat{a}^\dagger_{\boldsymbol{k}}\right]\exp\left[-\int d^n\boldsymbol{k}\alpha(\boldsymbol{k})^*\hat{a}_{\boldsymbol{k}}\right]\exp\left[-\frac{1}{2}\int d^n\boldsymbol{k}|\alpha(\boldsymbol{k})|^2\right] \tag{2.10}$$

One interesting calculation is the projection of the coherent state $|\alpha_{\boldsymbol{k}}\rangle$ on to the vacuum state. As the annihilator operator $\hat{a}_{\boldsymbol{k}}$ annihilates the vacuum state, $\hat{a}_{\boldsymbol{k}}|0\rangle = 0$, and similarly for the creation operator we have $\langle 0|\,\hat{a}^\dagger_{\boldsymbol{k}} = 0$, we obtain

$$\langle 0|\alpha_{\boldsymbol{k}}\rangle = \langle 0|D_{\alpha\boldsymbol{k}}|0\rangle = \exp\left[-\frac{1}{2}\int d^n\boldsymbol{k}|\alpha(\boldsymbol{k})|^2\right]. \tag{2.11}$$

Another interesting calculation is the projection of the coherent state $|\alpha_{\boldsymbol{k}}\rangle$ on to another coherent state $|\beta_{\boldsymbol{k}}\rangle$. Using again the commutation relation in Eq. (2.7) and the Baker-Campbell-Hausdorff lemma, we can show

$$D_{\alpha(\boldsymbol{k})}D_{\beta(\boldsymbol{k})} = D_{\alpha(\boldsymbol{k})+\beta(\boldsymbol{k})}\exp\left[\frac{1}{2}\int d^n\boldsymbol{k}\big(\alpha(\boldsymbol{k})\beta^*(\boldsymbol{k}) - \alpha^*(\boldsymbol{k})\beta(\boldsymbol{k})\big)\right] \tag{2.12}$$

In the above expression, we take a product of two displacement operators, and get another displacement operator multiplied by a phase factor. We can further generalise this and

take a product of arbitrary number of displacement operators. We now use (2.12) to obtain the inner product of any two arbitrary coherent states, $|\alpha(\boldsymbol{k})\rangle$ and $|\beta(\boldsymbol{k})\rangle$.

$$\langle\alpha(\boldsymbol{k})|\beta(\boldsymbol{k})\rangle = \langle 0|D_{-\alpha(\boldsymbol{k})}D_{\beta(\boldsymbol{k})}|0\rangle \tag{2.13}$$

Using (2.12) and then (2.11), we get the inner product of two coherent states.

$$\langle\alpha(\boldsymbol{k})|\beta(\boldsymbol{k})\rangle = \exp\left[\frac{-1}{2}\int d^n\boldsymbol{k}\big(|\alpha(\boldsymbol{k})|^2 + |\beta(\boldsymbol{k})|^2 - 2\alpha^*(\boldsymbol{k})\beta(\boldsymbol{k})\big)\right] \tag{2.14}$$

The vacuum state $|0\rangle$ is also a particular example of what is called a squeezed state. A general squeezed state $|\zeta(\boldsymbol{k})\rangle$ is defined as

$$|\zeta(\boldsymbol{k})\rangle = e^{\frac{1}{2}\left(\int d^n\boldsymbol{k}\left[-\zeta(\boldsymbol{k})\hat{a}^{\dagger\,2}_{\boldsymbol{k}}+\zeta(\boldsymbol{k})^*\hat{a}^2_{\boldsymbol{k}}\right]\right)}|0\rangle \tag{2.15}$$

The unitary operator that acts on the vacuum state to produce a squeezed state, is called a squeezing operator, with a squeezing amplitude $\zeta(\boldsymbol{k})$.

$$S_{\zeta(\boldsymbol{k})} = \exp\left[\frac{1}{2}\int d^n\boldsymbol{k}(\zeta(\boldsymbol{k})^*\hat{a}^2_{\boldsymbol{k}} - \zeta(\boldsymbol{k})\hat{a}^{\dagger\,2}_{\boldsymbol{k}})\right] \tag{2.16}$$

The geometric interpretation and the reason why this state is called a "squeezed" state will be discussed in Section 2.8 in the case of a single mode.

A Fock state is usually denoted as $|n_{\boldsymbol{k}_1}, n_{\boldsymbol{k}_2}, \ldots, n_{\boldsymbol{k}_i}, \ldots\rangle$, where $n_{\boldsymbol{k}_i}$ denotes the number of particles in with wavenumber $\boldsymbol{k}_i$. The Fock state is defined as

$$|n_{\boldsymbol{k}_1}, n_{\boldsymbol{k}_2}, \ldots, n_{\boldsymbol{k}_i}, \ldots\rangle = \frac{(\hat{a}^\dagger_{\boldsymbol{k}_1})^{n_{\boldsymbol{k}_1}}}{\sqrt{n_{\boldsymbol{k}_1}!}}\frac{(\hat{a}^\dagger_{\boldsymbol{k}_2})^{n_{\boldsymbol{k}_2}}}{\sqrt{n_{\boldsymbol{k}_2}!}}\ldots\frac{(\hat{a}^\dagger_{\boldsymbol{k}_i})^{n_{\boldsymbol{k}_i}}}{\sqrt{n_{\boldsymbol{k}_i}!}}\ldots|0\rangle \tag{2.17}$$

2.3 Unruh-DeWitt model

The Unruh-DeWitt particle detector was first introduced to study curved spacetimes and black holes [136, 134]. One of the first successes of this formalism was the operational formulation of the Unruh effect without relying on ill-defined notions of particles [136, 133].

Mathematically, the interaction Hamiltonian of a stationary Unruh-DeWitt detector

coupled to a field with field operator $\hat{\phi}(t, \boldsymbol{x})$ is

$$\hat{\mathcal{H}}_{\text{INT}} = \lambda \chi(t) \int \mathrm{d}\boldsymbol{x}\, F(\boldsymbol{x})\, \hat{\mu}_{\text{D}} \otimes \hat{\phi}(t, \boldsymbol{x}), \tag{2.18}$$

where λ accounts for the strength of the coupling. Function $\chi(t)$ controls the time dependence of the interaction. It is normally called the *switching function* because the support of the function accounts for the period of time on which detector is "on" or "off". The function $F(x)$, the *smearing function*, accounts for the spatial extent of the interaction. One can think of it as the extent of the detector, just like the extent of an atom interacting with a photon field in light-matter interaction. It also quantifies the coupling of the detector to each of the modes of the field, as we will see in Section 2.6. We would like to note that the switching and smearing function are not necessarily always uncoupled. A most accurate description would be a function $\Lambda(t, \boldsymbol{x})$ that accounts for the spacetime extent of the interaction [84, 88]. However, we chose to introduce the switching and smearing as separate concepts because that is how we treat them in Chapter 3 and Chapter 4.

This linear model is inspired by light-matter interaction and it captures all its fundamental features [105, 85, 83, 7]. The detector typically is a two-level quantum system (qubit) with a monopole moment

$$\hat{\mu}_{\text{D}} = |e\rangle \langle g|\, e^{\mathrm{i}\Omega t} + |g\rangle \langle e|\, e^{-\mathrm{i}\Omega t}, \tag{2.19}$$

where $|g\rangle, |e\rangle$ are the ground and excited states and Ω the energy gap between them. In Chapter 3 we will choose this particular degree of freedom for the probe. In Chapter 4, we will choose the detector to be a harmonic oscillator, coupled to the field with their position operator:

$$\hat{\mu}_{\text{D}} = \hat{q}_{\text{D}} \tag{2.20}$$

Depending on the system under study the nature of the probe will be different. Our choices for the two chapters were practical. For Chapter 3, having a qubit probe simplified our analytical results. In Chapter 4, a harmonic oscillator allowed us to do numerical calculations after introducing a UV-cutoff. In the next section, we will explain what is a UV-cutoff and how to rightfully impose it taking into account our model detector.

2.4 Field discretization

From the well-established area of numerical analysis, we know that we can obtain approximate solutions of a partial differential equation by solving a discretized version of

the original equation. This discretization reduces the complexity of the problem: solving the discrete equation becomes equivalent to solving a linear equation. However, different choices in the discretization can affect the accuracy of the approximation. For example, the Euler and Runge-Kutta methods different use approximations of the derivative, which in turn leads to different local and global errors on the numerical solution. The choice of lattice pattern can also affect the quality of the approximation. For example, choosing a finer lattice for sections where the exact solution oscillates faster will generally result in a better approximation.

In quantum field theory, we also want to obtain the solution to a differential equation for which the solution is the quantum field, $\hat{\phi}$. To do so we discretize space in the free Klein-Gordon Hamiltonian and in the interaction Hamiltonian of a field and a probe, given respectively in Eq. (2.5) and Eq. (4.3):

$$\hat{H}_\phi = \frac{1}{2}\int \mathrm{d}\boldsymbol{x}\; c^2\hat{\pi}(t,\boldsymbol{x})^2 + \nabla\hat{\phi}(t,\boldsymbol{x})\cdot\nabla\hat{\phi}(t,\boldsymbol{x}) + \frac{m^2c^2}{\hbar^2}\hat{\phi}(t,\boldsymbol{x})^2, \tag{2.21}$$

$$\hat{\mathcal{H}}_{\text{INT}} = \lambda\,\chi(t)\int \mathrm{d}\boldsymbol{x}\, F(\boldsymbol{x})\,\hat{\mu}_{\text{D}}\otimes\hat{\phi}(t,\boldsymbol{x}). \tag{2.22}$$

Just like in any numerical problem, we have the liberty to choose a lattice pattern. In this thesis we choose a square pattern in which close neighbours are at a distance a. This results as

$$\hat{\mathcal{H}}_\phi \approx \frac{a}{2}\sum_n c^2\hat{\pi}^2(t,\boldsymbol{x}_n) + \nabla\hat{\phi}(t,\boldsymbol{x}_n)\cdot\nabla\hat{\phi}(t,\boldsymbol{x}_n) + \frac{m^2c^2}{\hbar^2}\hat{\phi}^2(t,\boldsymbol{x}_n), \tag{2.23}$$

$$\hat{\mathcal{H}}_{\text{INT}} \approx \lambda\,\chi(t)\sum_n a\,F(\boldsymbol{x}_n)\,\hat{\mu}_{\text{D}}\otimes\hat{\phi}(t,\boldsymbol{x}_n). \tag{2.24}$$

Changing the spacing a one can observe different behaviour of the entanglement entropy [106]. Our choice of a in the specific examples in this thesis is justified in Section (2.7). We note that, in this case, the operators $\hat{\phi}(t,\boldsymbol{x}_n)$ and $\hat{\pi}(t,\boldsymbol{x}_m)$ satisfy the commutation relations, $[\hat{\phi}(t,\boldsymbol{x}_n),\hat{\pi}(t,\boldsymbol{x}_m)] = \mathrm{i}\hbar(\delta_{nm}/a)\mathbb{1}$.

We can further impose an approximation of the derivative. This choice does not go without consequence: it will affect the number of modes that each mode couples to. For example, a common choice for the derivative [132] when dealing with a 1+1 dimensional field is

$$\partial_x\hat{\phi}(t,x_n) \approx \frac{\hat{\phi}(t,x_{n+1}) - \hat{\phi}(t,x_n)}{a}, \tag{2.25}$$

which yields nearest-neighbours coupling. Some works in preparation[1] find the choice of derivative approximation has an effect on the entanglement structure of the field. However, the comparison of different versions of the derivative approximation is out of the scope of this thesis. In Section 2.7 and Chapter 4 we will choose the approximation in (2.25), which, in the case of 1+1 dimensional field, will yield the discrete Hamiltonian

$$\hat{\mathcal{H}}_\phi = \frac{a}{2}\sum_n c^2\hat{\pi}^2(t,x_n) + \left(\frac{\hat{\phi}(t,x_{n+1}) - \hat{\phi}(t,x_n)}{a}\right)^2 + \frac{m^2c^2}{\hbar^2}\hat{\phi}^2(t,x_n). \tag{2.26}$$

We note that, in this case, the operators $\hat{\phi}(t,x_n)$ and $\hat{\pi}(t,x_m)$ satisfy the commutation relations, $[\hat{\phi}(t,x_n),\hat{\pi}(t,x_m)] = \mathrm{i}\hbar(\delta_{nm}/a)\mathbb{1}$.

Finally, in Chapter 4 we consider a field inside a cavity of length L, i.e. the field is restricted to a region $x \in [0,L]$. Defining $L = N\,a$, we only need to consider a finite number of modes to obtain an approximation of the field. We can rewrite the Hamiltonian (2.27) in terms of the dimensionless operators, $\hat{q}_n = \sqrt{am/\hbar^2}\,\hat{\phi}(\mathsf{x}_n)$ and $\hat{p}_n = \sqrt{a/m}\,\hat{\pi}(\mathsf{x}_n)$ which satisfy the commutation relations, $[\hat{q}_i,\hat{p}_j] = \mathrm{i}\delta_{ij}\mathbb{1}$. This yields one of the bandlimited field Hamiltonian claimed in the Chapter 4

$$\hat{\mathcal{H}}_\phi^{\mathrm{UV}} = \sum_{n=1}^{N}\frac{mc^2}{2}\left(\hat{p}_n^2 + \hat{q}_n^2\right) + \frac{\hbar^2}{2ma^2}(\hat{q}_{n+1} - \hat{q}_n)^2. \tag{2.27}$$

In the next section, we explain how imposing a UV cutoff (bandlimiting the field) we can induce a field discretization. If a function is bandlimited, it can be reconstructed using only values of the function at discrete points [102]. Once a choice of lattice is made, the derivative will be fixed [94], so any approximation such as the one in Eq. (2.25) will be an extra assumption. We will comment on this extra assumption in Section 2.5 and Section 2.7.

2.5 Imposing UV cutoff to discretize the field

In Section 2.4 we showed a discretization of the field. In this section, we will show how a UV-cutoff on the field can induce a discretization of the field. Applying a UV-cutoff consists of removing the modes of the field of frequencies larger than some cutoff scale K. If we expand the field operator, $\hat{\phi}(t,\boldsymbol{x})$ in terms of its Fourier transform, taking a UV

[1] Personal conversation with Eduardo Martín-Martínez and Daniel Grimmer

cutoff is equivalent to obtaining

$$\hat{\phi}^{\text{UV}}(t,\boldsymbol{x}) = \int_{|\boldsymbol{k}|<K} \mathrm{d}\boldsymbol{k}\, \hat{\Phi}(t,\boldsymbol{k}) e^{\mathrm{i}\boldsymbol{k}\cdot\boldsymbol{x}}, \tag{2.28}$$

where $\hat{\Phi}(t,\boldsymbol{k}) = \mathcal{F}_{\boldsymbol{k}}[\hat{\phi}(t,\boldsymbol{x})]$ is the Fourier transform of $\hat{\phi}(t,\boldsymbol{x})$. Imposing a hard UV cutoff on the interaction is equivalent to multiplying the Fourier transform of the field by $\Pi_K(k)$, defined as the n-dimensional rectangle function over over $\boldsymbol{k} \in [-K,K]^n$. The truncated field then becomes

$$\hat{\phi}^{\text{UV}}(t,\boldsymbol{x}) \coloneqq \mathcal{F}_{\boldsymbol{x}}^{-1}\left[\Pi_K(k)\mathcal{F}_k[\phi(t,\boldsymbol{x})]\right] \tag{2.29}$$

One can then use the Petersen–Middleton theorem[2] [102] to reconstruct $\hat{\phi}^{\text{UV}}$ with discrete points in a lattice. However, for this thesis it is enough to consider the one dimensional case. With this restriction, we use the variables x and k instead of $\boldsymbol{x}$ and $\boldsymbol{k}$. Using the Nyquist-Shannon sampling theorem to reconstruct our UV cutoff smearing function we obtain

$$\hat{\phi}^{\text{UV}}(t,x) = \sum_j \hat{\phi}^{\text{UV}}(t,x_j)\, S_j(x/a)\,. \tag{2.30}$$

where $a = \pi/K$ is the spacing of the discrete positions, $x_j = j\,a$, and where

$$S_j(r) \coloneqq \frac{\sin(\pi(r-j))}{\pi(r-j)} \tag{2.31}$$

is a displaced normalized sinc function.

Since it will be useful for Chapter 4, let us a apply a hard UV-cutoff to the free Klein-Gordon Hamiltonian in (2.5) in the one dimensional case, which depends on $\hat{\phi}(t,x)$, $\hat{\pi}(t,x)$ and $\partial_x\hat{\phi}(t,x)$. By removing the field modes with $\boldsymbol{k} > |K|$ we obtain the the UV-cutoff field operators

$$\hat{\pi}^{\text{UV}}(\mathsf{x}) \coloneqq \mathcal{F}_x^{-1}\left[\Pi_K(k)\mathcal{F}_k[\pi(\mathsf{x})]\right], \tag{2.32}$$

$$\partial_x\hat{\phi}^{\text{UV}}(\mathsf{x}) \coloneqq \mathcal{F}_x^{-1}\left[\Pi_K(k)\mathcal{F}_k[\partial_x\phi(\mathsf{x})]\right], \tag{2.33}$$

where where $\mathsf{x} \coloneqq (t,x)$. Note that since these operators are now bandlimited we can

[2]The n-dimensional generalization of Nyquist-Shanon theorem

express them as sums of sinc functions as,

$$\hat{\pi}^{\mathrm{UV}}(\mathsf{x}) = \sum_n \hat{\pi}^{\mathrm{UV}}(\mathsf{x}_n)\, S_n(x/a)\,, \tag{2.34}$$

$$\partial_x\hat{\phi}^{\mathrm{UV}}(\mathsf{x}) = \sum_n \partial_x\hat{\phi}^{\mathrm{UV}}(\mathsf{x}_n)\, S_n(x/a)\,. \tag{2.35}$$

Using these UV-cutoff operators we define the UV-cutoff field Hamiltonian as,

$$\hat{\mathcal{H}}^{\mathrm{UV}}_{\phi} \coloneqq \frac{1}{2}\int_{-\infty}^{\infty} \mathrm{d}x\; c^2\hat{\pi}^{\mathrm{UV}}(\mathsf{x})^2 + (\partial_x\hat{\phi}^{\mathrm{UV}}(\mathsf{x}))^2 + \frac{m^2c^2}{\hbar^2}\hat{\phi}^{\mathrm{UV}}(\mathsf{x})^2 = \tag{2.36}$$

$$\frac{a}{2}\sum_n c^2\hat{\pi}(\mathsf{x}_n)^2 + (\partial_x\hat{\phi}(\mathsf{x}_n))^2 + \frac{m^2c^2}{\hbar^2}\hat{\phi}(\mathsf{x}_n)^2, \tag{2.37}$$

where we have again used the operator's sinc representations and L^2 orthonormality of $\{S_m(r)\}$ to express the integral as a sum. The derivative in this case will be then

$$\begin{aligned}\partial_x\hat{\phi}(x_k) &= \frac{1}{a}\sum_n \left(\int_{-\infty}^{\infty}\mathrm{d}x\partial_x S_n(x/a)S_k(x/a)\right)\hat{\phi}(x_n) = \frac{1}{a}\sum_{n\neq k}\frac{(-1)^{k-n}}{k-n}\hat{\phi}(x_n)\\ &= 2\sum_{m=1}^{\infty}(-1)^{m-1}\frac{\hat{\phi}(x_{k+m})-\hat{\phi}(x_{k-m})}{2ma},\end{aligned} \tag{2.38}$$

which involves highly non-local couplings that decrease polynomically. In this thesis, we impose the extra approximation in Eq. 2.25:

$$\partial_x\hat{\phi}(t,x_n) \approx \frac{\hat{\phi}(t,x_{n+1})-\hat{\phi}(t,x_n)}{a}, \tag{2.39}$$

which will simplify our calculations. A detailed explanation on the physical implications of this choice are given in Section 2.7.

Using the UV-cutoff field $\hat{\phi}^{\mathrm{UV}}$ in (2.30) into the interaction Hamiltonian in (4.3) we would obtain the UV-cutoff version of the Hamiltonian

$$\hat{\mathcal{H}}^{\mathrm{UV}}_{\mathrm{INT}} = \lambda\,\chi(t)\sum_j a\,F(x_j)\,\hat{\mu}_{\mathrm{D}}\otimes\hat{\phi}^{\mathrm{UV}}(t,x_j). \tag{2.40}$$

here we have also used the orthonormality of the collection $\{S_m(r)\}$ in the L^2 norm. Thus, by taking a hard UV cutoff on the probe's smearing function we automatically find that

the probe effectively couples to the field at discrete positions x_j. For this last Hamiltonian, we can use our knowledge about the probe extension (or smearing) to motivate a cutoff scale, as we will discuss in the next section.

2.6 Local probes induce a soft UV cutoff

Applying a UV-cutoff is not harmless. This procedure can lead to superluminal signalling [87], but done carefully, it is *almost* harmless. Since we are using detectors to probe the field, if the detectors are not able to resolve the scales of the cutoff then the noxious effects of the UV truncation are reduced. To see when a UV-cutoff is *mostly harmless* for detector physics let us first expand the Unruh-DeWitt interaction Hamiltonian in (4.3) using the Fourier transform of the field, $\hat{\Phi}(t,\boldsymbol{k}) = \mathcal{F}_{\boldsymbol{k}}[\hat{\phi}(t,\boldsymbol{x})]$,

$$\hat{\mathcal{H}}_{\text{INT}} = \lambda\,\chi(t)\,\hat{\mu}_{\text{D}} \otimes \int \mathrm{d}\boldsymbol{x} F(\boldsymbol{x}) \left(\int \mathrm{d}\boldsymbol{k}\,\hat{\Phi}(t,\boldsymbol{k}) e^{\mathrm{i}\boldsymbol{k}\cdot\boldsymbol{x}} \right) = \lambda\,\chi(t)\,\hat{\mu}_{\text{D}} \otimes \int \mathrm{d}\boldsymbol{k}\,\tilde{F}(-\boldsymbol{k})\,\hat{\Phi}(t,\boldsymbol{k}) \tag{2.41}$$

where $\tilde{F}(\boldsymbol{k}) = \mathcal{F}_{\boldsymbol{k}}[F(\boldsymbol{x})]$ is the Fourier transform of $F(\boldsymbol{x})$. For even smearing functions, $\tilde{F}(\boldsymbol{k}) = \tilde{F}(-\boldsymbol{k})$. Therefore $\tilde{F}(\boldsymbol{k})$ determines how strongly the probe couples to each of the field modes, or in other words, "the frequency extent of the probe-field interaction". If the smearing function is strongly supported only on a finite region of size $\sim \sigma$ then $\tilde{F}(\boldsymbol{k})$ would be supported on an extent $\sim 1/\sigma$. That is, the probe would not couple strongly to modes with wavevector $|\boldsymbol{k}| \gg \sigma^{-1}$. Thus by considering a probe with a finite spatial extent we are effectively considering a soft-UV cutoff in the interaction of field and probe.

If $\tilde{F}(\boldsymbol{k})$ decays sufficiently fast away from σ^{-1}, we may be justified in dropping the coupling to the modes above some large UV threshold, say $|\boldsymbol{k}| > K > \sigma^{-1}$. This provides us with a scale to apply a hard UV-cutoff on the field, which in turn provides a scale for the distance between elements of the lattice, as $a = \pi/K < \pi\sigma$.

2.7 Error quantification of field discretization

In Section 2.4 we derived the discretized version of the Klein-Gordon Hamiltonian, Eq. (2.27). However, as discussed, this approximation can introduce superluminal signalling [87]. Therefore, we need a way to quantify how much we are deviating from a relativistic response and how accurate is the discretization. In order to do so let us review our choices

1. We took a UV-cutoff in the field Hamiltonian, i.e. we removed the high-frequency modes of the field, and

2. We further imposed the nearest-neighbour approximation for the derivative.

As we explained in Section 2.6, the extent of the probe induces suppresses the coupling of the probe to the high energy modes of the field. Therefore, removing these modes will be irrelevant to the probe's response with increasing cutoff K. The effect of the second change is more subtle. The discrete approximation for the derivative changes the dispersion relation of the field as

$$\hbar\omega_k = \sqrt{(m\,c^2)^2 + (\hbar\,c\,k)^2} \quad \longrightarrow \quad \hbar\omega'_k = \sqrt{(m\,c^2)^2 + \left(\frac{2\,\hbar\,c\,K}{\pi}\right)^2 \sin^2\left(\frac{\pi\,k}{2\,K}\right)}. \tag{2.42}$$

In Figure 2.1a) we plot both dispersion relations and note that $\hbar\omega_k \geq \hbar\omega'_k$. The dispersion relation is mostly modified at high frequencies, that is, at frequencies to which the probe does not couple strongly. This modified dispersion relation allows for the possibility of superluminal signals to existing in these high-frequency modes.

To quantify how much the dispersion relation has changed *in the modes the probe couples strongly to*, we introduce the "average relative error" in $\hbar\omega_k$. This error is the average relative difference between the modified and unmodified dispersion relations at each frequency weighted by the strength of the probe's coupling to that frequency. That is,

$$\text{Avg. Rel. Error} \coloneqq \int_{-\infty}^{\infty} \mathrm{d}k\ \frac{\hbar\omega_k - \hbar\omega'_k}{\hbar\omega_k}\ \tilde{F}(k). \tag{2.43}$$

We have computed the average relative error for various cutoff, field masses, and probe sizes in Fig 2.1b).

To investigate how the average relative error decreases as we increase K we use the following series of inequalities,

$$\text{Avg. Rel. Error} \leq \int_{-\infty}^{\infty}\mathrm{d}k\ \frac{(\hbar\omega_k)^2 - (\hbar\omega'_k)^2}{(\hbar\omega_k)^2}\ \tilde{F}(k) \leq \int_{-\infty}^{\infty}\mathrm{d}k\ \frac{(\hbar\omega_k)^2 - (\hbar\omega'_k)^2}{(\hbar\,c\,k)^2}\ \tilde{F}(k). \tag{2.44}$$

where the first inequality follows from $\hbar\omega_k \geq \hbar\omega'_k \geq 0$ and the second from $\hbar\omega_k \geq \hbar ck$.

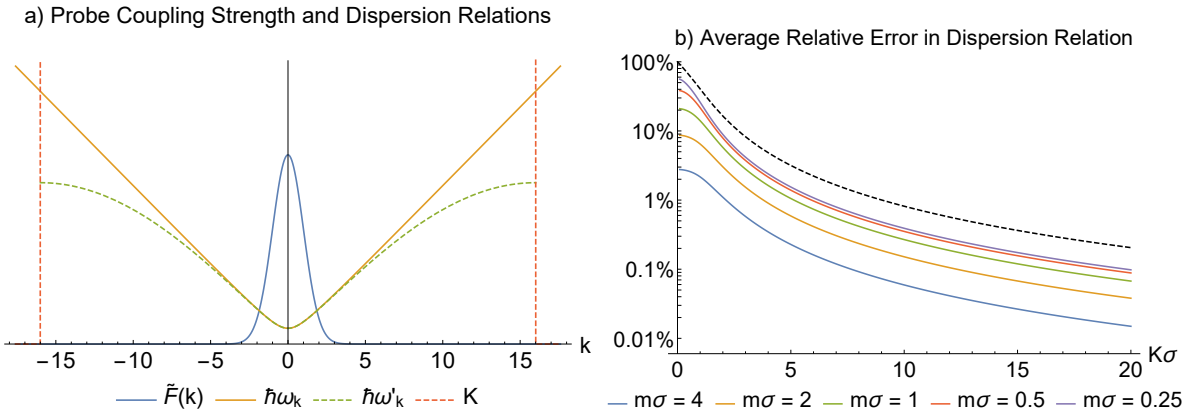

Figure 2.1: Modified dispersion relation and average relative error in dispersion relation. In subfigure a) we show the probe's coupling strength to the field modes, $\tilde{F}(k)$, (blue Gaussian) as a function of the mode's wavenumber, k. Note that the probes width is taken to be $\sigma = 1$. The field's dispersion relation $\hbar\omega_k$ is also plotted (yellow hyperbola). Note that the field's mass is taken to be $m = 1$. Taking a UV-cutoff at $K = 16$ (vertical red dashed line) yields a modified dispersion relation, $\hbar\omega'_k$, (green dashed) at high frequencies. In subfigure b) we plot the average relative error in $\hbar\omega_k$ as a function the cutoff K and the field mass m. This error decreases polynomially as $K\sigma$ increases. The error also decreases as the mass of the field increases. The black dashed line is a mass independent upper-bound on this error. In both subfigures we have taken $\hbar = c = 1$.

The final expression is mass-independent and can be computed in closed form yielding,

$$\text{Avg. Rel. Error} \leq 1+2\frac{K\sigma}{\sqrt{2\pi}}\text{Erf}\left(\frac{\pi}{K\sigma\sqrt{2}}\right)+\frac{2K^2\sigma^2}{\pi^2}\left(1-\exp\left(\frac{-\pi^2}{2\,K^2\sigma^2}\right)\right)\sim O\left(\frac{1}{(K\sigma)^2}\right). \tag{2.45}$$

Therefore we expect the error made by the discrete approximation to be quadratically suppressed as we increase $K\sigma$. For example, for a Gaussian smearing function of width σ and cutoff $K\sigma = 16$, the upper-bound on average relative error is 0.32%. With the right field's mass and Gaussian's width relation, this relative error can reduce enough to be almost harmless, as depicted in in Fig 2.1b). In Chapter 4, we precisely choose a Gaussian smearing function and cutoff cutoff $K\sigma = 16$. In the remote boundary sensing and thermometry examples we have (taking $\hbar = c = 1$), $m\sigma = 0.006$ and $m\sigma = 0.00027$ respectively. The average relative error can be computed numerically in each case yielding 0.16% in both cases.

2.8 Gaussian formalism

The Gaussian formalism of quantum mechanics is a potent tool to deal with continuous variable systems. It is used to study systems composed by a finite number of bosonic modes, which can be characterized by dimensionless position and momentum operators $\hat{q}_k$ and $\hat{p}_k$. An example of such a system is the discretized version of the quantum field given in Section 2.4, which is composed of N bosonic modes. Gaussian formalism can be used for the ground state or the coherent and thermal states of a free quadratic Hamiltonian (i.e. the Hamiltonian is a quadratic form in variables $\hat{q}_k$ and $\hat{p}_k$), which are examples of *Gaussian states*. Furthermore, when evolving under a quadratic Hamiltonian, Gaussian states remain Gaussian and their time evolution can be studied with the Gaussian formalism.

In subsection 2.8.1, we are going to explain what Gaussian states are and how to represent the ground, coherent and thermal states. In subsection 2.8.2 we study the time evolution of Gaussian states.

2.8.1 Gaussian states

We consider a system composed by N bosonic modes, labeled by $k = 1, \ldots, N$, with corresponding dimensionless position and momentum operators $\hat{q}_k$ and $\hat{p}_k$. These operators obey the commutation relation $[\hat{q}_k, \hat{p}_k] = \mathrm{i}\mathbb{1}$. We can define the vector of the canonical

operators and write its commutative relations in a compact form,

$$\hat{\boldsymbol{R}} = (\hat{q}_1, \hat{p}_1, \hat{q}_2, \hat{p}_2, \ldots, \hat{q}_N, \hat{p}_N) = (\hat{R}_1, \ldots, \hat{R}_{2N}), \tag{2.46}$$

where the commutation relations are $[\hat{R}_k, \hat{R}_l] = \mathrm{i}\Omega_{kl}$. The matrix Ω, so called *symplectic matrix* is given by

$$\Omega = \bigoplus_{n=1}^{N} \begin{pmatrix} 0 & 1 \\ -1 & 0 \end{pmatrix}. \tag{2.47}$$

Alternatively, this vector of canonical operators can be written in another popular ordering as

$$\hat{\boldsymbol{R}}' = (\hat{q}_1, \hat{q}_2, \ldots, \hat{q}_N, \hat{p}_1, \hat{p}_2, \ldots, \hat{p}_N) = (\hat{R}'_1, \ldots, \hat{R}'_{2N}). \tag{2.48}$$

In this case commutation relations are $[\hat{R}'_k, \hat{R}'_l] = \mathrm{i}\Omega'_{kl}$. The matrix Ω' is given by

$$\Omega' = \begin{pmatrix} 0 & \mathbb{1} \\ -\mathbb{1} & 0 \end{pmatrix}. \tag{2.49}$$

From this moment on, we will loosely refer to both $\hat{\boldsymbol{R}}$ and $\hat{\boldsymbol{R}}'$ as basis. We will say that a matrix is written in basis $\hat{\boldsymbol{R}}$ if it corresponds to a quadratic form in variables $\hat{\boldsymbol{R}}$. We will use the same notation for the matrices Ω and Ω', which represent the commutation relations in basis $\hat{\boldsymbol{R}}$ and $\hat{\boldsymbol{R}}'$ respectively.

After the presentation of the system of interest, we can start to talk about the Gaussian formalism. The core of this formalism is to map a density matrix, $\hat{\rho}$, describing the N-mode bosonic system, into a function depending on the phase space variables $\boldsymbol{x} = (x_1, x_2, \ldots, x_N)$ and $\boldsymbol{p} = (p_1, p_2, \ldots, p_N)$. One of the most common mappings is the so called Wigner transformation. The counterpart of the density matrix, $\hat{\rho}$, in the Wigner transformation is called the Wigner function, and it is defined as

$$W(\boldsymbol{x}, \boldsymbol{p}) = \frac{1}{\pi^N} \int_{\mathbb{R}^N} \mathrm{d}^N \boldsymbol{s}\ \langle \boldsymbol{x} + \boldsymbol{s} \,|\, \hat{\rho} \,|\, \boldsymbol{x} - \boldsymbol{s} \rangle \exp(-2\mathrm{i}\, \boldsymbol{p} \cdot \boldsymbol{s}). \tag{2.50}$$

The Wigner function is what is called a "quasiprobability distribution". The reason behind that name is that it possesses a set of properties [72] that make it really similar to a probability distributions:

1. $W(\boldsymbol{x}, \boldsymbol{p})$ is normalized: $\int \mathrm{d}^N \boldsymbol{x}\, \mathrm{d}^N \boldsymbol{p}\, W(\boldsymbol{x}, \boldsymbol{p}) = 1$.

2. The marginal distributions correspond to our notion of probability distribution in the position and space basis, where

$$\int \mathrm{d}^N \boldsymbol{x}\, W(\boldsymbol{x},\boldsymbol{p}) = \langle \boldsymbol{p}|\, \hat{\rho}\, |\boldsymbol{p}\rangle\,, \qquad \int \mathrm{d}^N \boldsymbol{p}\, W(\boldsymbol{x},\boldsymbol{p}) = \langle \boldsymbol{x}|\, \hat{\rho}\, |\boldsymbol{x}\rangle\,. \tag{2.51}$$

3. It gives the right expected values for operators. Given an operator $\hat{A}$ with the corresponding Wigner function $\tilde{A}(\boldsymbol{x},\boldsymbol{p})$, its expected value for density matrix $\hat{\rho}$ can be written as

$$\mathrm{Tr}\left(\hat{\rho}\hat{A}\right) = \int \mathrm{d}^N \boldsymbol{x}\, \mathrm{d}^N \boldsymbol{p}\, W(\boldsymbol{x},\boldsymbol{p})\tilde{A}(\boldsymbol{x},\boldsymbol{p}). \tag{2.52}$$

4. The Wigner function of a subsystem A composed by N_{A} modes, $W_{\mathrm{A}}(\boldsymbol{x}_{\mathrm{A}},\boldsymbol{p}_{\mathrm{A}})$, can be obtained by integrating the rest of variables:

$$W_{\mathrm{A}}(\boldsymbol{x}_{\mathrm{A}},\boldsymbol{p}_{\mathrm{A}}) = \int \mathrm{d}^{N_{\mathrm{B}}}\boldsymbol{x}_{\mathrm{B}}\, \mathrm{d}^{N_{\mathrm{B}}}\boldsymbol{p}_{\mathrm{B}}\, W(\boldsymbol{x},\boldsymbol{p}), \tag{2.53}$$

   where $\boldsymbol{x}_{\mathrm{B}}, \boldsymbol{p}_{\mathrm{B}}$ are the variables of the system B, which is formed by the $N_{\mathrm{B}} \coloneqq N - N_{\mathrm{A}}$ remaining modes.

However, the Wigner function does not generally obey one essential property of probabiliy distributions, which is the reason why it is called "quasiprobability" distribution: $W(\boldsymbol{x},\boldsymbol{p})$ is not necessarily positive [72].

A great thing about the Wigner transformation is that it is bijective: there is a one-to-one correspondence between Wigner functions and density matrices. Thus, without losing any information, one can study a system using only Wigner functions. Dealing with these Wigner functions is especially easy for Gaussian states.

A **Gaussian state**, given by density matrix state $\hat{\rho}$, is a state whose corresponding Wigner function is Gaussian, i.e. $W(\boldsymbol{x},\boldsymbol{p})$ can be written as

$$W(\boldsymbol{r}) = \frac{e^{-\frac{1}{2}(\boldsymbol{r}-\bar{\boldsymbol{r}})^T\sigma(\boldsymbol{r}-\bar{\boldsymbol{r}})}}{\pi^N\sqrt{\det(\sigma)}}, \tag{2.54}$$

where $\boldsymbol{r} = (\boldsymbol{x},\boldsymbol{p})$, $\bar{\boldsymbol{r}}$ is a $2N$-dimensional vector and σ is a $2N$-dimensional square matrix.

The fact that these states are Gaussian simplifies calculations. A Gaussian function can be characterized by its first and second-order moments. Therefore, by knowing only

$2N + 4N^2$ parameters [2], we are able to describe perfectly a particular Gaussian state — whereas previously we had to deal with a continuous system that is infinite-dimensional. Furthermore, the Wigner function of a Gaussian state is always positive. Then the Wigner function can be interpreted as a probability function for the $\hat{x}_k$ and $\hat{p}_k$ observables. It is interesting to note that, for pure states, the corresponding Wigner function is positive if and only if the state is Gaussian [63].

Finally there is a direct connection between the first and second moments of the Wigner function and the first and second moments of the operator vector $\hat{\boldsymbol{R}}$. Given a Gaussian state ρ, the first moments and the covariance matrix of the Wigner function are given by

$$\bar{r} = (\langle \hat{R}_1 \rangle, \ldots, \langle \hat{R}_{2N} \rangle), \tag{2.55}$$

$$\sigma_{ij} = \langle \hat{R}_i \hat{R}_j + \hat{R}_j \hat{R}_i \rangle - 2\langle \hat{R}_i \rangle \langle \hat{R}_j \rangle, \tag{2.56}$$

where $\langle A \rangle = \mathrm{Tr}\left[\rho \hat{A}\right]$. Gaussian states are completely defined by the first moments of the operators $\hat{R}_i$ and the second moments of operators $\hat{R}_i$ and $\hat{R}_j$.

In this formalism, obtaining the covariance matrix and the first moments of a subsystem is very straightforward. To obtain the covariance matrix σ_{A} of a subsystem A one only needs to "eliminate" from the original covariance matrix, σ, the rows and columns that do not correspond to subsystem A. Similarly, to obtain the first moments $\bar{\boldsymbol{r}}_{\mathrm{A}}$, one needs to "eliminate" from the original vector of first moments, $\bar{\boldsymbol{r}}$, the rows that do not correspond to subsystem A

This last "tracing out" property of Gaussian states stems from the fact that tensor product structure in Hilbert space translates to direct sum in phase-space. The direct sum of two square matrices A_1 and A_2, of sizes n_1 and n_2 is defined as

$$A_1 \oplus A_2 \coloneqq \begin{pmatrix} A_1 & \mathbb{0}_{n1,n_2} \\ \mathbb{0}_{n2,n_1} & A_2 \end{pmatrix} \tag{2.57}$$

where $\mathbb{0}_{n,m}$ is a zero matrix of size $n \times m$. The underlying product structure is then conserved when state with density matrix $\hat{\rho} = \hat{\rho}_1 \otimes \hat{\rho}_2$ is represented by the covariance matrix $\sigma = \sigma_1 \oplus \sigma_2$ in phase-space.

After this brief introduction to the Gaussian formalism, we will show how to calculate the covariance matrix and mean of some states considered in Chapter 4.

Some useful states for this thesis

We will show the covariance matrices and first moments of ground states and thermal states of Hamiltonians of the form:

$$\hat{H} = \frac{\omega}{2}\hat{\boldsymbol{p}}^T\hat{\boldsymbol{p}} + \frac{\omega}{2}\hat{\boldsymbol{q}}^T M\hat{\boldsymbol{q}}, \tag{2.58}$$

where M is some symmetric, positive definite matrix, the frequency ω obeys $\omega > 0$, $\hat{\boldsymbol{p}} = (\hat{p}_1, \hat{p}_2, \ldots, \hat{p}_N)$ and $\hat{\boldsymbol{q}} = (\hat{q}_1, \hat{q}_2, \ldots, \hat{q}_N)$. Since M is definite positive and symmetric, there exists an orthogonal matrix C ($C^T = C^{-1}$) such that $D = C^T MC$ and D is diagonal. Doing the change of basis $\hat{\boldsymbol{x}} = C\hat{\boldsymbol{x}}'$ and $\hat{\boldsymbol{p}} = C\hat{\boldsymbol{p}}'$, it is easy to check the commutation relations $[\hat{x_i}', \hat{x_j}'] = 0 = [\hat{p_i}', \hat{p_j}']$ and $[\hat{x_i}', \hat{p_j}'] = \mathrm{i}\delta_{ij}$. Doing this change of variables we can write the Hamiltonian as

$$\hat{H} = \frac{\omega}{2}\hat{\boldsymbol{p}}'^T C^T C\hat{\boldsymbol{p}}' + \frac{\omega}{2}\hat{\boldsymbol{x}}'^T C^T MC\hat{\boldsymbol{x}}' = \sum_{i=1}^{N}\frac{\omega}{2}(\hat{p_i}'^2 + D_{ii}\,\hat{x_i}'^2) = \sum_{i=1}^{N}\omega\sqrt{D_{ii}}(\frac{1}{2} + \hat{a}_i^\dagger\hat{a}_i), \tag{2.59}$$

with the annihilation and creation operators defined by the equations

$$\hat{p_i}' = \frac{\sqrt[4]{D_{ii}}}{\mathrm{i}\sqrt{2}}(\hat{a}_i - \hat{a}_i^\dagger), \qquad \hat{x_i}' = \frac{1}{\mathrm{i}\sqrt{2}\sqrt[4]{D_{ii}}}(\hat{a}_i + \hat{a}_i^\dagger), \tag{2.60}$$

and commutation relation $[\hat{a}_i, \hat{a}_i^\dagger] = 1$. Using the creation and anhilation operator, one can easily calculate the first moments and covariance matrices of several states.

For the **ground state** is easy to check that $\langle\hat{x_i}\rangle = 0 = \langle\hat{p_i}\rangle$. In that case the vector of first moments $\bar{\boldsymbol{r}}$ is identically zero. Its covariance matrix in the basis $\hat{\boldsymbol{R}}'$ (as in Eq. (2.48)) is

$$\sigma_{\text{GROUND}} = \begin{pmatrix} \frac{1}{\sqrt{M}} & 0 \\ 0 & \sqrt{M} \end{pmatrix}. \tag{2.61}$$

The Gibbs **thermal state** of a given Hamiltonian $\hat{H}$ with inverse temperature β is defined as

$$\hat{\rho} = \frac{e^{-\beta\hat{H}}}{\mathrm{Tr}\left(e^{-\beta\hat{H}}\right)}. \tag{2.62}$$

It can easily be checked that $\langle\hat{x_i}\rangle = 0 = \langle\hat{p_i}\rangle$ and so the vector of first moments $\bar{\boldsymbol{r}}$ is zero.

Its covariance matrix can be easily in the basis $\hat{\boldsymbol{R}}'$ (basis given in Eq. (2.48)):

$$\sigma_{\text{THERMAL}} = \begin{pmatrix} \frac{1}{\sqrt{M}} \coth\left(\frac{\beta\omega\sqrt{M}}{2}\right) & 0 \\ 0 & \sqrt{M}\coth\left(\frac{\beta\omega\sqrt{M}}{2}\right) \end{pmatrix}. \tag{2.63}$$

As β approaches infinity (the zero temperature limit) we recover the covariance matrix for the ground state.

A **one-mode squeezed state** [72] is defined as

$$|\zeta\rangle = \hat{S}_\zeta|0\rangle = \exp\left(\frac{-\zeta\hat{a}_1^{\dagger 2} + \zeta^*\hat{a}_1^2}{2}\right)|0\rangle, \tag{2.64}$$

where $\hat{S}_\zeta$ is called the squeezing operator.

For this state we also have $\langle\hat{x}_i\rangle = 0 = \langle\hat{p}_i\rangle$, and so the vector of first moments $\bar{\boldsymbol{r}}$ is zero. The covariance matrix, in either basis $\hat{\boldsymbol{R}}'$ or $\hat{\boldsymbol{R}}$ (for one mode they are the same basis) is given by

$$\sigma_{\text{SQUEEZED}} = \begin{pmatrix} e^{-2|\zeta|} & 0 \\ 0 & e^{2|\zeta|} \end{pmatrix}. \tag{2.65}$$

Then the choice of name *squeezed state* makes sense when compared to the ground state. The Wigner function corresponding to this squeezed state is the result of squeezing the Wigner function of the ground state in the x-variable.

A **one-mode coherent state** [72] or displaced state is defined as

$$|\alpha\rangle = \hat{D}_\alpha|0\rangle = \exp\Big(\alpha\hat{a}_1^\dagger - \alpha^*\hat{a}_1\Big)|0\rangle. \tag{2.66}$$

where $\hat{D}_\alpha$ is called the displacement operator.

For this state the covariance matrix, in either basis $\hat{\boldsymbol{R}}'$ or $\hat{\boldsymbol{R}}$ (for one mode they are the same basis) is given by $\sigma = \mathbb{1}_2$. The vector of first moments $\bar{\boldsymbol{r}}$ is given by

$$\bar{\boldsymbol{r}} = \begin{pmatrix} \text{Re}(\alpha) \\ \text{Im}(\alpha) \end{pmatrix}. \tag{2.67}$$

The name *displaced state* is appropriately chosen. The Wigner function of the *displaced*

state is the result of displacing the center of the Wigner function of the ground state.

2.8.2 Time evolution

As we have discussed, Gaussian states can be represented by their first and second moments. A very useful property of these states is that they remain Gaussian if they are evolving under the influence of a quadratic Hamiltonian. A quadratic Hamiltonian, $\hat{H}$, can be written as the quadratic form

$$\hat{H} = \frac{1}{2}\hat{\boldsymbol{R}}^T F \hat{\boldsymbol{R}} + \boldsymbol{\alpha}^T \hat{\boldsymbol{R}}, \tag{2.68}$$

where F is a symmetric matrix and $\boldsymbol{\alpha}$ is a vector. The vector of operator $\hat{\boldsymbol{R}}$ was defined in Eq. (2.46) as $\hat{\boldsymbol{R}} = (\hat{q}_1, \hat{p}_1, \hat{q}_2, \hat{p}_2, \ldots, \hat{q}_N, \hat{p}_N)$. Alternatively, this Hamiltonian can be expressed in basis $\hat{\boldsymbol{R}}'$ given in (2.48).

The time evolution for the time-independent Hamiltonian (2.68) is given by $\hat{U} = e^{\mathrm{i}\hat{H}t}$. An initial Gaussian state $\hat{\rho}_0$ will then evolve as $\rho(t) = \hat{U}\hat{\rho}_0\hat{U}^\dagger$, and $\hat{\rho}(t)$ will remain Gaussian for all t. In this scenario, we can track the time evolution of the initial vector of first moments, $\bar{\boldsymbol{r}}_0$ and initial covariance matrix, σ_0. To do so, we need to define the two symplectic counterparts to the unitary evolution operator $\hat{U}$:

$$S(t) = \exp(\Omega F t), \tag{2.69}$$

$$\boldsymbol{d}(t) = \frac{\exp(\Omega F t) - \mathbb{1}_{2N}}{\Omega F}\Omega\,\boldsymbol{\alpha}. \tag{2.70}$$

In this equation one can especially appreciate the similarities between $S(t)$ and $\hat{U}$ when vector $\boldsymbol{\alpha}$ is identically zero. In that case, in Eq. 2.68, the matrix F would encode all the information about the quadratic form defining the Hamiltonian $\hat{H}$. Also, Ω can be thought as a counterpart of imaginary number i, since they both obey $\Omega^2 = -\mathbb{1}_2$ and $\mathrm{i}^2 = -1$. The correspondence between both $S(t)$ and $\hat{U}$ then becomes clear element-by-element.

Using the Heisenberg equation,

$$\frac{\mathrm{d}\hat{\boldsymbol{R}}}{\mathrm{dt}} = \mathrm{i}[\hat{H}, \hat{\boldsymbol{R}}] = \Omega(F\hat{\boldsymbol{R}} + \boldsymbol{\alpha}), \tag{2.71}$$

the evolution of the vector of first moments and covariance matrix can be derived. Ac-

cording to [50], a Gaussian state evolves in phase space as

$$\sigma(t) = S\sigma_0 S^T, \tag{2.72}$$
$$\bar{\boldsymbol{r}}(t) = S\bar{\boldsymbol{r}}_0 + \boldsymbol{d}. \tag{2.73}$$

As a summary, the correspondence between time evolution in the Hilbert space and the time evolution in phase-space is given by

$$\mathrm{i} \longrightarrow \Omega \tag{2.74}$$
$$\hat{\rho}_0 \longrightarrow \sigma_0, \bar{\boldsymbol{r}}_0, \tag{2.75}$$
$$\hat{H} \longrightarrow F, \boldsymbol{\alpha} \tag{2.76}$$
$$\hat{U} = e^{\mathrm{i}\hat{H}t} \longrightarrow S(t) = \exp(\Omega F t), \tag{2.77}$$
$$\boldsymbol{d}(t) = \frac{\exp(\Omega F t) - \mathbb{1}_{2N}}{\Omega F}\Omega\,\boldsymbol{\alpha} \tag{2.78}$$
$$\hat{\rho}(t) = \hat{U}\hat{\rho}_0\hat{U}^\dagger \longrightarrow \sigma(t) = S\sigma_0 S^T, \tag{2.79}$$
$$\bar{\boldsymbol{r}}(t) = S\bar{\boldsymbol{r}}_0 + \boldsymbol{d}. \tag{2.80}$$

Chapter 3

Cancelling the harvesting of correlations

In this Chapter, Section 3.4 and 3.5 are verbatim from the manuscript in preparation "Cancelling the harvesting of correlations in QFT", in collaboration with Abhisek Sahu and Eduardo Martín-Martínez.

3.1 Introduction

Understanding the entanglement and correlation content of quantum fields has been a research focus for the relativistic quantum information community in recent years [79]. Beyond its intrinsic fundamental value, this area of research connects with various fields of physics, such as black-hole thermodynamics [54, 17] or many-body physics [139].

In particular, there has been a spike of interest in correlation and entanglement harvesting protocols [137, 109, 110, 124, 22, 81, 23, 75, 112, 105, 86, 68, 111]. Originally proposed by [137], their applications range from metrology [23] to energy teleportation [59, 66] and communication [23]. In these protocols, two initially uncorrelated probes (non-relativistic in nature, such as a qubit or a quantum harmonic oscillator) interact with a quantum field for a certain amount of time. Typically the interaction is described via the Unruh-DeWitt model [31], introduced in Section 2.3. The resultant reduced state of the two probes will have *harvested* the correlations or entanglement present in the quantum field state. This correlation harvesting is possible even when spacelike separated probes couple briefly to the field [104]. Correlation harvesting protocols have been studied in multiple settings. For example, correlation harvesting has been studied for atomic systems [105], using quadratic

couplings for the detector-field interaction [111], in curved spacetimes [22, 68] or taking into account the delocalization of the centre of mass of the detectors [126].

However, there has been little research on how correlation harvesting is affected when more than two detectors couple to the quantum field [75, 68, 144]. The presence of extra detectors in the field may enhance or detract our ability to harvest quantum correlations. This knowledge is crucial to understand whether macroscopic devices, modelled as conglomerations of microscopic Unruh-DeWitt detectors [104], can ever have the ability to harvest entanglement or correlations from fields.

In this chapter, we study non-perturbatively how the correlation harvested by two detectors, A for Alice and B for Bob, is affected by the presence of N *interloper* detectors. This non-perturbative calculation is possible by considering δ-Dirac interactions - a useful and common approximation to describe strong and short interactions. However, this choice, considered in [119] for the particular case of zero *interloper* detectors, prevents entanglement harvesting [118]. Nevertheless, in this setting detectors can still harvest correlations [119].

Our main result is that we can cancel the correlations harvested by Alice and Bob by placing a single *interloper* detector in the right spacetime coordinates and with the right coupling strength. We provide an interpretation of this result and discuss a particular example of a correlation cancelling kind of scenario.

In this chapter, we also obtain, analytically, different correlation measures for Alice and Bob's detectors. We obtain the correlators of the two target detector's observables, their mutual information and their quantum discord. We analyze the different correlation measures dependence on 1) the coupling strength of the two target detectors, 2) their relative position, and 3) the presence of multiple *interlopers*.

3.2 Setup

3.2.1 The Model

Let us consider a real massless scalar field in a $(n+1)$ dimensional flat space-time. We can write it in terms of plane wave solutions to the Klein-Gordon equation as

$$\hat{\phi}(\boldsymbol{x},t)=\int \mathrm{d}^n\boldsymbol{k}\frac{1}{\sqrt{2(2\pi)^n|\boldsymbol{k}|}}\left[\hat{a}^\dagger_{\boldsymbol{k}}e^{\mathrm{i}(|\boldsymbol{k}|t-\boldsymbol{k}.\boldsymbol{x})}+\hat{a}_{\boldsymbol{k}}e^{-i(|\boldsymbol{k}|t-\boldsymbol{k}.\boldsymbol{x})}\right], \tag{3.1}$$

where the creation, $\hat{a}^\dagger_{\boldsymbol{k}}$, and annihilation operators, $\hat{a}_{\boldsymbol{k}}$, obey the canonical commutation relations

$$[\hat{a}_{\boldsymbol{k}}, \hat{a}_{\boldsymbol{k}'}] = [\hat{a}^\dagger_{\boldsymbol{k}}, \hat{a}^\dagger_{\boldsymbol{k}'}] = 0, \qquad [\hat{a}_{\boldsymbol{k}}, \hat{a}^\dagger_{\boldsymbol{k}'}] = \delta^n(\boldsymbol{k} - \boldsymbol{k}'). \tag{3.2}$$

We now consider N particle detectors coupled linearly to the field according to the Unruh-DeWitt model [136, 134], explained in detail in Section 2.3. The interaction Hamiltonian (in the interaction picture) for the ν-th detector is given by

$$\hat{H}_\nu(t) = \lambda_\nu \chi_\nu(t) \hat{m}_\nu(t) \otimes \int \mathrm{d}^n \boldsymbol{x} F_\nu(\boldsymbol{x} - \boldsymbol{x}_\nu) \hat{\phi}(t, \boldsymbol{x}), \tag{3.3}$$

so that all detectors $\nu \in \{1, \ldots, N\}$ are comoving with the quantization frame $(t, \boldsymbol{x})$ and their centres of mass are localized at positions $\boldsymbol{x}_\nu$. The spatial profile of the detectors are given by the real-valued distributions $F_\nu(\boldsymbol{x})$, called *smearing functions.* Here, $\hat{m}_\nu(t) := |g_\nu\rangle \langle e_\nu| e^{\mathrm{i}\Omega_\nu t} + |e_\nu\rangle \langle g_\nu| e^{-\mathrm{i}\Omega_\nu t}$ is the detector's monopole moment ($|g_\nu\rangle, |e_\nu\rangle$ denote respectively ground and excited states and Ω_ν is the energy gap between them) and λ_ν is each detector's coupling strength. The time dependence of the coupling is controlled by the switching functions $\chi_\nu(t)$.

The interaction Hamiltonian of the N detectors with the field is therefore

$$\hat{H}(t) = \sum_{\nu=1}^{N} \lambda_\nu \chi_\nu(t) \hat{\mu}_\nu(t) \otimes \int \mathrm{d}^n \boldsymbol{x} F_\nu(\boldsymbol{x} - \boldsymbol{x}_{\boldsymbol{\nu}}) \hat{\phi}(\boldsymbol{x}, t), \tag{3.4}$$

where $\hat{\mu}_\nu(t) = \mathbb{1}_1 \otimes \ldots \mathbb{1}_{\nu-1} \otimes \hat{m}_\nu(t) \cdots \otimes \mathbb{1}_N$. For brevity, we will naturally extend operators in the Hilbert space $\mathcal{H}_\nu \otimes \mathcal{H}_\phi$ to operators in $\otimes_\nu \mathcal{H}_\nu \otimes \mathcal{H}_\phi$ by dropping the tensor products of identity operators.

The time evolution generated by (3.4) is implemented by its time-ordered exponential

$$\hat{U} = \mathcal{T} \exp\left[-\mathrm{i} \int_{-\infty}^{\infty} \mathrm{d}t \hat{H}(t)\right], \tag{3.5}$$

so that if the initial state of the detectors-field system is given by the density operator $\hat{\rho}_0$, the final state is given by

$$\hat{\rho}_f = \hat{U} \hat{\rho}_0 \hat{U}^\dagger, \tag{3.6}$$

and the final state of the detectors after the interaction can be obtained by tracing over the field degrees of freedom $\hat{\rho}_{\mathrm{D}} = \mathrm{tr}_{\hat{\phi}}[\hat{\rho}_f]$. We can also obtain the density matrix of any detector or group of detectors from the above expression by tracing over the appropriate

detector degrees of freedom.

3.2.2 Non-perturbative time evolution of N detectors

The problem of calculating the unitary $\hat{U}$ in Eq. (3.5) is very commonly approached perturbatively, where the expansion of the exponential is carried out up to a certain power of λ_ν. In some special cases, a non-perturbative calculation of Eq. (3.5) is possible. For example, in [119]), a delta switching function $\chi_\nu(t) := \eta_\nu \delta(t - t_\nu)$ has been used to find an exact expression for $\hat{U}$ and to study the harvesting of correlations from coherent field states using two detectors. This delta-switching function captures the limit of a very strong and short interaction. The parameter η_ν has the dimensions of length and denotes the strength of the interaction.

However, in some cases, this "ideal" approximation of delta-coupling can be a double-edged sword, even in its range of validity. Although it allows for non-perturbative formulas [119], it may sometimes hinder the possibility for entanglement harvesting. A relatively recent paper provided a no-go theorem for couplings that cannot harvest entanglement [118]. Single delta couplings — spoiler alert, the ones we are going to use — are particular cases of *simply generated* time evolution, which induce entanglement-breaking channels and prevent entanglement extraction. Entanglement harvesting in our scenario is therefore impossible. Nonetheless, as we will see as the chapter progresses, it is indeed possible to harvest both classical and quantum correlations with a single delta switching function.

After this small detour, we go back to computing the exact expression for the density matrix of N detectors, generalizing the result in [119]. Initially, the detectors are taken to be in their respective ground states. We consider the field initialized in an arbitrary coherent state, and the initial state of the field-detectors system to be $\hat{\rho}_0 = |\psi_0\rangle\langle\psi_0|$ with

$$|\psi_0\rangle = \bigotimes_{\nu=1}^{N} |g_\nu\rangle \otimes |\beta_0(\boldsymbol{k})\rangle \,. \tag{3.7}$$

The coherent state $|\beta_0(\boldsymbol{k})\rangle$ is characterized by a coherent amplitude distribution $\beta_0(\boldsymbol{k})$ defined as

$$|\beta_0(\boldsymbol{k})\rangle = \hat{D}_{\beta_0(\boldsymbol{k})} |0\rangle = \exp\left(\int \mathrm{d}^n \boldsymbol{k} \left[\beta_0(\boldsymbol{k}) \hat{a}^\dagger_{\boldsymbol{k}} - \beta_0(\boldsymbol{k})^* \hat{a}_{\boldsymbol{k}} \right] \right) |0\rangle \,, \tag{3.8}$$

where $\hat{D}_{\beta_0(\boldsymbol{k})}$ is a multimode displacement operator [120]. Note that the vacuum state of the field is the coherent state of distribution $\beta_0(\boldsymbol{k}) = 0 \ \forall \boldsymbol{k}$. The various properties of

coherent states have been given in Section 2.2

The initial state (3.2.2) will evolve in the interaction picture as $|\psi_f\rangle = \hat{U}\,|\psi_0\rangle$. Subsequently, we can obtain the state of the detectors by tracing over the field degrees of freedom:

$$\hat{\rho}_{\{\nu\}} = \mathrm{Tr}_{\hat{\phi}}[|\psi\rangle\,\langle\psi|]. \tag{3.9}$$

Each detector couples with the field through a delta-switching function

$$\chi_\nu(t) = \eta_\nu \delta(t - t_\nu), \tag{3.10}$$

where the constant η_ν quantifies the strength of the kick [119]. We can assume, without loss of generality, $t_1 \leq t_2 \leq \cdots \leq t_N$, i.e. the detector with label ν will be the νth to interact with the field.

Also, unless explicitly stated otherwise, we will work in the convenient basis $\{|1_\nu\rangle\,, |-1_\nu\rangle\}$ defined by

$$|1_\nu\rangle \coloneqq \frac{1}{\sqrt{2}}\big(\,|g_\nu\rangle + e^{i\Omega_\nu t_\nu}\,|e_\nu\rangle\,\big), \qquad |-1_\nu\rangle \coloneqq \frac{1}{\sqrt{2}}\big(\,|g_\nu\rangle - e^{i\Omega_\nu t_\nu}\,|e_\nu\rangle\,\big), \tag{3.11}$$

that we will denote throughout as $\{|s_\nu\rangle\}$, with $s_\nu = \pm 1$.

Considering the switching function (3.10) we calculate in Appendix A.2 a non-perturbative expression for $\hat{U}$ as given in (3.5). It turns out that $\hat{U}$ factorizes as a product of controlled unitaries:

$$\hat{U} = \hat{U}_N \hat{U}_{N-1} \ldots \hat{U}_1, \tag{3.12}$$

$$\hat{U}_\nu = |1_\nu\rangle\langle 1_\nu| \otimes \hat{D}_{+\beta_\nu(\boldsymbol{k})} + |-1_\nu\rangle\langle -1_\nu| \otimes \hat{D}_{-\beta_\nu(\boldsymbol{k})}. \tag{3.13}$$

Before diving into how the complex function $\beta_\nu(\boldsymbol{k})$ is defined, we can already interpret how a general set of detectors coupled via a single delta acts on the field. If a detector ν is in state $|1_\nu\rangle$, a multimode displacement operator with coherent amplitude $\beta_\nu(\boldsymbol{k})$, as defined in (3.8), will act on the field. Similarly, if the detector is in state $|-1_\nu\rangle$, the field will be displaced with a coherent amplitude $-\beta_\nu(\boldsymbol{k})$.

This process can be visualized in phase-space considering the action of detector ν in one particular mode, $\boldsymbol{k_0}$, as depicted in Figure 3.1. Even though singling out a mode among a continuous range of frequencies is not completely physical, let us still do it, because 1) the math is exactly the same as one of a harmonic oscillator, 2) it will help illustrate the effect of the detector coupling on the field and 3) it will help us understand the final density matrix in equation (3.18).

Initially, the mode $\boldsymbol{k_0}$ of the field is in a coherent state of coherent amplitude $\beta_0(\boldsymbol{k_0})$ (a particular complex outcome of the distribution $\beta_0(\boldsymbol{k})$). In phase-space, as explained in Secion 2.8.1, this is mathematically a Gaussian centered at point $x = \mathrm{Re}(\beta_0(\boldsymbol{k_0}))$ and $y = \mathrm{Im}(\beta_0(\boldsymbol{k_0}))$ with covariance matrix equal to the identity (in Figure 3.1, blue circles in both sides).

Then depending on whether the νth detector is in state $|1_\nu\rangle$ or $|{-1_\nu}\rangle$, the field mode will suddenly, after t_ν be displaced in phase space. The length and angle of displacement will follow the properties of a multiplication of displacement operators:

$$\hat{U}_\nu\big(\,|1_\nu\rangle \otimes |\beta_0(\boldsymbol{k_0})\rangle\,\big) = |1_\nu\rangle \otimes \hat{D}_{\beta_1(\boldsymbol{k_0})}\hat{D}_{\beta_0(\boldsymbol{k_0})}\,|0\rangle = |1_\nu\rangle \otimes e^{\mathrm{i}\xi}\,|\beta_0(\boldsymbol{k_0}) + \beta_1(\boldsymbol{k_0})\rangle\,, \tag{3.14}$$

$$\hat{U}_\nu\big(\,|{-1_\nu}\rangle \otimes |\beta_0(\boldsymbol{k_0})\rangle\,\big) = |1_\nu\rangle \otimes \hat{D}_{-\beta_1(\boldsymbol{k_0})}\hat{D}_{\beta_0(\boldsymbol{k_0})}\,|0\rangle = |1_\nu\rangle \otimes e^{-\mathrm{i}\xi}\,|\beta_0(\boldsymbol{k_0}) - \beta_1(\boldsymbol{k_0})\rangle\,, \tag{3.15}$$

where $\xi = \mathrm{Im}(\beta_1(\boldsymbol{k_0})^*\beta_0(\boldsymbol{k_0}))$. If the νth detector is in state $|1_\nu\rangle$ the resultant state of the mode in phase-space will be a Gaussian with its center displaced to the point with coordinates $x = \mathrm{Re}(\beta_0(\boldsymbol{k_0}) + \beta_\nu(\boldsymbol{k_0}))$ and $y = \mathrm{Im}(\beta_0(\boldsymbol{k_0}) + \beta_\nu(\boldsymbol{k_0}))$ (in Figure 3.1, red circle on left side). Similarly if the νth detector is in state $|{-1_\nu}\rangle$, the field state will suddenly, after t_ν be displaced in phase space to point with coordinates $x = \mathrm{Re}(\beta_0(\boldsymbol{k_0}) - \beta_\nu(\boldsymbol{k_0}))$ and $y = \mathrm{Im}(\beta_0(\boldsymbol{k_0}) - \beta_\nu(\boldsymbol{k_0}))$ (in Figure 3.1, red circle in right side). The effect of the coupling of νth detectors on the state of the field is similar. Depending on the state of the probe, the field will be "kicked" in phase space in the corresponding direction.

Now that we have a mental image of the situation let us open the black box of $\beta_\nu(\boldsymbol{k})$. How do the parameters of the detectors and its coupling to the field affect the field's trajectory in phase-space? Mathematically, their relation is given by

$$\beta_\nu(\boldsymbol{k}) = -\mathrm{i}\eta_\nu\lambda_\nu\frac{\tilde{F}_\nu(-\boldsymbol{k})}{\sqrt{2|\boldsymbol{k}|}}e^{\mathrm{i}(|\boldsymbol{k}|t_\nu - \boldsymbol{k}.\boldsymbol{x_\nu})}, \tag{3.16}$$

with $\tilde{F}_\nu(\boldsymbol{k})$ being the Fourier transform of the smearing function

$$\tilde{F}_\nu(\boldsymbol{k}) \coloneqq \frac{1}{\sqrt{(2\pi)^n}}\int \mathrm{d}^n\boldsymbol{k}F(\boldsymbol{x})e^{\mathrm{i}\boldsymbol{k}\cdot\boldsymbol{x}}. \tag{3.17}$$

We see then that the "length" of the displacements in phase-space depends on the strength of the coupling, λ_ν, and the strength of the kick in the delta-switching function, η_ν. Since these two parameters always appear together in the rest of the chapter, we can define an effective coupling strength, $\tilde{\lambda}_\nu \coloneqq \eta_\nu\lambda_\nu$, that we will use for notational brevity from now on. Another factor that contributes to $\beta_\nu(\boldsymbol{k})$ is the Fourier transform of the smearing

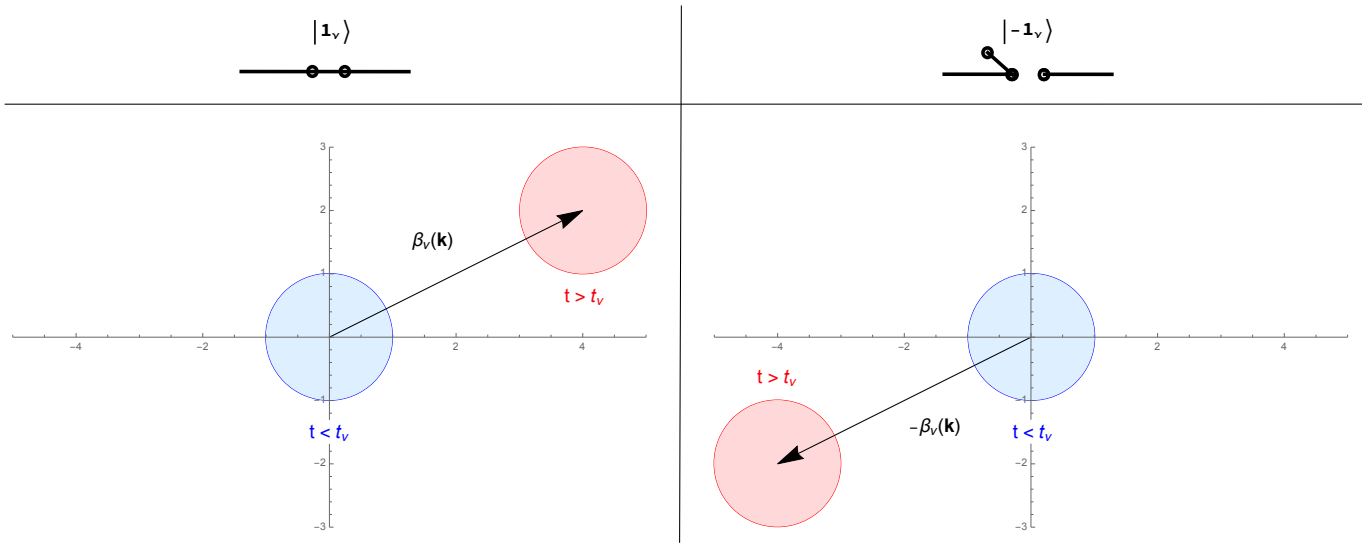

Figure 3.1: Visual representation of the controlled unitary in 3.13.
On the left of this figure we show the action of unitary U_ν on mode $\boldsymbol{k_0}$ when the νth detector is in state $|1_\nu\rangle$. On the right we show the action of unitary U_ν on mode $\boldsymbol{k_0}$ when the νth detector is in state $|-1_\nu\rangle$. Initially, at $t < t_\nu$, mode $\boldsymbol{k_0}$ in phase-space is a Gaussian centered at point $x = \mathrm{Re}(\beta_0(\boldsymbol{k_0}))$ and $y = \mathrm{Im}(\beta_0(\boldsymbol{k_0}))$ with covariance matrix equal to the identity. In both the right and left sides this Gaussian is represented by a blue circle of unit one at the origin of coordinates, which is chosen to be precisely $x = \mathrm{Re}(\beta_0(\boldsymbol{k_0}))$ and $y = \mathrm{Im}(\beta_0(\boldsymbol{k_0}))$. On the left we use a red circle to represent the state of mode $\boldsymbol{k_0}$ at time $t > t_\nu$, after the detector ν (initially in state $|1_\nu\rangle$) has interacted with the field. in this case, the final state of the mode is a Gaussian with its center displaced to point $x = \mathrm{Re}(\beta_0(\boldsymbol{k_0}) + \beta_\nu(\boldsymbol{k_0}))$ and $y = \mathrm{Im}(\beta_0(\boldsymbol{k_0}) + \beta_\nu(\boldsymbol{k_0}))$ and covariance matrix equal to the identity. On the left we use a red circle to represent the state of mode $\boldsymbol{k_0}$ at time $t > t_\nu$, after the detector ν (initially in state $|-1_\nu\rangle$) has interacted with the field. in this case, the final state of the mode is a Gaussian with its center displaced to point $x = \mathrm{Re}(\beta_0(\boldsymbol{k_0}) - \beta_\nu(\boldsymbol{k_0}))$ and $y = \mathrm{Im}(\beta_0(\boldsymbol{k_0}) - \beta_\nu(\boldsymbol{k_0}))$ and covariance matrix equal to the identity.

function, which determines how strongly the detector is coupled to each of the field modes. As we discussed in Section 2.6, the Fourier transform of a localized smearing function has a decreasing tail. This means that the most energetic modes will be less displaced by the "kick" of detector ν. Only the low energy modes will be displaced. Finally, the apparent "divergence" of $\beta_\nu(\boldsymbol{k})$ at $\boldsymbol{k}=0$ originates from singling out a particular mode, when $\beta_\nu(\boldsymbol{k})$ only makes sense as a distribution. When integrated, other terms, like the Jacobian, will smooth out this irregularity - the physics of a 3+1 scalar field does not break down at low energy.

After this analysis, we can calculate the final state of the detectors-field system. Applying the unitary $\hat{U}$ from (3.12) on the initial state $|\psi_0\rangle$ we obtain the joint final state, $|\psi_f\rangle$ for the detector-field system as

$$|\psi_f\rangle = \frac{1}{2^{N/2}} \sum_{\vec{s}} \exp\Big[\mathrm{i} \sum_{i=0}^{N} \sum_{j\geq i}^{N} s_j s_i \,\mathrm{Im}(T_{ij})\Big] |\vec{s}\rangle \otimes \Big| \sum_{i=0}^{N} s_i \beta_i(\boldsymbol{k}) \Big\rangle. \tag{3.18}$$

Here we have denoted the sum over $\vec{s} \coloneqq (s_1, \ldots, s_N)$ for a sum over the binary N-tuples $(s_1, \ldots, s_N) \in \{-1, 1\}^N$. The second and third sums are over the indices i which run from 0 to N, and $s_0 \coloneqq 1$ throughout - to account for the initial state of the field being an arbitrary coherent state of amplitude $\beta_0(\boldsymbol{k})$.

The coherent state $\left| \sum_{i=0}^{N} s_i \beta_i(\boldsymbol{k}) \right\rangle$ is characterized by the distribution result of the sum inside the ket. As we discussed, this state is the result of the displacements due to the "kick" of each detector ν, depending on whether the detector ν is in state $s_\nu = 1$ or $s_\nu = -1$. Finally, just like we saw in equation (3.14), there is always a phase that appears when multiplying displacement operators. This phase only depends on T_{ij}, which takes the form

$$T_{ij} \coloneqq \int \mathrm{d}^n \boldsymbol{k} \beta_j(\boldsymbol{k}) \beta_i^*(\boldsymbol{k}) =: \frac{\zeta_{ij}}{4} + \mathrm{i}\frac{\xi_{ij}}{4}, \tag{3.19}$$

where we have introduced ξ_{ij} and ζ_{ij} since it will be convenient later. Therefore, the final state in Eq. (3.18) will only depend on T_{ij}, which is given by the ìnner products of the "displacement distributions", $\beta_i(\boldsymbol{k})$. These "displacement distributions" either correspond to the initial state of the field, $\beta_0(\boldsymbol{k})$ or to a detector $\beta_i(\boldsymbol{k})$, with $i > 0$. The reader may refer to Appendix A.2 for the detailed derivation.

Tracing over the field in Eq. (3.18) we obtain the joint state of the N detectors:

$$\hat{\rho}_{\mathrm{D}} = \frac{1}{2^N}\sum_{\vec{s},\vec{s}'}\exp\left[\sum_{i=0}^{N} T_{ii}(s_i s_i' - 1) + \sum_{i,j=0,i>j}^{N}(T_{ij}s_j - T_{ji}s_j')(s_i' - s_i)\right]\left|\vec{s}\right\rangle\left\langle\vec{s}'\right|. \tag{3.20}$$

From this general density matrix, one can obtain the reduced density matrix of any pair of detectors (this general reduced state is derived in Appendix A.2) required to study correlation harvesting. In the next section, we specify two target detectors corresponding to Alice and Bob, and we show how *interloper* detectors could sabotage their harvesting of correlations.

3.3 Cancelling of correlations

For the results of this thesis we consider the following situation. Alice and Bob control one detector each, labeled A and B. Alice's detector couples to the field before Bob's detector, i.e. $t_{\mathrm{A}} < t_{\mathrm{B}}$. Also, we consider that there are N *interloper* detectors, which couple to the field at times $t_{\mathrm{A}} \leq t_j \leq t_{\mathrm{B}}$ for every $j = 1, \ldots, N$.

In that case we obtain a simpler expression particularizing (3.20):

$$\hat{\rho}_{\mathrm{AB}} = \sum_{s_{\mathrm{A}},s_{\mathrm{B}},s_{\mathrm{A}}',s_{\mathrm{B}}'}\Theta(s_{\mathrm{A}},s_{\mathrm{B}},s_{\mathrm{A}}',s_{\mathrm{B}}')\exp[\mathrm{i}\,\theta_0(s_{\mathrm{A}},s_{\mathrm{B}},s_{\mathrm{A}}',s_{\mathrm{B}}')]\prod_{j\neq \mathrm{A},\mathrm{B}}\cos\theta_j(s_{\mathrm{A}},s_{\mathrm{B}},s_{\mathrm{A}}',s_{\mathrm{B}}')|s_{\mathrm{A}},s_{\mathrm{B}}\rangle\langle s_{\mathrm{A}}',s_{\mathrm{B}}'|. \tag{3.21}$$

In this equation we have

$$\Theta(s_{\mathrm{A}},s_{\mathrm{B}},s_{\mathrm{A}}',s_{\mathrm{B}}') = \frac{1}{4}\exp[T_{\mathrm{BB}}(s_{\mathrm{B}}s_{\mathrm{B}}' - 1) + T_{\mathrm{AA}}(s_{\mathrm{A}}s_{\mathrm{A}}' - 1) + (s_{\mathrm{B}} - s_{\mathrm{B}}')(T_{\mathrm{AB}}s_{\mathrm{A}}' - T_{\mathrm{BA}}s_{\mathrm{A}})] \tag{3.22}$$

and

$$\theta_0 = \frac{1}{2}(s_{\mathrm{A}} - s_{\mathrm{A}}')\xi_{0\mathrm{A}} + \frac{1}{2}(s_{\mathrm{B}} - s_{\mathrm{B}}')\xi_{0\mathrm{B}}, \tag{3.23}$$

$$\theta_j = \frac{1}{2}(s_{\mathrm{B}} - s_{\mathrm{B}}')\xi_{j\mathrm{B}}. \tag{3.24}$$

Examining this expression, we realize that we can easily set some of $\cos\theta_j(s_{\mathrm{A}},s_{\mathrm{B}},s_{\mathrm{A}}',s_{\mathrm{B}}')$ to zero. This can only be done when $s_{\mathrm{B}} \neq s_{\mathrm{B}}'$, i.e. for non-diagonal terms in Bob's detector. Let us pick a preferred Interloper, labeled as I. For $s_{\mathrm{B}} \neq s_{\mathrm{B}}'$, we have that θ_{I} is equal to

$\pm\xi_{\text{IB}}$. If we chose ξ_{IB} to be an odd multiple of $\pi/2$, the corresponding coefficient in $\hat{\rho}_{\text{AB}}$ vanishes. Thus, for this particular choice of ξ_{IB}, the only terms in the density matrix that survive are diagonal in Bob's detector, that is, the terms for entries $s_{\text{B}} = s'_{\text{B}}$. For those elements (i.e. for elements such that $s_{\text{B}} = s'_{\text{B}}$) we have

$$\Theta = \frac{1}{4}\exp\left[\frac{\zeta_{\text{AA}}}{4}(s_{\text{A}}s'_{\text{A}} - 1)\right], \tag{3.25}$$

$$\theta_0 = \frac{1}{2}(s_{\text{A}} - s'_{\text{A}})\xi_{0\text{A}}, \tag{3.26}$$

$$\theta_j = 0. \tag{3.27}$$

This means the matrix elements of $\hat{\rho}_{\text{AB}}$ are independent of the value of s_{B}. Moreover, the density matrix is

$$\hat{\rho}_{\text{AB}} = \left(\frac{1}{2}\sum_{s_{\text{A}},s'_{\text{A}}}\exp\left[\frac{\zeta_{\text{AA}}}{4}(s_{\text{A}}s'_{\text{A}} - 1) + \mathrm{i}\frac{\xi_{0\text{A}}}{2}(s_{\text{A}} - s'_{\text{A}})\right]|s_{\text{A}}\rangle\langle s'_{\text{A}}|\right) \otimes \frac{1}{2}\mathbb{1}_{\text{B}}. \tag{3.28}$$

Thus we see that, when ξ_{IB} is an odd multiple of $\pi/2$, we have a product state, which means that Alice's and Bob's detectors are not correlated. In fact, Bob's detector is the maximally mixed state. The action of the Interloper's detector on the field provokes the "flooding"of Bob's detector with entropy. Since the state of the whole system (field and detectors) is pure, and Bob's reduced state is the maximally mixed state, Bob must be maximally entangled to some system.

Since the reduced state of Alice and Bob is a product state, Bob cannot be entangled with Alice. The only candidates then are the other interloper detectors, the field or both. However, it is impossible for Bob to be entangled to any of the other detectors. According to the results in the no-go theorem [118], two-qubit detectors interacting with the field with a delta-Dirac coupling (a particular case of simple generated unitary) cannot harvest entanglement. Necessarily, Bob's detector is maximally entangled with some bipartite sector of the field. Our interpretation then seems correct: by coupling instantaneously to the field, the Interloper detector modifies the field state so that when Bob's detector interaction is switched on, Bob's detector is "flooded" with entropy. Bob's detector cannot be correlated with anything but the field.

Then, if Alice and Bob tried to counteract the Interloper's action using extra detectors coupled through delta-couplings, it would be in vain, since Bob cannot be correlated with anybody. It is possible that if those extra detectors were allowed to couple beyond the delta limit, they might be able to somewhat undo the action of the interloper. However, these considerations are out of the scope of this thesis. In any case, the presence of

many detectors, at least with delta-couplings, will not tend to benefit Alice and Bob. If there are enough detectors (i.e. if N is big enough) and the detectors have somewhat random parameters, then we have $\prod_{j\neq \mathrm{A,B}} |\cos\theta_j(s_\mathrm{A}, s_\mathrm{B}, s'_\mathrm{A}, s'_\mathrm{B})| \to 0$. The presence of enough detectors leads to the product state in (3.28): they exponentially mess up any harvesting protocol between Alice and Bob. It is known that quantum information is very fragile and sensitive to noise, and so this result is not surprising. However, the analytic formula in (3.28) provides us with some insight into the amount of noise introduced by extra detectors.

So far, we have talked about what happens to Bob's detector when the Interloper's detector or many interloper detectors mess with it. In the many-detector case, it just seems that noise prevents Alice and Bob from becoming correlated. But how is this cancellation happening when there is a single Interloper? Is the Interloper detector communicating with Bob? These questions will be answered at in subection 3.3.2. However, first, we will show that a cancelling scenario is feasible: the parameter ξ_{IB} can always be fount to be equal to a multiple of $\pi/2$.

3.3.1 Conditions for correlation harvesting cancelling

As derived in Appendix A.5, we can rewrite ξ_{IB} as a convolution smearing functions. Defining the spatial separation between the Interloper's and Bob's detector, $\boldsymbol{X} = \boldsymbol{x}_\mathrm{B} - \boldsymbol{x}_\mathrm{I}$, and the time delay from the the Interloper's action to Bob's detector activation, $T = t_\mathrm{B} - t_\mathrm{I}$, we find, as in Eq. (A.74):

$$\xi_{\mathrm{IB}} = 2\tilde{\lambda}_\mathrm{I}\tilde{\lambda}_\mathrm{B}\int \mathrm{d}\boldsymbol{x'}\mathrm{d}\boldsymbol{z'}F_\mathrm{I}(\boldsymbol{z'})F_\mathrm{B}(\boldsymbol{x'}+\boldsymbol{z'})\int_0^\infty \mathrm{d}k\left(\frac{k}{|\boldsymbol{x'}-\boldsymbol{X}|}\right)^{\frac{n}{2}-1} J_{\frac{n}{2}-1}(k|\boldsymbol{x'}-\boldsymbol{X}|)\sin(kT). \tag{3.29}$$

In this expression $J_{\frac{n}{2}-1}(k|\boldsymbol{x'}-\boldsymbol{X}|)$ is a Bessel function.

The only requirement for the set of parameters to exist is that the expression inside integral is different from 0. In that case we can obtain $\xi_{\mathrm{IB}} = (n+1)\frac{\pi}{2}$ for some integer n if we the adjust the effective coupling strength $\tilde{\lambda}_\mathrm{I}$. To analyze the necessary order of magnitude $\tilde{\lambda}_\mathrm{I}$ we first change to a dimensionless version of the problem. We choose the length scale σ in which the interaction (which is somewhat local) of each of the detectors and the field is strongly supported. That means, more formally, that for $|\boldsymbol{x}| \gg \sigma \Rightarrow F(\boldsymbol{x}) \to 0$ for the smearing function $F(\boldsymbol{x})$. Through a change to dimensionless integration variables in the k integral in Eq. (3.29) we obtain that in $(n+1)$ dimensions

$$\xi_{\mathrm{IB}} = \frac{\tilde{\lambda}_\mathrm{I}\tilde{\lambda}_\mathrm{B}}{\sigma^{n-1}}\mathcal{I}, \tag{3.30}$$

where,

$$\mathcal{I} = 2\int \mathrm{d}\boldsymbol{x}'\mathrm{d}\boldsymbol{z}' F_{\mathrm{I}}(\boldsymbol{z}')F_{\mathrm{B}}(\boldsymbol{x}'+\boldsymbol{z}')\int \mathrm{d}(k\sigma)\, J_{\frac{n}{2}-1}(k|\boldsymbol{x}'-\boldsymbol{X}|)\sin(kT)\left(\frac{k\sigma}{|\boldsymbol{x}'-\boldsymbol{X}|/\sigma}\right)^{\frac{n}{2}-1}. \tag{3.31}$$

Importantly, $\mathcal{I}$ is a dimensionless geometric factor that depends on the smearing functions of the detectors and the separations $|\boldsymbol{X}|$ and T. This factor cannot be very large since the smearing functions are L^1 functions normalized to one, so one would expect that this geometric factor is indeed roughly of order 1 for three or less spatial dimensions.

In summary, in order for the interloper to completely sabotage the correlations between Alice and Bob, the interloper's coupling strength has to scale as

$$\tilde{\lambda}_{\mathrm{I}} \sim \frac{\sigma^{n-1}}{\tilde{\lambda}_{\mathrm{B}}}. \tag{3.32}$$

Cranking up or down the effective coupling strength of the Interloper's detector, we could find that ξ_{IB} is a multiple of $\pi/2$, which is a sufficient condition to cancel correlation harvesting. Notice that all these formulas are independent of detector A: Alice can do very little to avoid the sabotage of the correlation harvesting protocol. If Bob wants to make it difficult for the Interloper to sabotage the protocol, then Bob has to try to couple as nimbly as possible to the field. Of course, this also goes in detriment of the amount of correlation that Alice and Bob can extract from the field since the amount of correlation (in leading order) is proportional to $\tilde{\lambda}_{\mathrm{A}}\tilde{\lambda}_{\mathrm{B}}$. The safest protocol for correlation extraction, in this case, is to consider that Alice couples very strongly to the field. Using a small coupling for Bob, one would obtain the same leading order of amount correlation extracted from the field.

In the next section, we are going to choose a hard-sphere smearing for the Interloper's and Bob's detector in three spatial dimensions. We show that we can achieve $\xi_{\mathrm{IB}} = \pi/2$ by controlling their coupling with the field exclusively. By analyzing this case in depth, namely the spacetime positions where the Interloper can sabotage Alice and Bob correlation harvesting protocol, we will learn whether this phenomenon is due to signalling, partially signalling, or something entirely different.

3.3.2 Example

First we consider the smearing function of Bob's and the Interloper's detectors to be a normalised hard sphere in 3 spatial dimensions:

$$F_\nu(\boldsymbol{x}) = \begin{cases} \frac{3}{4\pi\sigma^3} & |\boldsymbol{x}| \leq \sigma \\ 0 & |\boldsymbol{x}| > \sigma \end{cases}. \tag{3.33}$$

Let us recall that the spatial separation between the Interloper's and Bob's detector $|\boldsymbol{X}| = |\boldsymbol{x}_{\text{B}} - \boldsymbol{x}_{\text{I}}|$ and the time delay from the Interloper's action to Bob's detector activation $T = t_{\text{B}} - t_{\text{I}}$. In Appendix A.5 we show that

$$\xi_{\text{IB}} = \begin{cases} 0 & \frac{||\boldsymbol{X}|-|T||}{2\sigma} \geq 1 \\ \tilde{\lambda}_{\text{I}}\tilde{\lambda}_{\text{B}}\dfrac{3\sqrt{2\pi}}{\sigma|\boldsymbol{X}|}(\frac{1}{5} - \delta_- + \delta_-^{3/2} - \frac{1}{5}\delta_-^{5/2}) & \frac{|\boldsymbol{X}|+|T|}{2\sigma} \geq 1 \\ \tilde{\lambda}_{\text{I}}\tilde{\lambda}_{\text{B}}\dfrac{3\sqrt{2\pi}}{\sigma|\boldsymbol{X}|}(\delta_+ - \delta_+^{3/2} + \frac{1}{5}\delta_+^{5/2} - \delta_- + \delta_-^{3/2} - \frac{1}{5}\delta_-^{5/2}) & \frac{|\boldsymbol{X}|+|T|}{2\sigma} \leq 1 \end{cases} \tag{3.34}$$

with $\delta_+ = \left(\frac{|\boldsymbol{X}|+|T|}{2\sigma}\right)^2$ and $\delta_- = \left(\frac{|\boldsymbol{X}|-|T|}{2\sigma}\right)^2$.

To cancel correlations we need to prove that we can modify the Interloper's detector parameters so that $\xi_{\text{IB}} = (2n+1)\pi/2$ for some integer n. The parameters that we can modify are the space and time coordinates of the Interloper's detector, $\boldsymbol{x}_{\text{I}}$ and t_{I} (which appear in $|\boldsymbol{X}|$ and T respectively) and its effective coupling strength $\tilde{\lambda}_{\text{I}}$. The unchangeable parameters are Bob's effective coupling strength $\tilde{\lambda}_{\text{B}}$ and the spatial extent of both detectors, σ, which provides the spatial scale in this scenario.

From Eq. (3.34) we observe that for very small values of $\tilde{\lambda}_{\text{I}}$, parameter ξ_{IB} is very small in absolute value and it would not be possible for it to be a multiple of $\pi/2$. It is possible, though, to find the coupling strength values for which it is guaranteed that $\xi_{\text{IB}} = \frac{\pi}{2}$ for some $\boldsymbol{x}_{\text{I}}$ and t_{I}. The strategy to prove that these $\boldsymbol{x}_{\text{I}}$ and t_{T} exist and how that restricts the rest of parameters is to prove that for each $\sigma, \tilde{\lambda}_{\text{I}}$ and $\tilde{\lambda}_{\text{B}}$, the maximum for function ξ_{IB}, denoted as ξ^*_{IB}, can be greater than $\frac{\pi}{2}$. With simple analysis, it can be shown that the maxima of ξ_{IB} occurs when $|\boldsymbol{X}| = T \approx 0.57673\sigma$. For these values, the condition $\xi^*_{\text{IB}} \geq \pi/2$ can be written as,

$$\tilde{\lambda}_{\text{I}} > 0.78\frac{\sigma^2}{\tilde{\lambda}_{\text{B}}}. \tag{3.35}$$

As long as this condition is met, we can find some spacetime position for detector I for which $\xi_{\text{IB}} = \pi/2$, due to the continuity of the function ξ_{IB}. In Figure 3.2 we plot a plane at $\pi/2$ (in blue) and function ξ_{IB} (in orange) for parameters which obey the condition (3.35): $\sigma = 1$, $\tilde{\lambda}_{\text{B}} = 2$ and $\tilde{\lambda}_{\text{I}} = 2$. In this plot we observe that $\pi/2$ is achieved within the region $||X| - T| \leq 2\sigma$, i.e. in the region where B and I are lightlike separated.

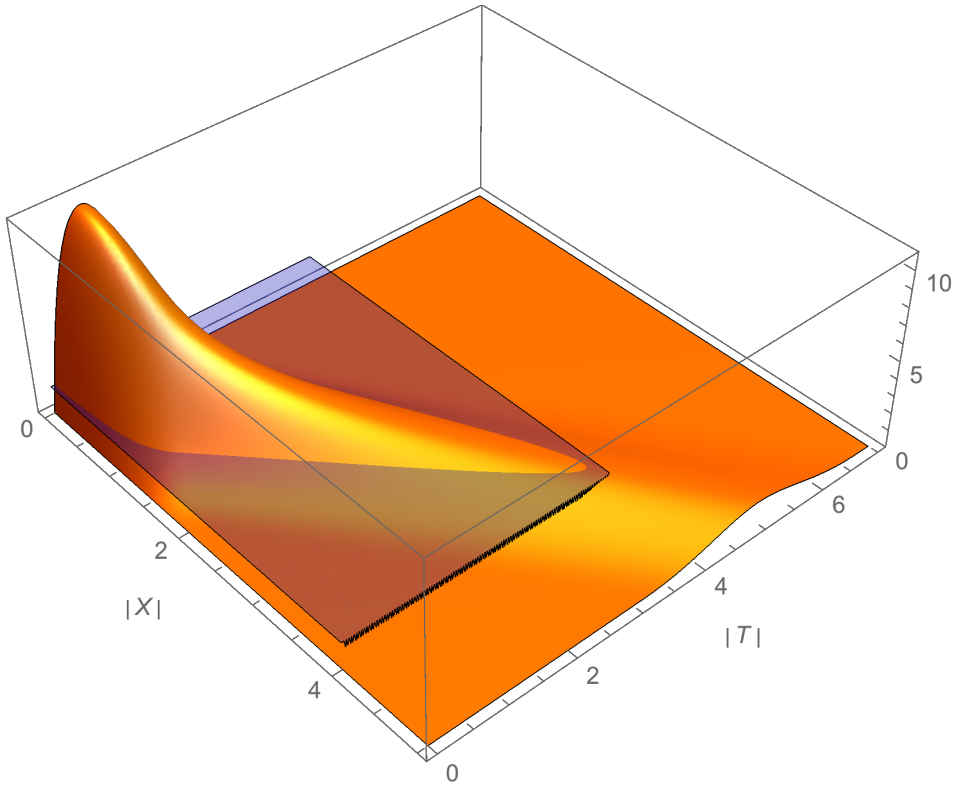

Figure 3.2: Plot a plane at $\pi/2$ (in blue) and function ξ_{IB} (in orange) for $\sigma = 1$, $\tilde{\lambda}_{\text{B}} = 2$ and $\tilde{\lambda}_{\text{I}} = 2$.
As these parameters obey the condition (3.35), as expected there is intersection between the plane and function ξ_{IB} at points with $||X| - T| \leq 2\sigma$, which determines points in which detectors B and I are lightlike separated.

In fact, looking once more at formula (3.34), it is evident that if Bob and the Interloper were spacelike or purely timelike separated, sabotage would be impossible since ξ_{IB} is identically zero. The Interloper's detector must then be placed in the past cone of Bob's detector and lightlike connected to it. In Figure 3.3, we depict a possible scenario between Alice, Bob and the Interloper's detectors plotting the x-coordinate of the detectors versus

time. Two curves represent some positions for the Interloper's detector center for which $\xi_{\text{IB}} = \pi/2$, with ξ_{IB} defined in 3.34. For those positions, the Interloper would cancel correlation harvesting between Alice and Bob.

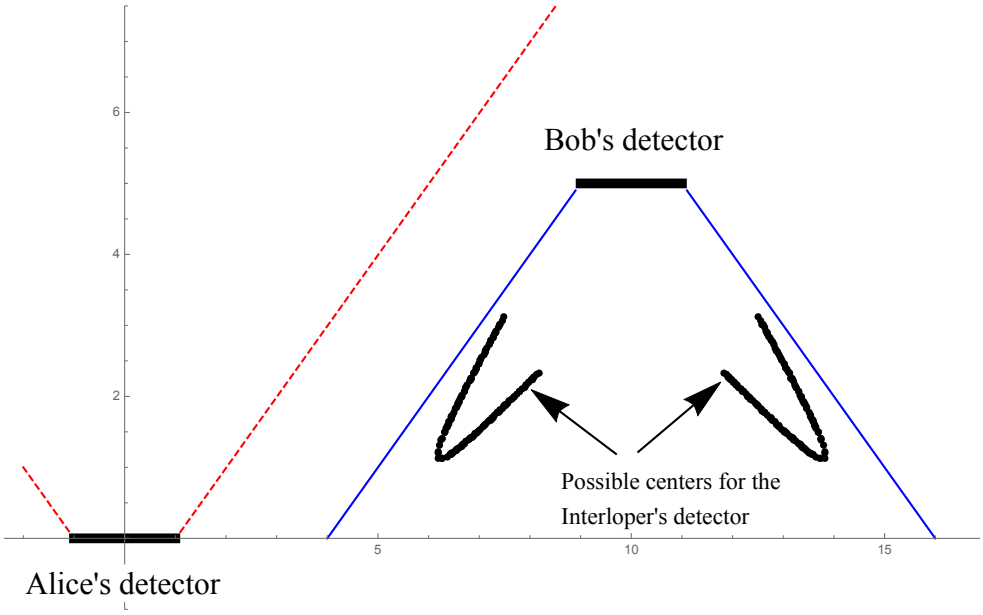

Figure 3.3: Plot of a possible scenario between Alice, Bob and the Interloper's detectors plotting the x-coordinate of the detectors versus time.
Alice's detector switches on at $t_{\text{A}} = 0$ and is centered at $\boldsymbol{x}_{\text{A}} = (0, 0, 0)$. Bob's detector switches on at $t_{\text{B}} = 5$ and is centered at $\boldsymbol{x}_{\text{A}} = (10, 0, 0)$. Two curves represent some positions for the Interloper's detector center for which $\xi_{\text{IB}} = \pi/2$, with ξ_{IB} definded in 3.34. For those positions, the Interloper would cancel correlation harvesting between Alice and Bob.

Now that we have some insight both visually and mathematically, we can understand better how the correlation cancellation works if the Interloper's detector is inside Bob's past cone. It seems that it is partially due to the Interloper's detector signalling Bob's detector, since the Interloper and Bob are necessarily in light-contact. This "evil" placing of Interloper detector sends a signal and modifies the field in such a way that detector B becomes maximally entangled with the field when it interacts with it.

At the beginning of this chapter, we stated that in the absence of the Interloper detector, Alice and Bob could harvest correlations. In the next section, we are going to analyze

different classical and quantum correlations harvested between Alice and Bob.

3.4 Harvesting correlations

In this section, we will study the classical and quantum correlations harvested between two identical target detectors, that is Alice's (A), Bob's (B) and with the presence of N *interloper* detectors (not just the Interloper). Recall that these *interloper* detectors interact with the field at some time before Bob and after Alice, i.e. $t_{\text{A}} < t_i < t_{\text{B}}$ for $i = 1, \ldots, N$. The density matrix for the target detectors is obtained from Eq. (3.20) after tracing out the interloper detectors. In particular, we study three kinds of correlation quantifiers for the final state of the detectors in Eq. (3.21). Namely, we will analyze:

1. the correlators of any two arbitrary observables of the detectors,
2. the mutual information of the target detectors, and
3. the quantum discord of the target detectors.

In the following subsections, we introduce the different correlation measures and provide analytical formulas for our scenario using the density matrix in Eq. (3.21). However, we will not analyze each of the formulas in depth. In Section 3.5, we will see that they have similar behaviour for various ranges of parameters; we will discuss and compare these correlations measures then.

3.4.1 Correlators of the detectors observables

Let $\hat{\mathcal{O}}_{\text{A}}$ and $\hat{\mathcal{O}}_{\text{B}}$ be any two observables defined on the Hilbert spaces of detectors A and B respectively. The correlation function between $\hat{\mathcal{O}}_{\text{A}}$ and $\hat{\mathcal{O}}_{\text{B}}$ in the joint state $\hat{\rho}_{\text{AB}}$ is defined as

$$\Gamma_{\hat{\rho}_{\text{AB}}}(\hat{\mathcal{O}}_{\text{A}}, \hat{\mathcal{O}}_{\text{B}}) \coloneqq \langle \hat{\mathcal{O}}_{\text{A}} \hat{\mathcal{O}}_{\text{B}} \rangle - \langle \hat{\mathcal{O}}_{\text{A}} \rangle \langle \hat{\mathcal{O}}_{\text{B}} \rangle, \tag{3.36}$$

where $\langle \hat{\mathcal{O}} \rangle \coloneqq \text{Tr}(\hat{\rho}_{\text{AB}} \hat{\mathcal{O}})$ denotes the expectation value of $\hat{\mathcal{O}}$ on the detectors' state $\hat{\rho}_{\text{AB}}$ given in Eq. (3.21). We define a convenient basis of detector operators for the $\nu-$th detector as

$$\hat{S}_0^\nu \coloneqq |-1_\nu\rangle\langle -1_\nu| + |1_\nu\rangle\langle 1_\nu| = \mathbb{1}_\nu, \qquad \hat{S}_1^\nu \coloneqq |-1_\nu\rangle\langle 1_\nu| + |1_\nu\rangle\langle -1_\nu|, \tag{3.37}$$

$$\hat{S}_2^\nu \coloneqq \text{i}\,|-1_\nu\rangle\langle 1_\nu| - \text{i}\,|1_\nu\rangle\langle -1_\nu|, \qquad \hat{S}_3^\nu \coloneqq -|-1_\nu\rangle\langle -1_\nu| + |1_\nu\rangle\langle 1_\nu|. \tag{3.38}$$

where $|1_\nu\rangle$ and $|-1_\nu\rangle$ are the elements of the basis of each detector's Hilbert space defined in Eq. (3.11). We can then denote any Hermitian operator in the Hilbert spaces of detectors a and b as

$$\hat{\mathcal{O}}_{\mathrm{A}} = a_0\hat{S}_0^{\mathrm{A}} + a_1\hat{S}_1^{\mathrm{A}} + a_2\hat{S}_2^{\mathrm{A}} + a_3\hat{S}_3^{\mathrm{A}}, \tag{3.39}$$

$$\hat{\mathcal{O}}_{\mathrm{B}} = b_0\hat{S}_0^{\mathrm{B}} + b_1\hat{S}_1^{\mathrm{B}} + b_2\hat{S}_2^{\mathrm{B}} + b_3\hat{S}_3^{\mathrm{B}}, \tag{3.40}$$

where $a_i, b_i \in \mathbb{R}$. We recall that the correlation between $\hat{S}_0^\nu = \mathbb{1}_\nu$ and any operator is zero; thus, we obtain

$$\Gamma_{\hat{\rho}_{\mathrm{AB}}}(\hat{\mathcal{O}}_{\mathrm{A}}, \hat{\mathcal{O}}_{\mathrm{B}}) = \sum_{m,n=1}^{3} a_m b_n \Gamma_{\hat{\rho}_{\mathrm{AB}}}(\hat{S}_m^{\mathrm{B}}, \hat{S}_n^{\mathrm{A}}). \tag{3.41}$$

It is then straightforward to calculate each $\Gamma_{\hat{\rho}_{ab}}(\hat{S}_m^{\mathrm{B}}, \hat{S}_n^{\mathrm{A}})$ using (3.21) and (3.36)—which we do explicitly in Appendix A.3—resulting in

$$\begin{aligned}\Gamma_{\hat{\rho}_{\mathrm{AB}}}(\hat{\mathcal{O}}_{\mathrm{A}}, \hat{\mathcal{O}}_{\mathrm{B}}) =& \frac{\Omega_{\mathrm{A}}\Omega_{\mathrm{B}}}{4}\Big(\prod_j \cos\xi_{j\mathrm{B}}\Big)e^{-\zeta}\big[\,\sinh\zeta_{\mathrm{AB}}(a_1\sin\xi_{0\mathrm{B}} + a_2\cos\xi_{0\mathrm{B}})(b_1\sin\xi_{0\mathrm{A}} + b_2\cos\xi_{0\mathrm{A}}) \\ &+ (\cosh\zeta_{\mathrm{AB}} - \cos\xi_{\mathrm{AB}})(a_1\cos\xi_{0\mathrm{B}} - a_2\sin\xi_{0\mathrm{B}})(b_1\cos\xi_{0\mathrm{A}} - b_2\sin\xi_{0\mathrm{A}}) \\ &- e^{\zeta/2}\sin\xi_{\mathrm{AB}}\,(a_1\sin\xi_{0\mathrm{B}} + a_2\cos\xi_{0\mathrm{B}})\,b_3\big].\end{aligned} \tag{3.42}$$

In this expression, the detectors are considered to be identical and coupling with equal strength, so we defined

$$\zeta \coloneqq \zeta_{\mathrm{AA}} = \zeta_{\mathrm{BB}} = 4\int \mathrm{d}^n\boldsymbol{k}|\beta_{\mathrm{A}}(\boldsymbol{k})|^2 = 4\int \mathrm{d}^n\boldsymbol{k}|\beta_{\mathrm{B}}(\boldsymbol{k})|^2. \tag{3.43}$$

As shown in Appendix A.5, ζ depends on Alice's and Bob's detectors coupling strengths, but it does not depend on the spacetime position of Alice's, Bob's and the interloper's detectors.

From Eq. (3.42) we can extract how correlators depend on the parameters of the setup. The product $\prod_j \cos\xi_{j\mathrm{B}}$ depends solely on the characteristics of the interloper detectors and their relative position to Bob's detector. The rest of the expression depends on the target detectors and the initial field state.

3.4.2 Mutual information

Mutual information is a measure of total correlations (classical and quantum) that can be thought of as the amount of information that the two parties in a bipartite system share between each other [97]. It is defined as

$$\mathcal{I}(\hat{\rho}_{\mathrm{AB}}) \coloneqq S(\hat{\rho}_{\mathrm{A}}) + S(\hat{\rho}_{\mathrm{B}}) - S(\hat{\rho}_{\mathrm{AB}}), \tag{3.44}$$

where $\hat{\rho}_{\mathrm{A}}$ and $\hat{\rho}_{\mathrm{B}}$ are the reduced states for the first and last detector, respectively and $S(\hat{\rho})$ is the von-Neumann entropy of state $\hat{\rho}$.

Although the mutual information can be computed in closed form for any choice of initial coherent state of the field, for convenience of the analysis, we will focus on the case when the field is initially in the vacuum state. In this scenario the density matrix $\hat{\rho}_{\mathrm{AB}}$ becomes a X-state, as derived in Appendix A.4.

As shown in the Appendix A.4, we obtain

$$\begin{aligned}
S(\hat{\rho}_{\mathrm{B}}) &= g\Big(e^{-\zeta/2}\cos\xi_{\mathrm{AB}}\prod_j \cos\xi_{j\mathrm{B}}\Big), \\
S(\rho_{\mathrm{A}}) &= g(e^{-\zeta/2}), \\
S(\hat{\rho}_{\mathrm{AB}}) &= -a_1\log_2 a_1 - b_1\log_2 b_1 + a_1 g\Big(\frac{a_2}{a_1}\Big) + b_1 g\Big(\frac{b_2}{b_1}\Big),
\end{aligned} \tag{3.45}$$

where,

$$\begin{aligned}
g(x) &= -\frac{1-x}{2}\log_2\Big(\frac{1-x}{2}\Big) - \frac{1+x}{2}\log_2\Big(\frac{1+x}{2}\Big), \\
a_1 &= \frac{1}{2}(1 + e^{-\zeta}\cosh\zeta_{\mathrm{AB}}\prod_j \cos\xi_{j\mathrm{B}}), \\
b_1 &= \frac{1}{2}(1 - e^{-\zeta}\cosh\zeta_{\mathrm{AB}}\prod_j \cos\xi_{j\mathrm{B}}), \\
a_2^2 &= \frac{1}{4}e^{-\zeta}\Big[1 + 2\cos\xi_{\mathrm{AB}}\prod_j \cos\xi_{j\mathrm{B}} + \Big(\prod_j \cos\xi_{j\mathrm{B}}\Big)^2\Big(1 + e^{-\zeta}\sinh^2\zeta_{\mathrm{AB}}\Big)\Big], \\
b_2^2 &= \frac{1}{4}e^{-\zeta}\Big[1 - 2\cos\xi_{\mathrm{AB}}\prod_j \cos\xi_{j\mathrm{B}} + \Big(\prod_j \cos\xi_{j\mathrm{B}}\Big)^2\Big(1 + e^{-\zeta}\sinh^2\zeta_{\mathrm{AB}}\Big)\Big].
\end{aligned} \tag{3.46}$$

From (3.45) we can evaluate the mutual information $\mathcal{I}(\hat{\rho}_{\mathrm{AB}})$ using (3.44).

3.4.3 Quantum Discord

Mutual information does not distinguish classical correlations from quantum ones. Even in the absence of entanglement it has been argued that there can be other kind of correlations that may have some notion of 'non-classicality' such as quantum discord [3]. Before defining quantum discord, it is worth introducing a new measure of correlations $\mathcal{C}$ (called in [56] *classical correlations*) was defined as follows:

$$\mathcal{C}(\hat{\rho}_{\text{AB}}) = S(\hat{\rho}_{\text{B}}) - \inf_{\{\hat{M}_k\}} S(\hat{\rho}_{\text{AB}}|\{\hat{M}_k\}), \tag{3.47}$$

where the expression $S(\hat{\rho}_{\text{AB}}|\{\hat{M}_k\})$ denotes the average amount of uncertainty that we have about subsystem B after performing local positive-operator valued measures (POVM), $\hat{M}_i\hat{M}_i^\dagger$, on subsystem A:

$$S(\hat{\rho}_{\text{AB}}|\{M_k\}) = \sum_i p_i S(\hat{\rho}_{\text{B}}^i), \tag{3.48}$$

$$p_i = \text{Tr}\Big\{(\hat{M}_i \otimes \mathbb{1})\hat{\rho}_{\text{AB}}(\hat{M}_i^\dagger \otimes \mathbb{1})\Big\}, \tag{3.49}$$

$$\hat{\rho}_{\text{B}}^i = \frac{\text{Tr}_{\text{A}}\,(\hat{M}_i \otimes \mathbb{1})\hat{\rho}_{\text{AB}}(\hat{M}_i^\dagger \otimes \mathbb{1})}{p_i}. \tag{3.50}$$

Even if the optimization is over the set of POVMs on the subsystem A, some formulas have been found when optimizing solely over the set of PVMs [53, 47, 90]. For some cases of two-qubit states, optimizing over the set of PVMs yields the correct $\mathcal{C}$ correlation function [27]. As we will detail a bit further down the road, for our particular only need to optimize over the set PVMs. Thus, for our two qubit system, $\mathcal{C}(\hat{\rho}_{\text{AB}})$ can be thought of as the maximum information that can be gained about a subsystem B, by coherence-destroying projective measurements of the state of A. It can be seen that for a separable state for which the partial state of A is a classical probability distribution over the eigenstates of some observable (i.e., $\hat{\rho}_{\text{AB}} = \sum_i p_i \left|i\right\rangle\!\left\langle i\right| \otimes \hat{\rho}_{\text{B}}^i$) then $\mathcal{C}(\hat{\rho}_{\text{AB}}) = \mathcal{I}(\hat{\rho}_{\text{AB}})$ [3]. Thus, in the case where the system only has classical correlations, $\mathcal{C}(\hat{\rho}_{\text{AB}})$ is exactly the mutual information.

However, the name 'classical correlation' does not mean correlations *in absence of entanglement*. The presence of entanglement in a pure two-qubit system (which is a genuinely quantum form of correlations) will yield non-zero $\mathcal{C}$. Rather $\mathcal{C}$ accounts for the information that can be learned about B by the application of measurement protocols on A—usually associated with classical (macroscopic) apparatuses acting locally on A. Along this line, it can be checked that $\mathcal{C}$ satisfies the following reasonable properties described in [56]:

- $\mathcal{C} = 0$ for product states $\hat{\rho}_{\mathrm{AB}} = \hat{\rho}_{\mathrm{A}} \otimes \hat{\rho}_{\mathrm{B}}$.
- $\mathcal{C}$ is invariant under local unitary transformations.
- $\mathcal{C}$ is non-increasing under local operations.
- $\mathcal{C} = S(\hat{\rho}_{\mathrm{A}}) = S(\hat{\rho}_{\mathrm{B}})$ for pure states.

The only two differences between these reasonable properties for $\mathcal{C}$ and an entanglement measure is that a) we allow $\mathcal{C}$ to increase under local operations when there is classical communication and b) we allow $\mathcal{C}$ to be non-zero for non-product separable states. In this light one may wonder if 'classical correlation' might be a misnomer since, for pure bipartite states, $\mathcal{C}$ is precisely the entanglement entropy and entanglement is rarely referred to as a 'classical correlation'. Instead, the usefulness of $\mathcal{C}$ on its own is that it quantifies the information about B that is revealed when measuring A through POVMs, regardless whether it is a consequence of pre-existing classical correlations or entanglement [138]. Note as well that, outside pure states, $\mathcal{C}$ is not symmetric w.r.t subsystems A and B.

The Henderson-Vedral $\mathcal{C}$ function is often difficult to find analytically because of the optimization over the set of possible POVMs on A. However, for a pair of qubits, it has been proved that the optimality in the $\mathcal{C}$ function is always achieved optimizing over the set of PVMs [53]. Even though no general analytical expression for $\mathcal{C}$ exists for a pair of qubits in an arbitrary state, tight bounds have been found analytically for some class of states [9, 44].

One of such families of two-qubit states is the family of *X-states* (states for which density matrix elements in some relevant basis is of the form ρ_{ij}, obeying $\rho_{12} = \rho_{13} = \rho_{21} = \rho_{24} = \rho_{31} = \rho_{34} = \rho_{42} = \rho_{43} = 0$). In Appendix A.4 we show that the density matrix of A and B (3.21) is indeed a X-state in the $\{|g\rangle, |e\rangle e^{\mathrm{i}t\Omega}\}$ basis, when the field is initially in the vacuum state.

For X-states, the authors in [9] proposed an algorithm to evaluate analytically the $\mathcal{C}$ function, by optimizing over the set of orthogonal measurements (also called von Neumann measurements) instead of over the set of PVMs. This optimization is not enough, in general, to obtain the optimal value of the $\mathcal{C}$-function for X-states of rank higher than two [53, 76]. Therefore, this algorithm only provides a tight bound for the $\mathcal{C}$-function in general.

However, for our density matrices (Eq. (3.21)) we can still use the formulae obtained in [9] to calculate exactly the $\mathcal{C}$ function, even though they are rank four. It was shown in [27] that the algorithm proposed in [9] gives the correct results for a certain subfamily of

X-states, which satisfy any one of the following conditions:

$$4(|\rho_{23}|^2) \leq (\rho_{11} - \rho_{22})(\rho_{44} - \rho_{33}), \tag{3.51}$$

$$|\sqrt{\rho_{11}\rho_{44}} - \sqrt{\rho_{22}\rho_{33}}| \leq 2|\rho_{23}|. \tag{3.52}$$

In Appendix A.4.3 we show how first condition is always false and the second condition is always met for the parameters we consider in this manuscript. Hence using the formulas provided by Ali et al. in [9] is justified in our case.

To calculate the classical correlation for a X-state as described in [9], one has to do an optimization over eight different possibilities. In our case, they are reduced to the the following formula as derived in Appendix A.4.2:

$$\mathcal{C}(\hat{\rho}_{\text{AB}}) = S(\hat{\rho}_{\text{B}}) - \min\{p_0 g(\theta_0) + p_1 g(\theta_1), g(\theta')\}, \tag{3.53}$$

$$p_0 = \frac{1 + e^{-\zeta/2}}{2} \qquad p_1 = \frac{1 - e^{-\zeta/2}}{2}, \tag{3.54}$$

$$\theta_0 = e^{-\zeta/2} \frac{\cos\xi_{\text{AB}} + e^{-\zeta/2}\cosh\zeta_{\text{AB}}}{2p_0} \prod_j \cos\xi_{j\text{B}}, \tag{3.55}$$

$$\theta_1 = e^{-\zeta/2} \frac{\cos\xi_{\text{AB}} - e^{-\zeta/2}\cosh\zeta_{\text{AB}}}{2p_1} \prod_j \cos\xi_{j\text{B}}, \tag{3.56}$$

$$\theta' = e^{-\zeta/2} \sqrt{1 + e^{-\zeta}\sinh^2\zeta_{\text{AB}}} \prod_j \cos\xi_{j\text{B}}. \tag{3.57}$$

Finally, quantum discord, $\mathcal{Q}$, is a measure of quantum correlations for bipartite systems, useful in characterizing quantum correlations beyond entanglement. It is defined as the difference between quantum mutual information, $\mathcal{I}(\hat{\rho})$, and the Henderson-Vedral correlation function $\mathcal{C}(\hat{\rho})$,

$$\mathcal{Q}(\hat{\rho}) = \mathcal{I}(\hat{\rho}) - \mathcal{C}(\hat{\rho}). \tag{3.58}$$

The motivation for defining discord as such comes from the fact that in classical information theory, the mutual information between two random variables can be obtained 1) with an expression like (3.44) where the entropies are the respective Shannon entropies, and 2) as an optimization problem over all possible measurements of one of the variables. The quantum analogue to the two classically identical expressions can differ for some states. Discord is defined as this difference [98].

3.5 Trends in correlation

In this section, we analyze and compare these correlation measures. The four correlation measures considered (observable correlators, mutual information, $\mathcal{C}$ correlation function and quantum discord) follow similar trends in their dependence on the parameters of the setup.

In this subsection, we explore the dependence of the different correlation measures on

1. The relative positioning of Alice and Bob
2. The coupling strength of both target detectors
3. The impact of the presence of an additional (interloper) detector in the harvesting of bipartite correlations

In all cases we consider that both Alice and Bob are identical detectors and that their smearing function is the hard-sphere defined in Eq. (3.34), with radious σ. In the last two scenarios, we will consider the following spacetimes positions for Alice and Bob shown in Fig. 3.5, which showcases space-like separation, light-like separation and time-like separation. In the three cases, the difference of switching time is $T = t_{\text{B}} - t_{\text{A}} = 5$. In the first scenario, the difference between in position is $|\boldsymbol{X}| = |\boldsymbol{x}_{\text{A}} - \boldsymbol{x}_{\text{B}}| = 0$ and thus Alice and Bob are timelike separated. In the second scenario, the difference between in position is $|\boldsymbol{X}| = |\boldsymbol{x}_{\text{A}} - \boldsymbol{x}_{\text{B}}| = 5\sigma$ and thus Alice and Bob are lightlike separated. In the first scenario, the difference between in position is $|\boldsymbol{X}| = |\boldsymbol{x}_{\text{A}} - \boldsymbol{x}_{\text{B}}| = 10\sigma$ and thus Alice and Bob are spacelike separated.

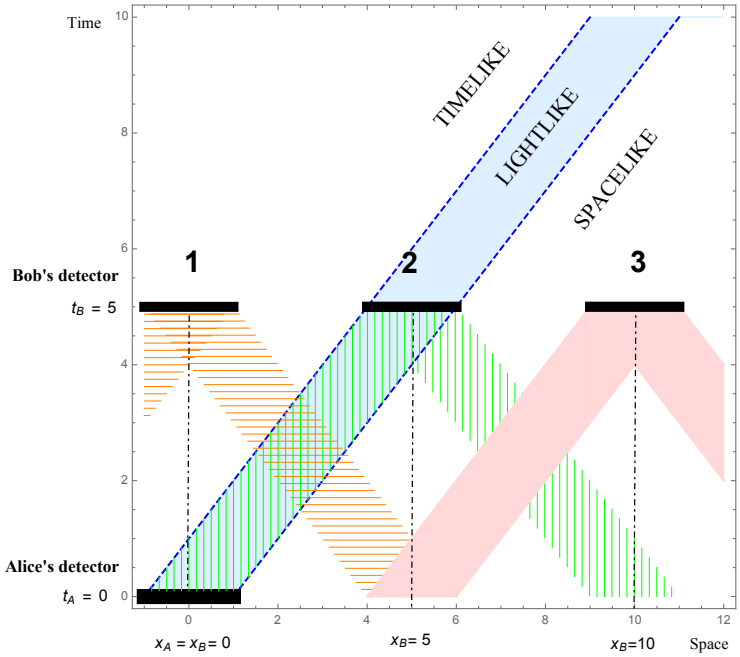

Figure 3.4: Representation for 1+1 dimensions of three possible scenarios for Alice and Bob's detectors.

3.5.1 Spacetime dependence of correlations

In the scenario where we have two detectors coupling to the field, there are two main ways in which they can get correlated. First, if the detectors are light-connected, they can talk to each other by the exchange of "real-quanta". More precisely, the first detector creates energy-carrying perturbations that propagate at the speed of light and reach the second detector, correlating the two of them.

On the other hand, if the detectors are spacelike separated, they cannot exchange signals, but they can harvest the correlations that pre-exist in the vacuum state of the field [104]. This is also the case for pure timelike separation since, in 3+1D Minkowski space, the energy carried by a massless field cannot propagate slower than light either due to the strong Huygens principle [64].

Figs. 3.5 show how the extracted correlations decay as the spacetime separation between the detectors increases. Whereas most of the correlation harvesting happens on null-

contact, we see how detectors can also harvest correlations while spacelike (or timelike) separated. This is not surprising since local field observables in spacelike separation are, in general, also correlated [127, 128, 110], albeit with smaller intensity as the spatial and temporal distance between them increases.

Propagators become smaller as the spacelike distance between detectors increases for fixed time slices. Thus, the term $T_{j\mathrm{B}}$, given in (3.19), becomes smaller as the two detectors, A and B, are more and more spacelike separated. It is then easy to check with our formulas that vanishing $T_{j\mathrm{B}}$ implies that every correlation measure we have studied also vanishes. This makes sense as the correlations we are trying to extract from the field become increasingly small.

In Fig. 3.5 we show the dependence of the different measures of correlation for depending on their position with respect to each other, when there is hard-sphere smearing. We observe that correlations are stronger when the two detectors are time-like separated. Mathematically that is the zone such that $||\boldsymbol{x}_{\mathrm{B}} - \boldsymbol{x}_{\mathrm{A}}| - |t_{\mathrm{B}} - t_{\mathrm{A}}|| = ||\boldsymbol{X}| - |T|| \leq 2\sigma$.

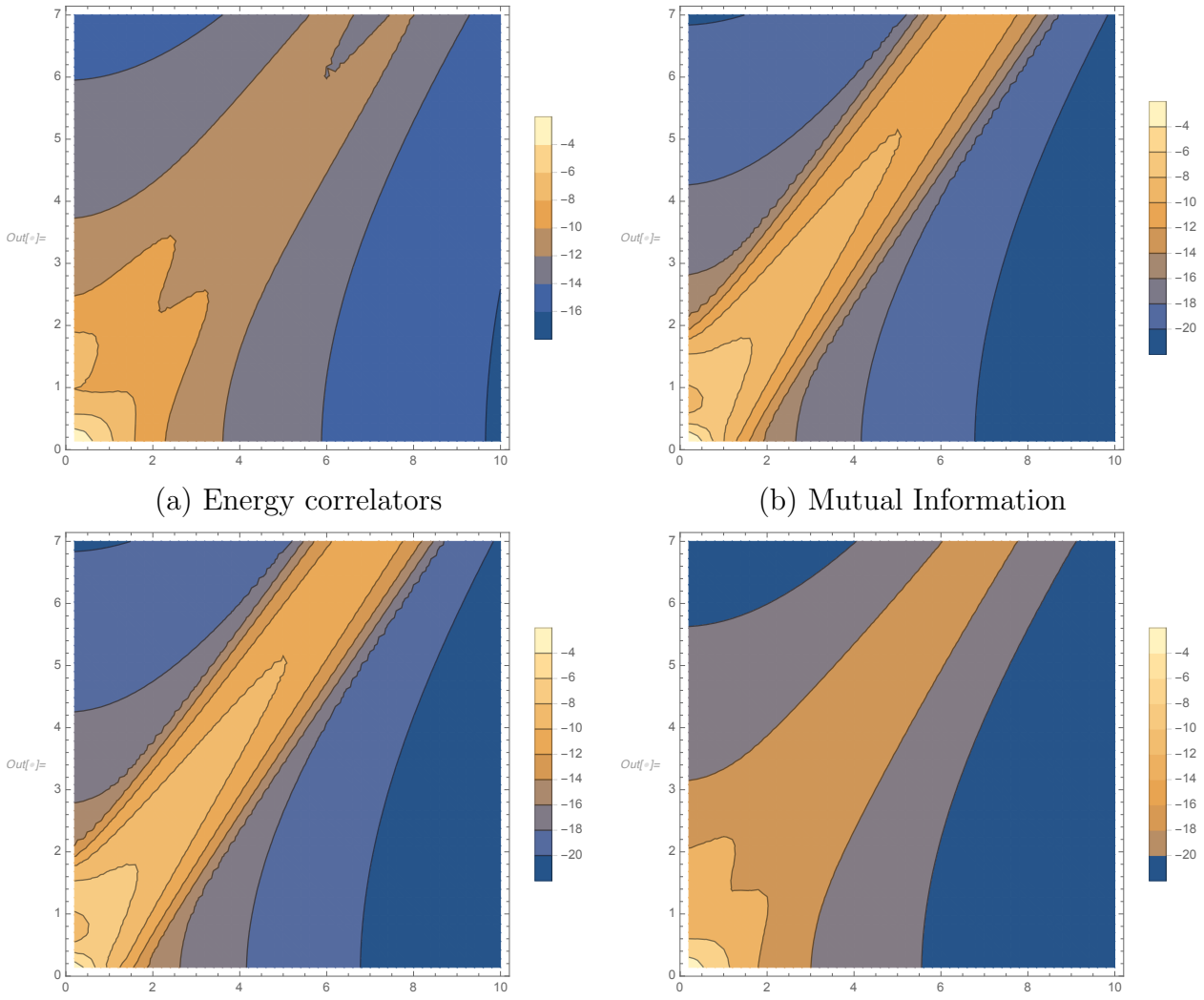

(a) Energy correlators

(b) Mutual Information

(c) Classical Correlations

(d) Quantum Discord

Figure 3.5: Logarithmic dependence on relative position of target detectors of different correlation measures.
Coupling strength is set to $\tilde{\lambda}^2 = 1$. The smearing function has been chosen to be 3-dimensional hard-sphere with radius equal to $\sigma = 1$, as given in (3.33). We consider a scenario in which there are no other detectors present, i.e., $\xi_{\text{IB}} = 0$. We consider that the initial state of the field is the vacuum state. Plotted from $X = 0$ to $X = 10\sigma$.

3.5.2 Coupling strength

The strength of the couplings of detector A and B is quantified by the parameter $\tilde{\lambda}$ (we are assuming the target detectors to be identical; i.e. $\tilde{\lambda}_{\text{A}} = \tilde{\lambda}_{\text{B}} = \tilde{\lambda}$ and hence the product of coupling strengths of detectors A and B, is $\tilde{\lambda}^2$). In Fig. (3.6) we plot the dependence on $\tilde{\lambda}^2$ of (a) the free energy $\hat{H}_{\nu}^{\text{free}}$ correlators, (b) mutual information, (c) Henderson-Vedral classical correlation and (d) quantum discord.

We see how all the correlations vanish at $\tilde{\lambda}^2 = 0$ and for a small increase in the $\tilde{\lambda}^2$ the magnitude of correlations increases. This is natural as zero coupling implies that the (initially uncorrelated) detectors do not interact with the field at all and hence they cannot correlate with each other. As we increase the coupling, the detectors start interacting with the field, and the correlations slowly increase in magnitude.

Moreover, in the limit of very strong coupling, $\tilde{\lambda}^2 \to \infty$ all correlations vanish. Applying the Cauchy-Schwarz inequality to (3.19) we obtain $|\zeta_{\text{BA}}|, |\xi_{\text{AB}}| \leq \zeta$. Since by definition, $\zeta \propto \tilde{\lambda}^2$ and $\zeta \geq 0$, we see that the terms $e^{-\zeta}, e^{-\zeta+\zeta_{\text{AB}}}$ and $e^{-\zeta-\zeta_{\text{AB}}}$ all approach zero as $\tilde{\lambda}^2$ tends to infinity. Thus using Eqs. (3.42), (3.45), (3.44), (3.53) and (3.58) we conclude that all correlation measures must go to zero in the strong coupling limit. Physically what this means is a detector interacts with the field so strongly, i.e. "kicks" or displaces the field so much that the second detector is unable to harvest correlations. This particular phenomenon was studied in the case of non-perturbative entanglement harvesting [118]. In the strong coupling regime (outside perturbation theory), increasing the coupling strength provokes a fast decay of correlation harvesting at least for the case of delta-couplings. Since the harvesting of correlations is usually a competition between non-local terms and local noise [110], it is possible that this phenomenon is due to the amplification of the local noise as the intensity of the interaction increases [119]. The strong delta couplings entangle every single detector with the field locally introducing local noise that plays against the acquisition of correlations between the two detectors.

Finally, we would like to note that, as the correlations are continuous at all points, vanish at $\tilde{\lambda}^2 = 0$ and asymptote horizontally to the line $y = 0$, the existence of a maximum is implied, as shown in Fig. (3.6). Therefore given any arrangement of target detectors and interlopers, and any correlation measure, we can always find a coupling strength that maximizes its value.

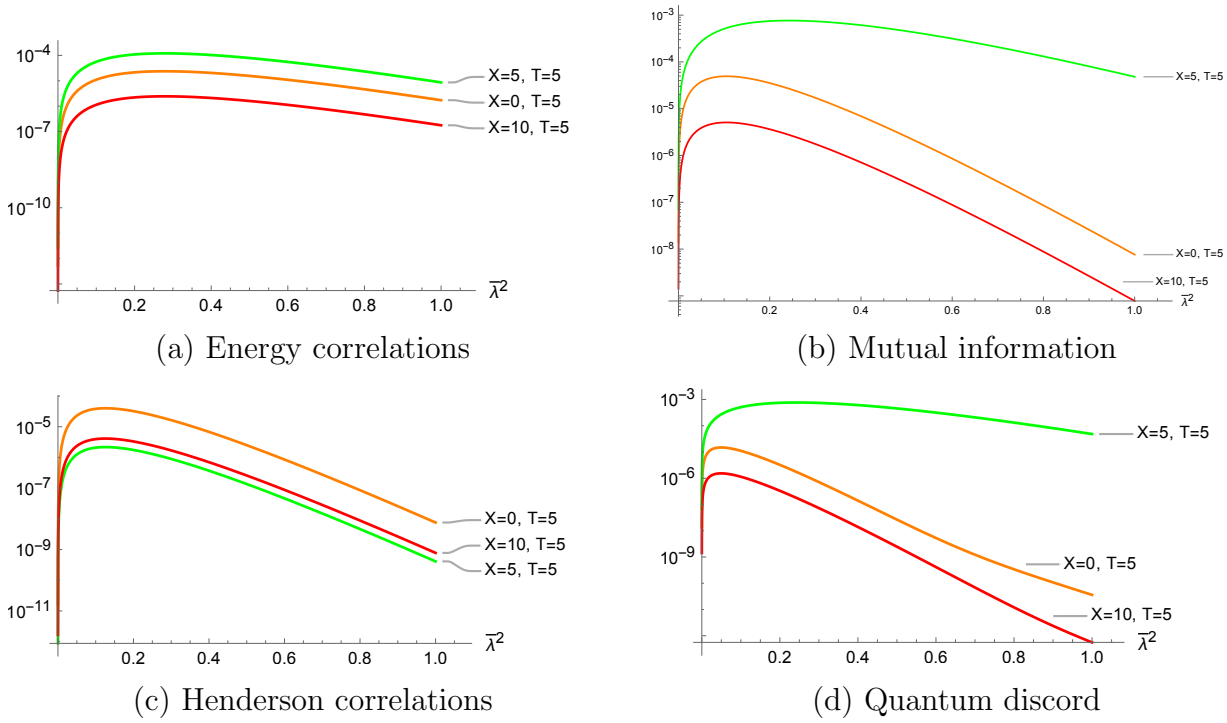

(a) Energy correlations

(b) Mutual information

(c) Henderson correlations

(d) Quantum discord

Figure 3.6: Logarithmic dependence of coupling strength for correlation measures between detector A and B in the absence of other detectors.
The smearing function has been chosen to be 3-dimensional hard-sphere with a radius equal to $\sigma = 1$, as given in (3.33). We consider the energy gap of the detectors, $\Omega_{\mathrm{A}} = \Omega_{\mathrm{B}} = 1$ The initial state of the field is the vacuum. We observe that all correlation measures vanish at $\gamma = 0$ and have horizontal asymptotes going to 0. As expected, there is at least one maximum for each correlation measure and each set of fixed parameters.

3.5.3 Influence of the extra detectors

Finally, we discuss the influence of the interloper detectors. They attenuate the correlation harvested, in general due to the $\cos \xi_{j\mathrm{B}}$ term contributed by each interloper j as can easily be checked in the expressions of the correlation measures- Eqs. (3.42), (3.45), (3.44), (3.53) and (3.58). Moreover, notice that the argument of the cosine depends on $\xi_{j\mathrm{B}}$, which is a function of the relative arrangement of the extra detector and Bob's detector (the last detector).

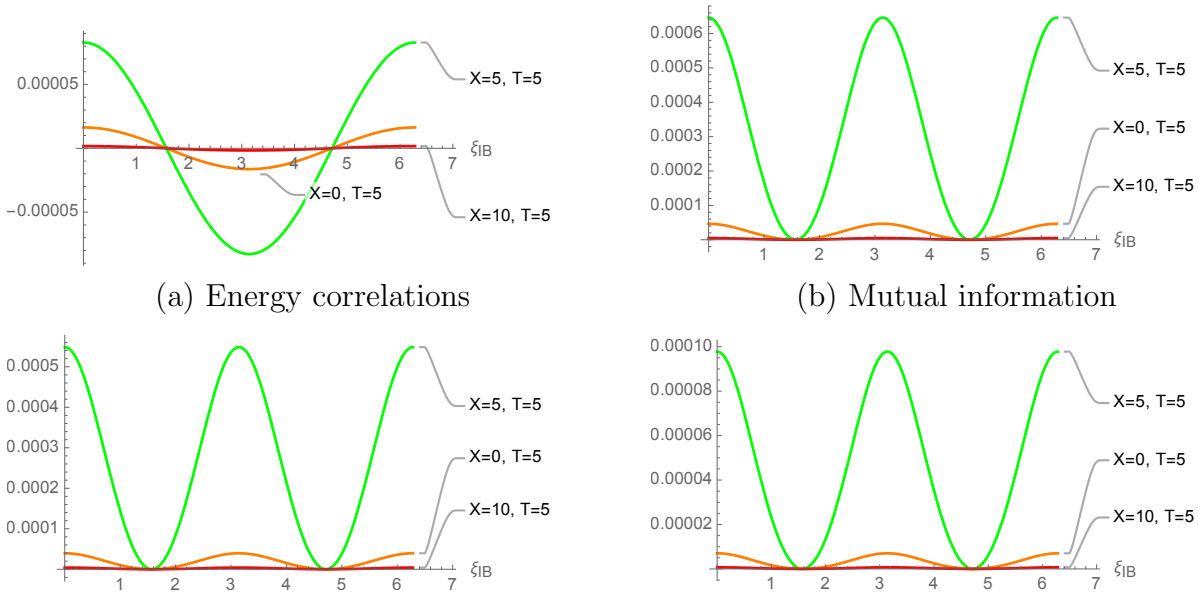

(a) Energy correlations

(b) Mutual information

(c) Henderson correlations

(d) Quantum discord

Figure 3.7: Dependence of the different correlation measures with respect to ξ_{IB}. We consider a scenario in which there is a single interloper detector, I, and we analyze the dependence of the different correlation measures with respect to ξ_{IB} (for the rest of the detectors, $\xi_{\text{JB}} = 0$). The term ξ_{IB} depends on the coupling strength of the middle detector and the relative position between detector I and the last detector, B. Coupling strength is set to $\bar{\lambda}^2 = 0.2$. The smearing function has been chosen to be a 3-dimensional hard-sphere with a radius equal to $\sigma = 1$, as given in (3.33). We consider the initial state of the field to be the vacuum state.

We notice that, if we place enough detectors such that $|\cos \xi_{j\text{B}}| < 1$, the limit of 0 correlations will be achieved. This attenuation of the correlation by extra detectors is expected, as they introduce more noise in the field in between the time the field interacts with our target detectors.

As we already discussed in Section 3.3, our most striking result was that when a single interloper I is placed at a spacetime position $(\mathbf{x}_{\text{I}}, t_{\text{M}})$, such that ξ_{IB} is an odd multiple of $\pi/2$, all the correlations measures vanish simultaneously as $\cos \xi_{\text{IB}} = 0$. In figure 3.7 we plot how the different measures depend on one ξ_{IB} when there is only one interloper detector I along with the target detectors.

3.6 Conclusion

In this chapter, we considered N two-level detectors interacting with a coherent state of a free scalar massless field via a delta-Dirac coupling. We non-perturbatively obtained the density matrix of the whole system. We particularized our formula and obtained the joint state for two detectors, Alice and Bob, the first and last to couple to the field, in the presence of N *interloper* detectors that coupled to the field at some intermediate times. We discussed that in this setting, Alice and Bob could generally harvest classical and quantum correlations, even if entanglement correlation was not possible.

The main result in this chapter is that the presence of a single interloper placed conveniently in spacetime and with a particular coupling strength can cancel the harvesting of correlations between Alice and Bob. The Interloper accomplishes that by modifying the field in such a way that it "floods" Bob's detector with entropy. In other words, the presence of the interloper makes Bob maximally entangled with the field. In fact, the parameters of the interloper solely depend on Bob's detector's parameters and not at all on Alice's detector. We particularized this result to 3+1 dimensions and discussed an example in which the detectors have compact smearing functions. We concluded that an interloper needs to always be placed lightlike separated from Bob to be successful at sabotaging the correlation harvesting protocol. Thus, the correlation harvesting cancellation is partially due to some communication between the Interloper and Bob.

After presenting this first result, we studied several classical and quantum correlation measures: namely, the correlators between any pair of observables for Alice's and Bob's detectors, their mutual information and their quantum discord. We included analytical formulas for each of the correlation measures. We studied the dependence of the correlation measures on the coupling strengths of Alice and Bob. We obtained that there existed some coupling strengths for which the different correlation measures maximized. For the limit of strong coupling, it could be obtained analytically that the correlation measures vanished. Our interpretation was that too much noise was introduced, which was detrimental to the correlation harvesting protocol. In this same line, we studied that the presence of enough interloper detectors exponentially deteriorated the harvesting of correlation, and we could obtain this result from the density matrix of Alice and Bob generally.

The implications and outlook of this project will be described in Chapter 5.

Chapter 4

Machine learning quantum fields with detector probes

The results in this chapter are based in the preprint [51], a project result of the collaboration with Daniel Grimmer and Eduardo Martín-Martínez. Sections 4.4, 4.6 and 4.9 are verbatim. The paragraphs setting the paramaters in subsections 4.7.2 and 4.8.2 are verbatim. In 4.7.3, the paragraphs from Eq. (4.34) to Eq. (4.37) are verbatim.

4.1 Introduction

In Chapter 3, we explored how, using local Unruh-DeWitt detectors, one can learn about correlations and entanglement of quantum field states. In both cases, we used quite problem-dependent choices for detectors' geometry and coupling scenarios. These convenient choices allowed us to obtain analytical expressions for the detectors states, which in turn provided us with some information about the field. However, many scenarios may be too difficult to analyze mathematically or for which we do not even have theoretical models.

In such cases, a sensible way to obtain information about a quantum field is to analyze the outcomes of measurements of local probes coupled to the field. It is thinkable that one could learn about local features of the field using local probes. However, this task seems more challenging if we are interested in global features of the field, like its geometry or underlying entanglement structure. Fortunately, this is still theoretically feasible [96, 95]. Indeed, ground and thermal states of quantum fields store global information of the field in a localized, although scrambled, manner [100, 86, 78, 147, 70, 145]. For example, a ground

state will have information about its boundary conditions even in localized places far away from its boundaries [5].

Thus, in principle, there exists a map from measurement outcomes of local probes to claims about local and non-local features of the field. However, this map will be very convoluted: the information extracted from the field by the local probes is very scrambled. In some specific situations, one can translate the transition probabilities of the detector to the features of the field we want to study [129, 58, 5, 122, 96, 4]. However, in more challenging scenarios, one may not know what family of probabilities distributions are adequate for the problem in hand. We then have to find a context-free fit for the raw data coming from the probe(s) to claims about the field.

Fortunately, this is a well-studied problem in machine learning and deep learning. These techniques are used to provide insight from large and convoluted data sets by fitting a very general form of functions. They have been applied to multiple quantum settings in [57, 49, 26, 107, 131, 130, 148, 115, 93].

In this chapter, we use machine learning techniques to study how

1. a particle detector distinguishes boundary conditions before signals can bounce off of the boundaries and reach the probe,

2. detectors can determine the temperature of the quantum field before thermalization time, and

3. to distinguish a Fock State and a phase-averaged coherent state.

We obtain all these results by analyzing the outcomes of a single local probe coupled to the field with the same type of neural network. The first two results are accomplished using the same measurement protocol, and the third one is slightly modified to be able to generate the data more easily.

These results work as a proof-of-principle and show that neural networks are useful context-free tools in the study of non-local properties of the field using only local probes. This work introduces an operational way to study Quantum Field Theories without the burden of designing a clever measurement procedure (i.e. with lots of probes or complicated couplings). We prescribe a simple measurement protocol on the field, not tailored to extract information about one particular feature. The "difficult" part of the job is then done by the neural networks, which unravel the outcomes of the probe(s) and can recover information about *any* feature of the field.

4.2 Setup

We consider a 1+1 dimensional scalar quantum field with mass m and a harmonic oscillator probe coupled locally to the field. This harmonic oscillator probe has an excitation energy of $\hbar\omega_{\text{D}}$. The free Hamiltonian of this field-probe system is $\hat{\mathcal{H}}_{\text{FREE}} = \hat{\mathcal{H}}_\phi + \hat{\mathcal{H}}_{\text{D}}$ with

$$\hat{\mathcal{H}}_\phi = \frac{1}{2}\int_{-\infty}^{\infty} \mathrm{d}x\ c^2\hat{\pi}(\mathsf{x})^2 + (\partial_x\hat{\phi}(\mathsf{x}))^2 + \frac{m^2c^2}{\hbar^2}\hat{\phi}(\mathsf{x})^2, \tag{4.1}$$

$$\hat{\mathcal{H}}_{\text{D}} = \frac{\hbar\omega_{\text{D}}}{2}(\hat{q}_{\text{D}}^2 + \hat{p}_{\text{D}}^2), \tag{4.2}$$

where $\mathsf{x} = (t, x)$ and where $\hat{\phi}(\mathsf{x})$ and $\hat{\pi}(\mathsf{x})$ are the field observables satisfying the cannonical commutation relations $[\hat{\phi}(t,x), \hat{\pi}(t,y)] = \mathrm{i}\hbar\delta(x-y)$ and $\hat{q}_{\text{D}}$ and $\hat{p}_{\text{D}}$ are the probe observables satisfying $[\hat{q}_{\text{D}}, \hat{p}_{\text{D}}] = \mathrm{i}$. The probe couples to the field locally via an Unruh-DeWitt type of interaction, where the Hamiltonian (in the interaction picture) is given by

$$\hat{\mathcal{H}}_{\text{INT}} = \lambda\,\chi(t)\int_{-\infty}^{\infty}\mathrm{d}x\,F(x)\,\hat{q}_{\text{D}}\otimes\hat{\phi}(\mathsf{x}), \tag{4.3}$$

where λ is their coupling strength, $\chi(t)$ is a switching function and $F(x)$ is the probe's smearing function. The time evolution generated by (4.3) is implemented by its time-ordered exponential

$$\hat{U} = \mathcal{T}\exp\left[-\mathrm{i}\int_{-\infty}^{\infty}\mathrm{d}t\hat{H}_{\text{INT}}(t)\right], \tag{4.4}$$

so that if the initial state of the detector-field system is given by the density operator $\hat{\rho}_0$, the final state is given by

$$\hat{\rho} = \hat{U}\hat{\rho}_0\hat{U}^\dagger, \tag{4.5}$$

and the final state of the detectors after the interaction can be obtained by tracing over the field degrees of freedom $\hat{\rho}_{\text{D}} = \mathrm{tr}_{\hat{\phi}}[\hat{\rho}]$.

In the two cases we study the switching function is a top-hat function,

$$\chi(t) = \begin{cases} 1 & 0 \le t \le T \\ 0 & \text{else} \end{cases}, \tag{4.6}$$

where T denotes the duration of the coupling.

The smearing function will be given by a Gaussian function with width σ centered at x_{D}, the position of the detector's center of mass, i.e.,

$$F(x) = \frac{1}{\sigma\sqrt{2\pi}} \exp\left[-\frac{(x - x_{\text{D}})^2}{2\sigma^2}\right]. \tag{4.7}$$

In the next section, we consider two simplifications to this set up: we take an IR-cutoff and a probe-induced UV-cutoff. The IR-cutoff can be easily justified by considering we are studying a quantum field in a cavity. However, a naively chosen UV-cutoff can, in principle, cause superluminal signalling in our setting [87]. In Section 2.6, we explain how a probe induces a soft-UV cutoff in our setting, and thus this approximation is harmless in the right regime.

These two simplifications - the UV-cutoff and IR-cutoff - will allow us to study the evolution of the coupled system with the powerful Gaussian formalism.

4.3 Simplification and Gaussian formalism

Any smearing function with local support induces a natural UV cutoff for the field-probe system. As explained in Section 2.6, the coupling of the detector to the field modes is exponentially suppressed as the modes' frequencies increase. In particular, if a smearing function has length scale σ, then the probe will effectively not couple to modes with $|k| >> \sigma^{-1}$. Thus, we are justified in introducing a UV cutoff $K = 16/\sigma$ (i.e. we cut out the modes whose frequencies obey $|k| > K$), and this cutoff does not change our analysis nor the physical behaviour of the system. A detailed explanation of the effect of this particular cutoff and why it can be used is given in Section 2.7. Thus, the UV cutoff version of the interaction Hamiltonian yields

$$\hat{\mathcal{H}}^{\text{UV}}_{\text{INT}} = \lambda\, \chi(t) \sum_j a\, F(x_n)\, \hat{q}_{\text{D}} \otimes \hat{\phi}(t, x_j), \tag{4.8}$$

where $a \coloneqq \pi/K$ is the spacing of the discrete positions and the terms $x_j \coloneqq j\, a$ represent the points where the probe effectively couples to the field.

To simplify our calculations, we also modify the free field Hamiltonian given in Eq. (2.5). We choose to 1) introduce a hard UV-cutoff on the field Hamiltonian (i.e. we eliminate the modes with frequency $|k| \geq K$ everywhere, not just in the interaction Hamiltonian) and 2) introduce a first-neighbours approximation for $(\partial_x \hat{\phi}(\mathsf{x}))^2$. The physical implications of the second choice are a little bit more subtle, and they are discussed in detail in Section 2.7. There we conclude that a naively chosen cutoff may allow the existence of superluminal signals in higher frequencies. However, we analyze how the probe couples

in a feeble way to these frequencies and we quantify the amount of error introduced by this cutoff.

The resultant field Hamiltonian is as derived in Chapter 2 in Eq. (2.27):

$$\hat{\mathcal{H}}_{\phi}^{\text{UV}} = \frac{a}{2}\sum_{n} c^2\hat{\pi}^2(\mathsf{x}_n) + \left(\frac{\hat{\phi}(\mathsf{x}_{n+1}) - \hat{\phi}(\mathsf{x}_n)}{a}\right)^2 + \frac{m^2c^2}{\hbar^2}\hat{\phi}^2(\mathsf{x}_n). \tag{4.9}$$

We can further impose an IR-cutoff (i.e. we consider $|k| > M$ for some M). This is equivalent to restricting the field to a region $x \in [0, L]$ where $L = N\,a$ (i.e., field in a cavity). Since this cutoff does not induce a problem with super-luminal signal we have a degree of freedom in choosing L or, equivalently, N. Defining now dimensionless field operators $\hat{q}_n \coloneqq \sqrt{am/\hbar^2}\,\hat{\phi}(\mathsf{x}_n)$ and $\hat{p}_n \coloneqq \sqrt{a/m}\,\hat{\pi}(\mathsf{x}_n)$ (which satisfy $[\hat{q}_i, \hat{p}_j] = \mathrm{i}\delta_{ij}$) we obtain the following field and interaction Hamiltonians,

$$\hat{\mathcal{H}}_{\phi}^{\text{UV}} = \sum_{n=1}^{N} \frac{mc^2}{2}\left(\hat{p}_n^2 + \hat{q}_n^2\right) + \frac{\hbar^2}{2ma^2}(\hat{q}_{n+1} - \hat{q}_n)^2, \tag{4.10}$$

$$\hat{\mathcal{H}}_{\text{INT}}^{\text{UV}} = \lambda_0\,\chi(t)\sum_{n=1}^{N} a\,F(x_n)\,\hat{q}_{\text{D}} \otimes \hat{q}_n, \tag{4.11}$$

where $\lambda_0 = \lambda\,\hbar/\sqrt{a\,m}$ is the energy scale of the probe-field coupling. After these UV and IR cutoff, we obtain Hamiltonians that can be analyzed with the Gaussian formalism, explained in Section 2.8. We will use both the basis $\hat{\boldsymbol{R}} = (\hat{q}_{\text{D}}, \hat{p}_{\text{D}}, \hat{q}_1, \hat{p}_1, \hat{q}_2, \hat{p}_2, \ldots, \hat{q}_N, \hat{p}_N)$ and the basis $\hat{\boldsymbol{R}}' = (\hat{q}_{\text{D}}, \hat{q}_1, \hat{q}_2, \ldots, \hat{q}_N, \hat{p}_{\text{D}}, \hat{p}_1, \hat{p}_2, \ldots, \hat{p}_N)$ and recall that

$$\hat{H} = \frac{1}{2}\hat{\boldsymbol{R}}^T F\,\hat{\boldsymbol{R}}, \qquad \Omega = \bigoplus_{i=1}^{N+1}\begin{pmatrix} 0 & 1 \\ -1 & 0 \end{pmatrix},$$
$$\hat{H} = \frac{1}{2}\hat{\boldsymbol{R}}'^T F'\,\hat{\boldsymbol{R}}', \qquad \Omega' = \begin{pmatrix} 0_{N+1} & \mathbb{1}_{N+1} \\ -\mathbb{1}_{N+1} & 0_{N+1} \end{pmatrix},$$

where F and F' are symmetric matrices. The notation is as follows: matrices M and M' are written in basis $\hat{\boldsymbol{R}}$ or $\hat{\boldsymbol{R}}'$ respectively. The corresponding Gaussian counterparts of the operators we defined in equations (2.76),(2.79) and (2.77) are:

$$\hat{\mathcal{H}}_{\text{FREE}} = \hat{\mathcal{H}}_{\text{D}} + \hat{\mathcal{H}}_{\phi}^{\text{UV}} \to F_{\text{FREE}} = F_{\text{D}} \oplus 0_{2N} + 0_2 \oplus F_{\phi}, \tag{4.12}$$

$$\hat{\rho}_0 = \hat{\rho}_{\text{D}_0} \otimes \hat{\rho}_{\text{F}_0} \to \sigma_0 = \sigma_{\text{D}_0} \oplus \sigma_{\text{F}_0}, \tag{4.13}$$

$$\hat{\mathcal{H}}_{\text{INT}}^{\text{UV}},\ \hat{U} \to F_{\text{INT}},\ S = e^{\Omega F_{\text{INT}} T}, \tag{4.14}$$

where T denotes the duration of the coupling as in (4.6). In this case we see that initial vector of first moments, $\bar{\boldsymbol{r}}_0$, as defined in Eq. (2.79) is identically zero. This is because the initial Gaussian states of the different systems, the field and the probe, are not displaced (they are either the ground or thermal states). Since the Hamiltonian that rules the evolution does not have a linear term that displaces the Gaussian state (i.e. $\boldsymbol{\alpha}$ defined in Eq. (2.76)), the vector of moments $\boldsymbol{r} = S\boldsymbol{r}_0$ remains identically zero throughout the interaction.

The initial state of the probe is always the ground state so that $\sigma_{\text{D}_0} = \mathbb{1}_2$. The initial state of the field is a thermal state of inverse temperature $\beta \coloneqq 1/k_B T$, with respect to the Hamiltonian $\hat{\mathcal{H}}_{\phi}^{\text{UV}}$ in Eq. (4.10). In basis $\hat{\boldsymbol{R}}'$ the covariance matrix is

$$\sigma'_{\text{F}_0} = \begin{pmatrix} \dfrac{1}{\sqrt{M}} \coth\left(\beta mc^2 \sqrt{M}\right) & 0 \\ 0 & \sqrt{M} \coth\left(\beta mc^2 \sqrt{M}\right) \end{pmatrix}, \tag{4.15}$$

where the symmetric matrix M is defined, from Eq. (4.10), as

$$\hat{\mathcal{H}}_{\phi}^{\text{UV}} = \frac{mc^2}{2} \hat{\boldsymbol{p}}^T \hat{\boldsymbol{p}} + \frac{mc^2}{2} \hat{\boldsymbol{q}}^T M \hat{\boldsymbol{q}}, \tag{4.16}$$

with $\hat{\boldsymbol{q}} = (\hat{q}_1, \hat{q}_2, \ldots, \hat{q}_N)$ and $\hat{\boldsymbol{p}} = (\hat{p}_1, \hat{p}_2, \ldots, \hat{p}_N)$. We observe that that the ground state is a particular thermal state with $T = 0$. In that case, we obtain (4.15) with $\coth\left(\beta mc^2 \sqrt{M}\right) = 1$.

The composite system obeys $\sigma = S\sigma_0 S^T$. The state of the detector can be easily obtained as the submatrix $\sigma_{\text{D}} \coloneqq \sigma_{1:2,1:2}$. We will use the following notation:

$$\sigma_{\text{D}} = \begin{pmatrix} \sigma_{qq} & \sigma_{qp} \\ \sigma_{pq} & \sigma_{pp} \end{pmatrix} \tag{4.17}$$

We note, once again that in this case, $\langle \hat{q}_{\text{D}} \rangle = \langle \hat{p}_{\text{D}} \rangle = 0$, since the vector of moments $\bar{\boldsymbol{r}}$ remains identically zero throughout the interaction. For future purposes, we define

operator $\hat{r}_{\mathrm{D}} = (\hat{q}_{\mathrm{D}} + \hat{p}_{\mathrm{D}})/\sqrt{2}$. In this case, $\langle \hat{r}_{\mathrm{D}} \rangle = 0$ and $\sigma_{rr} = \langle \hat{r}_{\mathrm{D}}^2 \rangle - \langle \hat{r}_{\mathrm{D}} \rangle^2 = \langle (\hat{q}_{\mathrm{D}} + \hat{p}_{\mathrm{D}})^2/2 \rangle = (\sigma_{qq} + \sigma_{pp} + \sigma_{pq} + \sigma_{qp})/2$. We can now derive the marginals of the state of the probe, as explained in Section 2.8, as

$$\psi(x) = \frac{1}{\sqrt{2\pi\sigma_{qq}}} \exp\left[-\frac{x^2}{2\sigma_{qq}}\right], \tag{4.18}$$

$$\psi(p) = \frac{1}{\sqrt{2\pi\sigma_{pp}}} \exp\left[-\frac{p^2}{2\sigma_{pp}}\right], \tag{4.19}$$

$$\psi(r) = \frac{1}{\sqrt{2\pi\sigma_{rr}}} \exp\left[-\frac{r^2}{2\sigma_{rr}}\right]. \tag{4.20}$$

This means that when a measurement is made of operator $\hat{q}_{\mathrm{D}}$, the outcomes will follow a normal distribution of mean 0 and variance σ_{qq}. Therefore, to computationally imitate a measurement of observable $\hat{q}_{\mathrm{D}}$ one just has to pick q following the distribution $\mathcal{N}(0, \sigma_{qq})$. Equivalently, measuring the other observables $\hat{p}_{\mathrm{D}}$ and $\hat{r}_{\mathrm{D}}$ is equivalent to picking p and r from $\mathcal{N}(0, \sigma_{pp})$ and $\mathcal{N}(0, \sigma_{rr})$ respectively.

In the following section, we describe the measurement protocol that measures some observables of the detector at different times.

4.4 Measurement protocol

In this section, we propose a simple measurement protocol to produce labelled data (from a harmonic oscillator probe coupled locally to a quantum field) that can then be processed to learn about different features of QFT. This measurement protocol does not make any assumption about the nature of the field and replicates the type of measurements usually performed in labs, in particular with heterodyne detection.

As we explained, the local probe is a harmonic oscillator with free Hamiltonian $\hat{\mathcal{H}}_{\mathrm{D}}$ given in (4.2), where $\hat{q}_{\mathrm{D}}$ and $\hat{p}_{\mathrm{D}}$ are the probe's quadrature operators satisfying $[\hat{q}_{\mathrm{D}}, \hat{p}_{\mathrm{D}}] = \mathrm{i}$. We take the probe to couple to a general field linearly via (4.3) with $\hat{\mu}_{\mathrm{D}} = \hat{q}_{\mathrm{D}}$. Our measurement procedure is as follows:

1. Initialize the field according to some choice of label y.

2. Initialize the probe to its ground state. Couple the probe locally to the field at time $t = 0$ and let it couple to the field according to a switching function $\chi(t)$.

3. At time $t_m = T_{\text{MIN}}$, perform a projective measurement of the probe's $\hat{q}_{\text{D}}$ quadrature and record the result.

4. Repeat steps $1-3$ but measuring $\hat{p}_{\text{D}}$, then repeat steps $1-3$ but measuring the observable $\hat{r}_{\text{D}} = (\hat{q}_{\text{D}} + \hat{p}_{\text{D}})/\sqrt{2}$.

5. Repeat steps $1-4$ a total of $N_{\text{TIMES}} - 1$ more times increasing t_m by Δt each time.

6. Repeat this whole process N_{TOM} times.

This measurement procedure yields data $D_{\text{raw}} \in \mathbb{R}^{N_{\text{M}}}$, where $N_{\text{M}} = 3 \times N_{\text{TIMES}} \times N_{\text{TOM}}$ along with an associated label, y. Notice that this particular measurement protocol was explained for illustration: it can be done using different observables and different choices for the probe model. Even though this procedure could be applied in a lab, in our case, we do not have access to raw data coming from experiments. In the following section we explain how we generate data mimicking projective measurements and how we process it.

4.5 Data generation

To generate data, our code replicates the measurement protocol. To make it as clear as possible, we write the steps of the protocol using the Gaussian formalism in Section 2.8 and its physical meaning:

1. Choose a particular F_ϕ (the Gaussian equivalent to $\hat{H}_\phi$ in Eq. (2.76)) and a particular initial state σ_{F} (the Gaussian equivalent to $\hat{H}_\phi$ in Eq. (2.79)) according to some choice of label y. In other words, choose the free Hamiltonian of the field and its initial state.

2. Compute the initial state of the probe, which is its ground state, $\sigma_0 = \mathbb{1}_2$. Compute the initial joint state $\sigma = \sigma_0 \oplus \sigma_{\text{F}}$. Compute $S(t_m) = e^{\text{i}\Omega F_{\text{INT}} t_m}$. Compute $\sigma(t_m) = S(t_m)\sigma_0 S(t_m)^T$. The state of the probe is $\sigma_{\text{D}} := \sigma_{1:2,1:2}$. In other words, couple the probe locally to the field at time $t = 0$ and let it evolve for some time t_m (recall that $\chi(t)$ is a step function, as in (4.6)).

3. Obtain a value $q(t_m)$ from the normal distribution $\mathcal{N}(0, \sigma_{qq}(t_m))$. As explained in Section 4.3, this is equivalent to, at time $t_m = T_{\text{MIN}}$, perform a projective measurement of the probe's $\hat{q}_{\text{D}}$ quadrature and record the result.

4. Repeat steps $1-3$ but picking $p(t_m)$ from the normal distribution $\mathcal{N}(0, \sigma_{pp}(t_m))$ (measuring $\hat{p}_{\text{D}}$), then repeat steps $1-3$ but $r(t_m)$ from the normal distribution $\mathcal{N}(0, \sigma_{rr}(t_m))$(measuring $\hat{r}_{\text{D}} = (\hat{q}_{\text{D}} + \hat{p}_{\text{D}})/\sqrt{2}$).

5. Repeat steps $1-4$ a total of $N_{\text{TIMES}} - 1$ more times increasing t_m by Δt each time.

6. Repeat this whole process N_{TOM} times.

Following this procedure would result in a data set of $N_{\text{M}} = 3 \times N_{\text{TOM}} \times N_{\text{TIMES}}$ real numbers. For instance the values may look like those shown in Table 4.1, where $T_{\text{MAX}} = T_{\text{MIN}} + (N_{\text{TIMES}} - 1)\,\Delta t$

	q	r	p				
T_{MIN}	-0.752	-1.795	+1.128	...	+2.174	+0.499	-0.754
$T_{\text{MIN}} + \Delta t$	-0.651	-0.118	+0.075	...	+0.592	+0.426	-0.487
$T_{\text{MIN}} + 2\,\Delta t$	-0.525	+2.612	-0.587	...	+0.242	-0.815	-0.092
...		...		...		...	
T_{MAX}	+1.134	+0.232	-2.275	...	-0.007	-0.460	+0.738

N_{TOM} triples

Table 4.1: Possible Local Probe Measurement Data

Note that each of our N_{TOM} measurements of $\hat{q}_{\text{D}}(t)$, denoted as $q_k(t)$, are independent and identically distributed (here, $t = T_{\text{MIN}} + m\Delta t,\ m \in \{0, \ldots, N_{\text{TIMES}} - 1\}$). We can summarize these measurement outcomes, q_k, via their sample mean and sample variance,

$$\bar{q}(t) = \frac{1}{N_{\text{TOM}}} \sum_{k=1}^{N_{\text{TOM}}} q_k(t), \qquad \bar{s}_q^2(t) = \frac{1}{N_{\text{TOM}} - 1} \sum_{k=1}^{N_{\text{TOM}}} \big(q_k(t) - \bar{q}(t)\big)^2 \tag{4.21}$$

As discussed in Section 4.3, the outcomes $\hat{q}_k(t)$ follow the distribution $\mathcal{N}(0, \sigma_{qq}(t))$. Therefore, the sample mean, $\bar{q}(t)$, and sample variance, $\bar{s_q}^2(t)$, are *sufficient* statistics to summarize the information of the N_{TOM} measurements and thus the compression is lossless.

Similarly we can losslessly compress the measurements of $\hat{q}_{\text{D}}$, $\hat{r}_{\text{D}}$ and $\hat{p}_{\text{D}}$ at each time $t = T_{\text{MIN}} + m\Delta t$. Once compressed, our data is described by N_{TIMES} sextuplets of the form $\{\bar{q}(t), \bar{r}(t), \bar{p}(t), \bar{s}_q^2(t), \bar{s}_r^2(t), \bar{s}_p^2(t)\}$ and can be represented by a vector $D_{\text{COMP}} \in \mathbb{R}^d$ where

$d = 6\,N_{\text{TIMES}}$. Notice that even after compression the data may be high-dimensional since N_{TIMES} will generally be very large.

Once this analysis is done, we realize that our code can be sped up when generating the N_{TIMES} sextuplets. As each $q_k \sim \mathcal{N}(0, \sigma_{qq}(t))$ then we have

$$\bar{q}(t) = \frac{1}{N_{\text{TOM}}} \sum_{k=1}^{N_{\text{TOM}}} q_k(t) \sim \mathcal{N}\big(0, \frac{\sigma_{qq}(t)}{\sqrt{N_{\text{TOM}}}}\big), \tag{4.22}$$

$$\bar{s}_q^2(t) = \frac{1}{N_{\text{TOM}} - 1} \sum_{k=1}^{N_{\text{TOM}}} \big(q_k(t) - \bar{q}(t)\big)^2 \sim \sigma_{qq}(t) \frac{\chi^2(N_{\text{TOM}} - 1)}{N_{\text{TOM}} - 1}, \tag{4.23}$$

and similarly the other sample means and variances follow equivalent distributions.

Then, instead of generating every $q(t), p(t), r(t)$ a number of times N_{TOM}, we just generate the sextuplets $\{\bar{q}(t), \bar{r}(t), \bar{p}(t), \bar{s}_q^2(t), \bar{s}_r^2(t), \bar{s}_p^2(t)\}$ using their distribution at each time $t = T_{\text{MIN}} + m\Delta t,\ m \in \{0, \ldots, N_{\text{TIMES}} - 1\}$. From now on, a labeled data point generated this way will be called (D, y) with $D \in \mathbb{R}^{6N_{\text{TIMES}}}$, and y being the label.

4.6 Machine learning techniques

4.6.1 Preprocessing

As we discussed in the previous section, our measurement procedure and lossless compression produces labeled data (D, y) with $D \in \mathbb{R}^d$, where $d = 6N_{\text{TIMES}}$ and y is the label. To begin training we collect n instances of this labeled data (in both examples explained in this thesis, $n = 5000$), into a $n \times d$ design matrix $\boldsymbol{X} = (D_1, \ldots, D_n)^\intercal$ and a vector of labels $\boldsymbol{y} = (y_1, \ldots, y_n)^\intercal$. We use the first 75% of this data ($n_{\text{train}} = 0.75\,n$) to train the neural network, $\boldsymbol{X}_{\text{train}}$ and $\boldsymbol{y}_{\text{train}}$. We use the remaining 25% ($n_{\text{valid}} = 0.25\,n$) as validating data, $\boldsymbol{X}_{\text{valid}}$ and $\boldsymbol{y}_{\text{valid}}$, which will be used to test the accuracy of the trained network. Note that the network will not be exposed to any of the validation data during training.

After we generate the training data, we perform standard preprocessing [48]: we center the data, do principal component analysis, and whiten the data. Centering the data consists on subtracting from each datapoint, D_k, of the complet dataset, $\boldsymbol{X}$, the average of the *training* dataset, (i.e. we "center" the average of the transformed training data to

the zero vector). Mathematically this process can be expressed as $\boldsymbol{X} \to \boldsymbol{X} - \boldsymbol{X}^{\text{avg}}_{\text{train}}$, where

$$\boldsymbol{X}^{\text{avg}}_{\text{train}} = (D^{\text{avg}}_{\text{train}}, D^{\text{avg}}_{\text{train}}, \ldots, D^{\text{avg}}_{\text{train}})^\intercal, \qquad D^{\text{avg}}_{\text{train}} = \frac{1}{n_{\text{train}}} \sum_{k=1}^{n_{\text{train}}} D_k.$$

We note that $\boldsymbol{X}^{\text{avg}}_{\text{train}}$ is a $n \times d$ matrix.

Next we do principle component analysis (PCA), which finds a set of "uncorrelated" vectors to represent the training dataset $\boldsymbol{X}_{\text{train}}$. To do this we compute the covariance matrix of our training data and perform a singular value decomposition on it,

$$\frac{1}{n_{\text{train}} - 1} \boldsymbol{X}^\intercal_{\text{train}} \boldsymbol{X}_{\text{train}} = U^\intercal \Lambda U = \sum_{j=1}^{d} \lambda_j \, \boldsymbol{\xi}_j \boldsymbol{\xi}_j^\intercal \tag{4.24}$$

where $U = (\boldsymbol{\xi}_1, \ldots, \boldsymbol{\xi}_d)^\intercal$ is the matrix of singular vectors, $\boldsymbol{\xi}_j \in \mathbb{R}^d$ (note that U has shape $d \times d$ and it is orthogonal $UU^\intercal = U^\intercal U = \mathbb{1}_d$). The diagonal matrix $\Lambda = \text{diag}(\lambda_1, \ldots \lambda_d)$ is the matrix of singular values, $\lambda_j \in \mathbb{R}_+$. The singular vectors are the directions in our data that vary independently and the singular values indicate the strength of the variance in each direction. Using this decomposition we can rewrite our data in this singular basis by taking $\boldsymbol{X} \to \boldsymbol{X} U^\intercal$. After this transformation the training data has a diagonal covariance matrix, namely Λ. Finally we can whiten the data by taking $\boldsymbol{X} \to \boldsymbol{X} \Lambda^{-1/2}$. The covariance matrix of the training data is now the identity matrix. The data would now be ready to begin training the neural network.

4.6.2 Neural network training

Neural networks work by alternatingly applying tuneable linear-affine transformations (controlled by weights and biases) and fixed non-linear transformations (the activator function) to their inputs. See Fig. 4.1 for a schematic of a neural network that can be used to classify the topology of a QFTs based on local probe measurement data.

We will now use the architecture in Fig. 4.1 as a basic illustrative example. In this example the network accepts a 5-dimensional input, $\boldsymbol{x}^{(0)}$, into the left-most layer of the network (note that in the examples discussed in the main text the input dimension is much larger). In passing this data to the next layer of the network, a linear-affine transformation is applied to $\boldsymbol{x}^{(0)}$ as, $\boldsymbol{x}^{(1)} = W^{(1)} \boldsymbol{x}^{(0)} + \boldsymbol{b}^{(1)}$. The weight matrix $W^{(1)}$ here has dimensions 7×5 and the bias vector has a dimension of 7 such that $\boldsymbol{x}^{(1)}$ is 7-dimensional. The $7 \times 5 + 7 = 42$ values that determine this linear-affine transformation are left as free

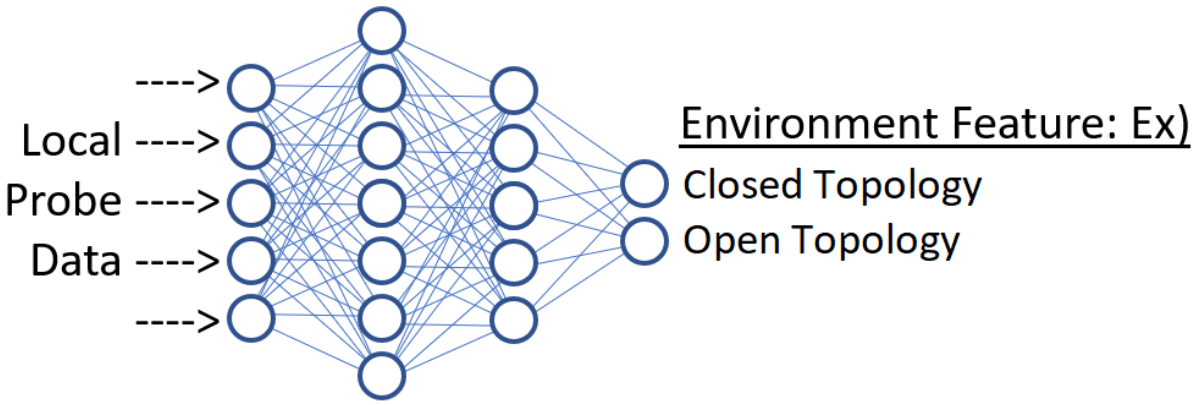

Figure 4.1: A schematic example of a neural network for processing local probe data to learn about features of a QFT.

parameters to be optimized during training. Next, a fixed non-linear function, $\mathcal{N}^{(1)}$ is applied element-wise to each entry of $\boldsymbol{x}^{(1)}$ yielding $\boldsymbol{z}^{(1)} = \mathcal{N}^{(1)}(\boldsymbol{x}^{(1)})$. For instance $\mathcal{N}^{(1)}$ may be the hyperbolic tangent function or a rectified linear unit.

This process is then repeated at each layer. First a linear affine transformation is applied to $\boldsymbol{z}^{(1)}$ as $\boldsymbol{x}^{(2)} = W^{(2)}\boldsymbol{z}^{(1)} + \boldsymbol{b}^{(2)}$ where $W^{(2)}$ has dimensions 5×7 and $\boldsymbol{b}^{(2)}$ has dimension 5. Then a fixed non-linear function, $\mathcal{N}^{(2)}$ is applied element-wise to $\boldsymbol{x}^{(2)}$ yielding $\boldsymbol{z}^{(2)} = \mathcal{N}^{(2)}(\boldsymbol{x}^{(2)})$. In the final layer we have $\boldsymbol{x}^{(3)} = W^{(3)}\boldsymbol{z}^{(2)} + \boldsymbol{b}^{(3)}$ where $W^{(3)}$ has dimensions 2×5 and $\boldsymbol{b}^{(3)}$ has dimension 2 and $\boldsymbol{z}^{(3)} = \mathcal{N}^{(3)}(\boldsymbol{x}^{(3)})$ for some non-linear function, $\mathcal{N}^{(3)}$. In total this network computes the function $f(\boldsymbol{x}^{(1)}; W, b) = \boldsymbol{z}^{(3)}$ where W and b refer to this network's 94 free parameters collectively.

There are two different problem types we need to design a network for, classification and regression. In classification, our network is tasked with deciding to which of several classes (given by a discrete label y) our data belongs. In this scenario, we take the number of neurons in the final layer to be equal to the number of classes and take the final activation function to be a soft-max. This allows us to interpret the network's output as a probability assignment that the input data belongs to each class. In regression, our network is tasked with assigning the data a continuous label y. In this case, we take the final layer to have a single neuron.

In the examples discussed in Section 4.7, 4.8 and 4.9, we considered a network consisting of 60 neurons on the input layer, 30 in the intermediate (hidden) layer and either 2 or 1 neurons in the final layer in the boundary sensing and thermometry cases respectively. All

of the non-linear activator functions were taken to be leaky rectified linear units.

The network's weights and biases are tuned to minimize error of the network's predictions over the training set. To quantify this error we define the following cost functions,

$$\text{Classification:} \qquad C(W,b) = \frac{-1}{n_{\text{train}}} \sum_{k=1}^{n_{\text{train}}} \tilde{y}_k \cdot \log(f(\boldsymbol{x}_k; W, b)) \tag{4.25}$$

$$\text{Regression:} \qquad C(W,b) = \frac{1}{n_{\text{train}}} \sum_{k=1}^{n_{\text{train}}} (f(\boldsymbol{x}_k; W, b) - y_k)^2 \tag{4.26}$$

where $\tilde{y}_k$ is the one-hot encoding of the k^{th} data point's label. For the classification scenario, our cost function is the cross entropy between the network's probability assignment and the expected result. For the regression case, the cost function is the mean square error. To help reduce overfitting we add an L_2 regularizer to this cost function, $\sim \lambda_2 ||W||_2$. This penalizes the network for using large weights. Additionally when training the network we randomly "drop" some fraction of the neurons. This forces the network to be more robust. The sum of the cost function and the regularizer are then minimized by stochastic gradient descent.

4.7 Boundary sensing example

In this section, we are going to study the sensitivity of a detector to changes in boundary conditions of the field. We are going to generate data containing outputs of the probe with the label corresponding to their particular boundary condition. We are going to process the outcomes of the probe and train a neural network to classify this data. Finally, we are going to test the network with unseen data and study how the accuracy of the results depends on the duration of the coupling of the probe to the field.

4.7.1 Setting different boundary conditions

In this section we are going to consider a detector coupled to one extreme of the cavity, $x = 0$. That means that the smearing function is a Gaussian function centered at $x_{\text{D}} = 0$, as in equation (4.7), i.e. the interaction Hamiltonian is:

$$\hat{\mathcal{H}}_{\text{INT}} = \frac{a\,\lambda_0}{\sigma\sqrt{2\pi}}\,\chi(t) \sum_{n=1}^{N} e^{-x_n^2/2\sigma^2}\,\hat{q}_{\text{D}} \otimes \hat{q}_n. \tag{4.27}$$

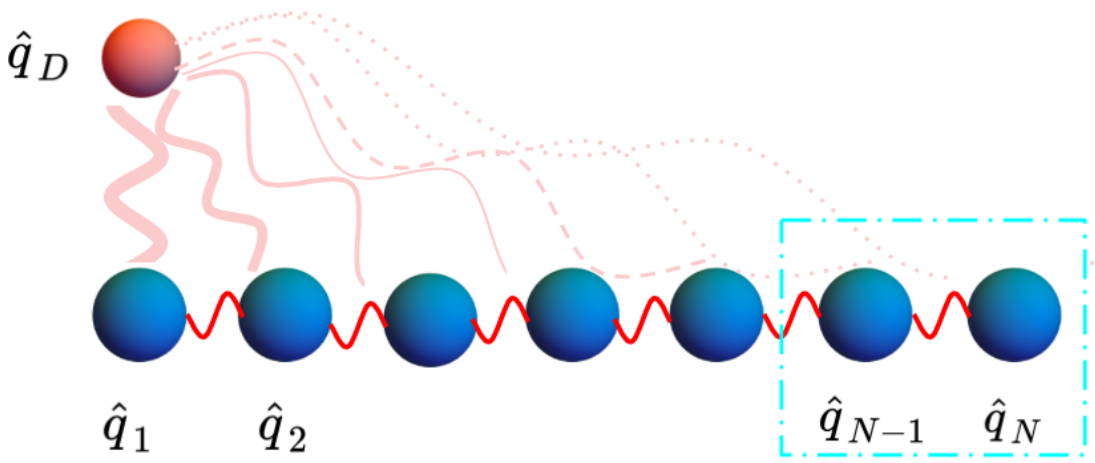

Figure 4.2: Visual representation of $\hat{\mathcal{H}}_{\text{FULL}}$.
The strength of the interaction between the detector and the different modes decreases as a Gaussian function. In this case, the second-to-last and last detector are xx-coupled.

To simulate a change of boundary condition, we will modify the coupling of the lattice to the spatial mode farthest from the probe. We first consider the two following free Hamiltonians for the field, labelled "Full" and "Cut", which are exactly equation (4.10) and a slight modification of it:

$$\hat{\mathcal{H}}_{\text{FULL}} = \sum_{n=1}^{N}\left[\frac{mc^2}{2}\hat{p}_n^2 + \left(\frac{mc^2}{2}+\frac{\hbar^2}{ma^2}\right)\hat{q}_n^2\right] + \sum_{n=1}^{N-1}\frac{\hbar^2}{ma^2}\hat{q}_{n+1}\hat{q}_n,$$

$$\hat{\mathcal{H}}_{\text{CUT}} = \sum_{n=1}^{N}\left[\frac{mc^2}{2}\hat{p}_n^2 + \left(\frac{mc^2}{2}+\frac{\hbar^2}{ma^2}\right)\hat{q}_n^2\right] + \sum_{n=1}^{\textcircled{N-2}}\frac{\hbar^2}{ma^2}\hat{q}_{n+1}\hat{q}_n. \tag{4.28}$$

In other words, $\hat{\mathcal{H}}_{\text{FULL}} = \hat{\mathcal{H}}_{\text{CUT}} + \dfrac{\hbar^2}{ma^2}\hat{q}_N\hat{q}_{N-1}$

Visually, the two different scenarios are depicted in Figures 4.2 and 4.3. We summarize the modified couplings that we consider in Table 4.2.

In this section, we are trying to differentiate the "full" boundary condition and the "cut" boundary condition. For this purpose we will generate, as per the data generation in Section 4.5, "time-series" data (remember that this data was composed by means and

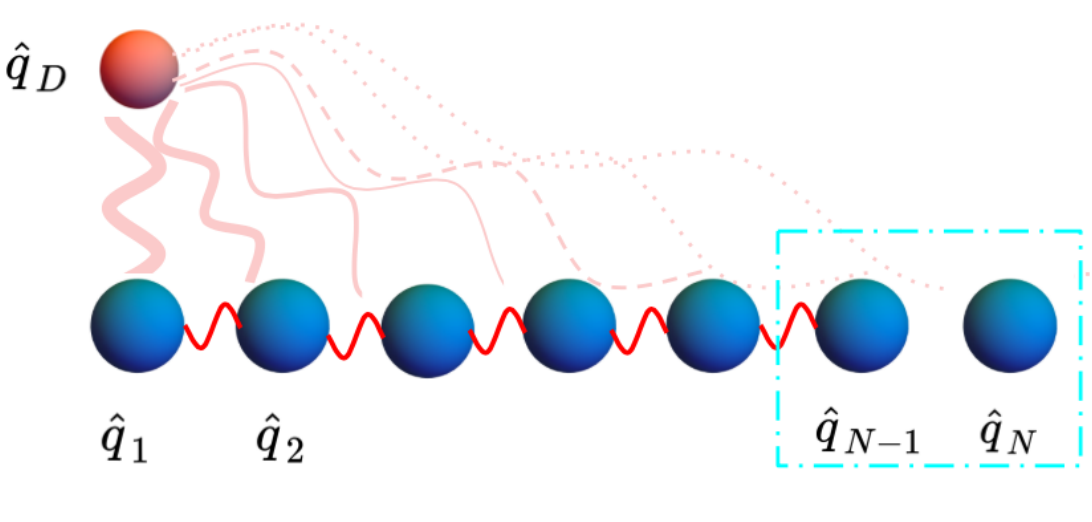

Figure 4.3: Visual representation of $\hat{\mathcal{H}}_{\text{CUT}}$.
We see that the strength of the interaction between the detector and the different modes decreases as a Gaussian function. In this case, the second-to-last and last detector are not xx-coupled.

y-label	Name	$\hat{H}_{\text{last}}$ for $t < 0$		$\hat{H}_{\text{last}}$ for $t \geq 0$
y=1	Full Bond	g	$\hat{q}_{N-1} \otimes \hat{q}_N$	Same as $t < 0$
y=2	Cut Bond	0	$\hat{q}_{N-1} \otimes \hat{q}_N$	Same as $t < 0$

Table 4.2: Modifications to the coupling between $\hat{q}_{N-1}$ and $\hat{q}_N$, connecting the last spatial mode to the rest of the lattice. $g = \hbar^2/ma^2$.

variances of independent runs of the experiment) from time T_{MIN} to time T_{MAX}. We choose the initial state (with this we mean at $t = 0$, not $t = T_{\text{MIN}}$) of the modes to be the ground state. An interesting question to ask is how well the neural network classifies the labelled data depending on the interval of time considered in the data generation. Is the network able to distinguish the two cases before a signal can bounce from the boundary? Is the UV-induced discretization explained in Section 2.4 allowing superluminal signalling?

In order to answer these questions we need to know the speed of signalling in this setting. To do this we introduce a new scenario in which a signal is introduced at time $t = 0$. In that case, the Hamiltonian is given by:

$$\hat{\mathcal{H}}_{\text{SIGNAL}}(t) = \hat{\mathcal{H}}_{\text{CUT}} + \Theta(t)\frac{\hbar^2}{ma^2}\hat{q}_N\hat{q}_{N-1}, \tag{4.29}$$

where $\Theta(t) = 0$ for $t < 0$ and $\Theta(t) = 1$ for $t > 0$. The Hamiltonian in this case is exactly the same to the $\hat{\mathcal{H}}_{\text{CUT}}$ before $t < 0$. In Fig. 4.4 we have a visual representation of this Hamiltonian.

At $t = 0$ this "instant" connection between modes $\hat{q}_{N-1}$ and $\hat{q}_N$ induces a signal that the neural network might be able to detect. To make this easier to distinguish, we choose the initial state of mode $\hat{q}_N$ to be a squeezed state of 8 dB instead of the vacuum state. We then train the neural network to differentiate between case CUT and SIGNAL, as summarized in Table 4.7.1.

y-label	Name	$\hat{H}_{\text{last}}$ for $t < 0$	$\hat{H}_{\text{last}}$ for $t \geq 0$	Initial state of mode N
y=2	Cut Bond	$0 \quad \hat{q}_{N-1} \otimes \hat{q}_N$	Same as $t < 0$	vacuum state
y=3	Signal	$0 \quad \hat{q}_{N-1} \otimes \hat{q}_N$	$g \quad \hat{q}_{N-1} \otimes \hat{q}_N$	squeezed state, 8dB

Table 4.3: Modifications to the coupling between $\hat{q}_{N-1}$ and $\hat{q}_N$, connecting the last spatial mode to the rest of the lattice. $g = \hbar^2/ma^2$.

In summary, we will train two neural networks for the following two tasks:

- Distinguish cases FULL and CUT (cases 1 and 2)
- Distinguish cases CUT and SIGNAL (cases 2 and 3)

Comparing cases 2 and 3 will allow us to measure the signal-propagation speed on the lattice explicitly. In both cases, the field (neglecting the last spatial mode) is in exactly the same state prior to $t = 0$. This disturbance will then propagate and eventually arrive at our probe system. Thus we can define the effective signalling time as the time it takes the probe to differentiate between cases 2 and 3. Importantly, if the probe is able to differentiate cases 1 and 2 in less than this effective signalling time, it cannot be due to having received a signal from the boundary. Moreover, if our probe is able to differentiate these cases in less than twice the effective signalling time, it can not be due to the probe bouncing a signal off the boundary.

4.7.2 Performance of the neural network

To illustrate how our analysis can work in realistic scenarios, we consider a detector of atomic size. This detector could model, for example, a trapped ion in a potential. As explained in Section 2.3, Unruh-DeWitt detectors captured the "scalar essence" of the

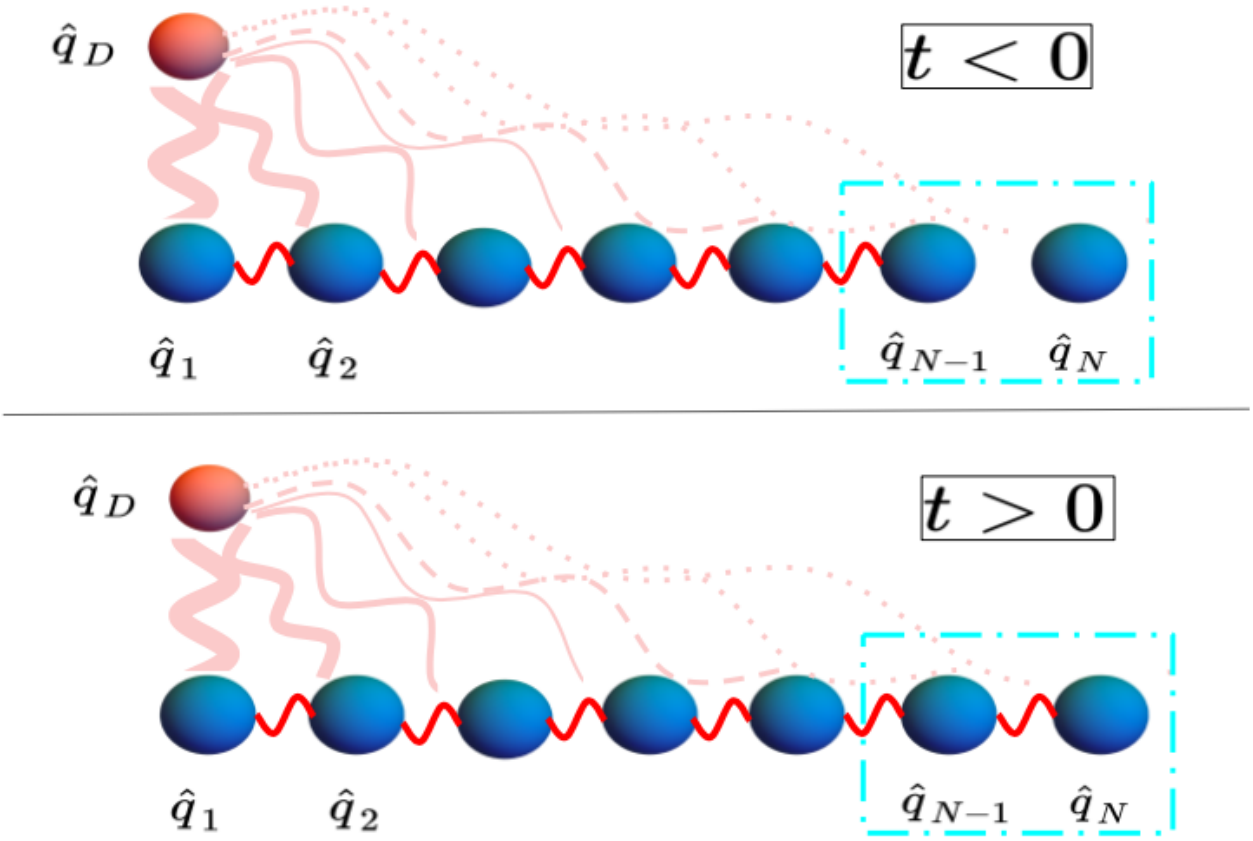

Figure 4.4: Visual representation of $\hat{\mathcal{H}}_{\text{SIGNAL}}$.
We see that the strength of the interaction between the detector and the different modes decreases as a Gaussian function. In this case, the second-to-last and last detector are not xx-coupled for $t < 0$ and they are xx-coupled for $t > 0$.

electromagnetic interaction between an atom and the electromagnetic field [105]. With this in mind, we choose a detector with Gaussian smearing function of width, $\sigma = 53$ pm.

Taking the UV-cutoff at $K = 16/\sigma$ gives us a lattice spacing of $a = \pi/K = 10.4$ pm. We take the boundary to be at a distance $L = 90\,a = 4.7\,\sigma = 457$ nm. We can quantify how much this discretization changes the dispersion relation of the field. For our parameters, the "average relative error" in the dispersion relation, introduced in Section 2.7, is 0.16%. We take the detector to have an excitation energy $\hbar\omega_{\text{D}} = 130$ eV and the field to have a mass $mc^2 = 1$ eV. Note that in this example the field is approximately massless since its mass is more than a hundred times smaller than any other energy scale in the problem.

Finally, we investigate the strong coupling regime (which is non-perturbative), where the energy scale of the probe-field coupling is near the probe's free energy scale, so that $\lambda_0 = \hbar\omega_{\text{D}} = 130$ eV. Note that the choice of parameters is just for demonstration purposes; similar results were also obtained for a broad set of different parameters.

The results are plotted in Fig 4.5. We plot the accuracy of the neural network on distinguishing between the CUT, and SIGNAL cases with a triangle green line. From the green triangle line, we can derive the effective speed of propagation of a signal in the lattice. Since we generate a signal from the further boundary of the cavity at time $t = 0$, one would expect to be able to differentiate the CUT and SIGNAL at time $t_{\text{EFF}} = c_{\text{EFF}}(L - 7\sigma)$, where $L-7\sigma$ is the length of the cavity corrected to taking into account the extent of the Gaussian smearing of the detector. The green line in Fig.4.5 indicates that it is impossible for the network to distinguish between the CUT and SIGNAL cases in less than ≈ 15 as. Using this, we obtain that signal to edge of detector effective speed $c_{\text{EFF}} = (L - 7\sigma)/15$ as $= c$ is actually the speed of light (in Fig 4.5 a vertical red line indicates the light-crossing time from the end of the cavity to the detector, which coincides with the sudden improvement on the accuracy of the network). Indeed our toy model is very approximately relativistically causal, as a good quantum field theory on the lattice should be.

In the blue circle lines, we plot the ability for the neural network to distinguish between the CUT and FULL boundary conditions. In this case, we had to distinguish between the time-evolved states that were initialized as ground states of different Hamiltonians. In this case, the information about the boundary was scrambled all over the field and accessible locally: the ground state knows locally about its boundary conditions [96, 5]. Indeed, the network accuracy shows that the network can distinguish field boundary conditions before any signal propagates to the detector. This allows the probe to see the boundary 'without light', that is, in the vacuum state of the theory and much before the light-crossing time of the lattice. Notice that the network can accurately distinguish the two boundary conditions by considering a number of measurements that is still relatively small as compared with the typical number of atoms in a macroscopic sensor, $N_{\text{TOM}} = 10^{20} \ll N_{\text{A}} \approx 10^{24}$.

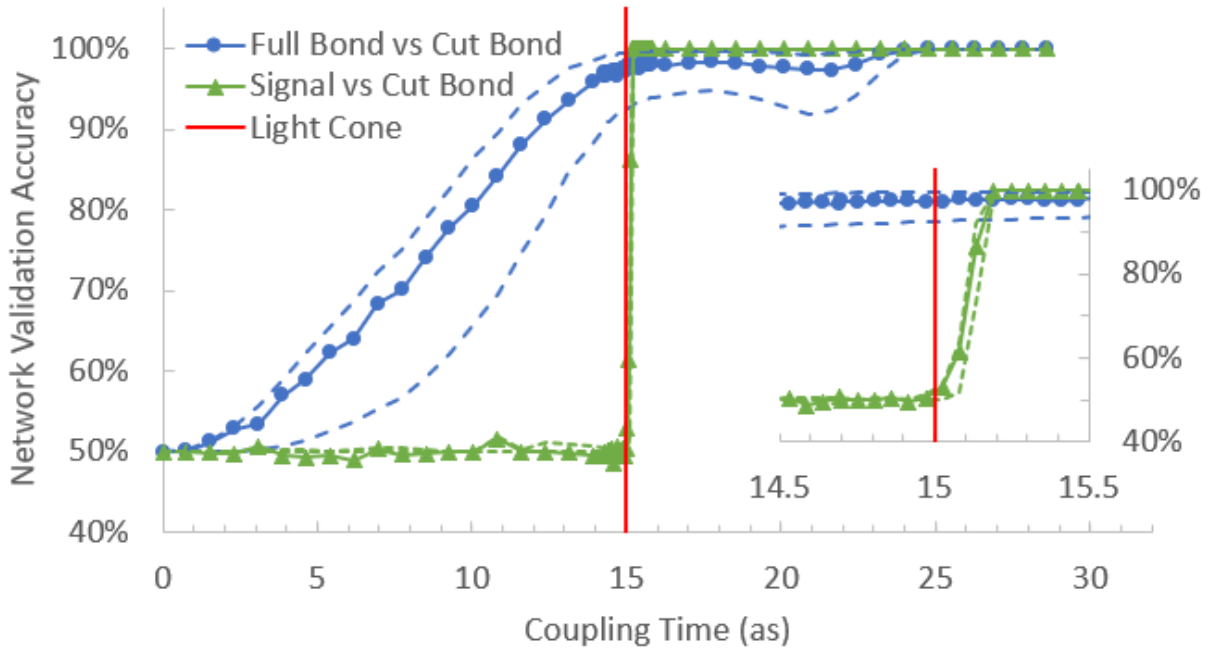

Figure 4.5: Accuracy of a neural network in distinguishing the boundary condition of a field.
We trained a neural network to predict the boundary condition of a quantum field from local probe data gathered far from the boundary. The network was asked a) to detect a signal sent from the boundary (green triangles) and b) to detect a modification of the field's boundary condition (blue circles). The network's accuracy (solid) and the theoretical bounds (dashed) are plotted as a function of the duration of the probe's interaction with the field. A point plotted at time t indicates the network's accuracy given measurements taken at $N_{\text{TIMES}} = 10$ measurement times between t and the previous plot point. The network was trained on $n_{\text{train}} = 3750$ examples. Each example summarizes $N_{\text{TOM}} = 10^{20}$ measurements of each of the probe's quadratures ($\hat{q}_{\text{D}}$, $\hat{r}_{\text{D}}$ and $\hat{p}_{\text{D}}$) at each measurement time. The inset shows details of the causal response to the detector to the signal. The vertical red line is at the edge-of-detector-to-boundary light-crossing time.

One may still have the lingering doubt of whether this neural network is performing optimally. In this case, we can find theoretical bounds for the network's performance, drawn in dashed lines in Fig 4.5. In the next section, we explain how we can find this bounds using the Hellinger distance.

4.7.3 Hellinger analysis

In the previous example, we trained the network to distinguish cases FULL and CUT (cases 1 and 2) or distinguish between cases CUT and SIGNAL (cases 2 and 3). Each of these tasks consists then of a binary classifications of 60-dimensional points of the following form:

$$\boldsymbol{x} = \left(\bar{q}(t), \bar{r}(t), \bar{p}(t), \bar{s}_q^2(t), \bar{s}_r^2(t), \bar{s}_p^2(t) \quad \text{for } t = T_{\text{MIN}},\ T_{\text{MIN}} + \Delta t,\ \ldots,\ T_{\text{MAX}}\right), \tag{4.30}$$

where $T_{\text{MAX}} - T_{\text{MIN}} = 10\Delta t$.

As explained in Section 4.3, each of the elements of this vector follow known probability distributions, detailed in Eqs. (4.22) and (4.23). Each of these elements are independently distributed (since the sample mean and sample variance of normal distributions are independent [41]). When we consider high tomography, i.e., the sample variance mean and the sample variance are computed with many experimental outcomes, we can use the central limit theorem to obtain the distributions of the sample mean and sample variance. For example, the sample mean $\bar{q}(t)$ and sample variance $\bar{s}_q^2(t)$ follow, in a high tomography approximation, the distributions

$$\bar{q}(t) \sim \mathcal{N}\left(0, \frac{\sigma_{qq}(t)}{\sqrt{N_{\text{TOM}}}}\right), \quad \bar{s}_q^2(t) \sim \sigma_{qq}(t)\frac{\chi^2(N_{\text{TOM}} - 1)}{N_{\text{TOM}} - 1} \sim \mathcal{N}\left(\sigma_{qq}(t), \frac{2\sigma_{qq}(t)}{N_{\text{TOM}} - 1}\right). \tag{4.31}$$

Since we know that each sample statistic, $\bar{q}(t), \bar{r}(t), \bar{p}(t), \bar{s}_q^2(t), \bar{s}_r^2(t)$ and $\bar{s}_p^2(t)$ follows a normal distribution, we obtain that the probability distribution of the 60-dimensional vector, $\boldsymbol{x}$, defined in Eq. (4.30), is a multivariate normal probability distribution. Then, to obtain $\boldsymbol{x}$ we can either 1) measure the probe 10^{24} times and calculate its sample statistics, $\bar{q}(t), \bar{r}(t), \bar{p}(t), \bar{s}_q^2(t), \bar{s}_r^2(t)$ and $\bar{s}_p^2(t)$ or 2) draw a point from a multivariate normal probability distribution with multivariate mean and sample:

$$\boldsymbol{\mu} = (\langle\hat{q}(t)\rangle, \langle\hat{r}(t)\rangle, \langle\hat{p}(t)\rangle, \sigma_{qq}(t), \sigma_{rr}(t), \sigma_{pp}(t) \quad \text{for } t = T_{\text{MIN}},\ T_{\text{MIN}} + \Delta t,\ \ldots,\ T_{\text{MAX}}) \tag{4.32}$$

$$\Sigma = \text{diag}\left(\frac{\sigma_{qq}(t)}{N_{\text{TOM}}}, \frac{\sigma_{rr}(t)}{N_{\text{TOM}}}, \frac{\sigma_{pp}(t)}{N_{\text{TOM}}}, \frac{2\sigma_{qq}^2(t)}{N_{\text{TOM}} - 1}, \frac{2\sigma_{rr}^2(t)}{N_{\text{TOM}} - 1}, \frac{2\sigma_{pp}^2(t)}{N_{\text{TOM}} - 1}, \text{ for } t = T_{\text{MIN}},\ \ldots,\ T_{\text{MAX}}\right). \tag{4.33}$$

This binary classification problem for the CUT and FULL boundary conditions can then be understood as knowing if a point comes from two different multivariate normal distributions corresponding to labels CUT and FULL. In general, a binary classification consists in distinguishing between two probability distributions $r_\theta(\boldsymbol{x})$ or $q_\theta(\boldsymbol{x})$, where θ is some free parameter of the problem. In terms of our scenario, θ describes the other details of the

scenario, like time T_{MIN}. We will say that $r_\theta(\boldsymbol{x})$ is associated to label $y = 0$ (that could stand for some boundary condition) and $q_\theta(\boldsymbol{x})$ is associated to label $y = 1$. The distributions $r_\theta(\boldsymbol{x})$ and $q_\theta(\boldsymbol{x})$ provide the odds that some particular data was produced given the state of the field and measurement procedure.

The optimal strategy (i.e., the one that maximizes your success probability) for this binary classification problem is to guess $y = 1$ if $q_\theta(\boldsymbol{x}) > r_\theta(\boldsymbol{x})$ and $y = 0$ if $r_\theta(\boldsymbol{x}) > q_\theta(\boldsymbol{x})$, breaking ties randomly. This strategy succeeds with probability of $p_{\text{success}} = \frac{1}{2}\big(1 + \text{TV}(r_\theta, q_\theta)\big)$ where

$$\text{TV}(r_\theta, q_\theta) = \frac{1}{2}\int \big|r_\theta(\boldsymbol{x}) - q_\theta(\boldsymbol{x})\big| \, \mathrm{d}\boldsymbol{x} \tag{4.34}$$

is the total variation distance between $r_\theta(\boldsymbol{x})$ and $q_\theta(\boldsymbol{x})$. If we can compute this distance, we can determine for which values of θ (e.g., for which coupling times) the distributions $r_\theta(\boldsymbol{x})$ and $q_\theta(\boldsymbol{x})$ are distinguishable.

The total variation distance is only useful for binary classification problems. It cannot be used in this way when there are more than two classes or for regression problems, such as our thermometry example. In the remote boundary sensing scenario, calculating the total variation distance directly is infeasible. An alternate approach is to compute upper and lower bounds on TV using the Hellinger distance, $H(r_\theta, q_\theta)$ [20], as

$$H(r_\theta, q_\theta)^2 \leq \text{TV}(r_\theta, q_\theta) \leq H(r_\theta, q_\theta)\sqrt{2 - H(r_\theta, q_\theta)^2} \tag{4.35}$$

where

$$H(r, q) = \frac{1}{\sqrt{2}}\sqrt{\int \left(\sqrt{r(\boldsymbol{x})} - \sqrt{q(\boldsymbol{x})}\right)^2 \mathrm{d}\boldsymbol{x}} \tag{4.36}$$

Usually, the Hellingher distance does not have a closed forom. Fortunately, the Hellinger distance is easy to compute for multivariate normal distribution, $r_\theta(\boldsymbol{x}) = \mathcal{N}(\boldsymbol{x}; \mu_r, \Sigma_r)$ and $q_\theta(\boldsymbol{x}) = \mathcal{N}(\boldsymbol{x}; \mu_q, \Sigma_q)$ for some means, μ_r and μ_q, and some covariances, Σ_q and Σ_r. The Hellinger distance between two such multivariate normal distributions is given by [20]

$$H(r_\theta, q_\theta)^2 = 1 - \left(\frac{\det(\Sigma_r \, \Sigma_q)}{\det(\overline{\Sigma}^2)}\right)^{\frac{1}{4}} \exp\left(-\frac{\Delta\mu^\intercal \overline{\Sigma}^{-1} \Delta\mu}{8}\right). \tag{4.37}$$

where $\Delta\mu = \mu_r - \mu_q$ and $\overline{\Sigma} = (\Sigma_r + \Sigma_q)/2$. Thus if we can compute the means and covariances of our data in the central limit, we can find bounds for the neural network's optimal performance.

In Fig. 4.5, we plot these bounds to the optimal performance of any network in dashed lines; in blue, to bound the ability to distinguish the FULL and CUT boundary conditions and, in green, to bound the ability to distinguish the SIGNAL and CUT. We observe than in both cases, the performance of our network is bounded by those dashed plots and therefore, our results are trustworthy.

4.8 Thermometry example

In this section, we are going to study the sensitivity of a detector to changes in KMS temperature of the field. We are going to generate data containing outputs of the probe with the label corresponding to the particular temperature. We are going to process the outcomes of the probe and train a neural network to perform a regression on this data. Finally, we are going to test the network with unseen data and study how the accuracy of the results depends on the duration of the coupling of the probe to the field.

4.8.1 Setting different temperatures

In this section we are going to consider a detector coupled to the center of the cavity, $x = L/2$. That means that the smearing function is a Gaussian function centered at $x_{\text{D}} = L/2$, as in equation (4.7), i.e. the interaction Hamiltonian is:

$$\hat{\mathcal{H}}_{\text{INT}} = \frac{a\,\lambda_0}{\sigma\sqrt{2\pi}}\,\chi(t)\sum_{n=1}^{N} e^{-(x_n-L/2)^2/2\sigma^2}\,\hat{q}_{\text{D}}\otimes\hat{q}_n. \tag{4.38}$$

The Hamiltonian of the field will be exactly the same as $\hat{H}_{\text{FULL}}$:

$$\hat{\mathcal{H}}_{\text{FULL}} = \sum_{n=1}^{N}\left[\frac{mc^2}{2}\hat{p}_n^2 + \left(\frac{mc^2}{2}+\frac{\hbar^2}{ma^2}\right)\hat{q}_n^2\right] + \sum_{n=1}^{N-1}\frac{\hbar^2}{ma^2}\hat{q}_{n+1}\hat{q}_n. \tag{4.39}$$

Fig. 4.6 is a visual representation of this type of coupling and of $\hat{H}_{\text{FULL}}$.

We want to be able to predict the temperature of the field using the outcomes of the probe. Therefore, we will generate data with a range of temperatures, i.e. the initial state of the field will be a thermal state of different temperatures (as in Eq. (4.15)). We recall that the initial state of the probe will be the ground state. We will associate temperature labels T if the initial state of the field has a temperature in the range $T \pm 10\%$. The labels

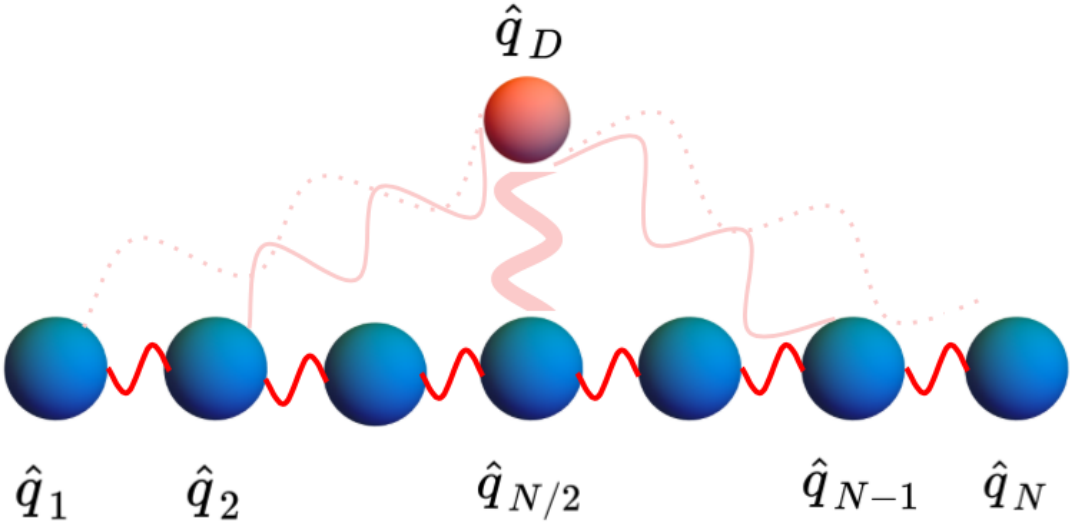

Figure 4.6: Visual representation of $\hat{\mathcal{H}}_{\text{FULL}}$, the Hamiltonian considered in the thermometer case.
The strength of the interaction between the detector and the different modes decreases as a Gaussian function, and it is placed in the middle of the cavity.

T will run from $300\mu K$ to $350\mu K$ in $10\mu K$ steps. We will train the neural network with this data. To check the accuracy of the network, we show it unseen data and plot the percentage of the data labelled correctly within $\pm 1\%$.

4.8.2 Performance of the neural network

To showcase the broad applicability of our framework, we consider a very different problem keeping the exact same measurement protocol, coupling between probe and field, and data-analysis ansatz.

We consider a probe motivated by a superconducting circuit undergoing a long-range interaction with an open transmission line in a thermal state. Such systems do not couple strongly to frequencies above 50 GHz [33, 42, 91]. Assuming a Gaussian profile we can match this behavior by taking $3/\sigma = 50$ GHz/c, i.e., $\sigma = 18$ mm [91]. Taking our UV-cutoff in the field at $K = 16/\sigma = 267$ GHz/c gives lattice spacing $a = \pi/K = 3.5$ mm. We couple the circuit to the center of a transmission line of length $L = 100\, a = 19.6\sigma = 353$ mm.

We take the circuit to have an energy gap typical of such systems, $\omega_{\text{D}} = 10$ GHz and

the field to have a mass $mc^2 = 0.1\text{GHz} \cdot \hbar$, much smaller than the other energy scales. We again consider strong-coupling: $\lambda_0/\hbar = \omega_{\text{D}} = 10$ GHz.

We trained the network to estimate the field's temperature based only on measurements of the local probe. Fig 4.7 shows the fraction of the validation data which the network able to label within $\pm 1\%$ of the actual temperature. Note that the neural network can determine the temperature very accurately even for very low transmission line temperature (sub-mK). It can do so even before the interaction's thermalization time scales which is lower-bounded by the detector's Heisenberg time, $1/\omega_{\text{D}} = 100$ ps.

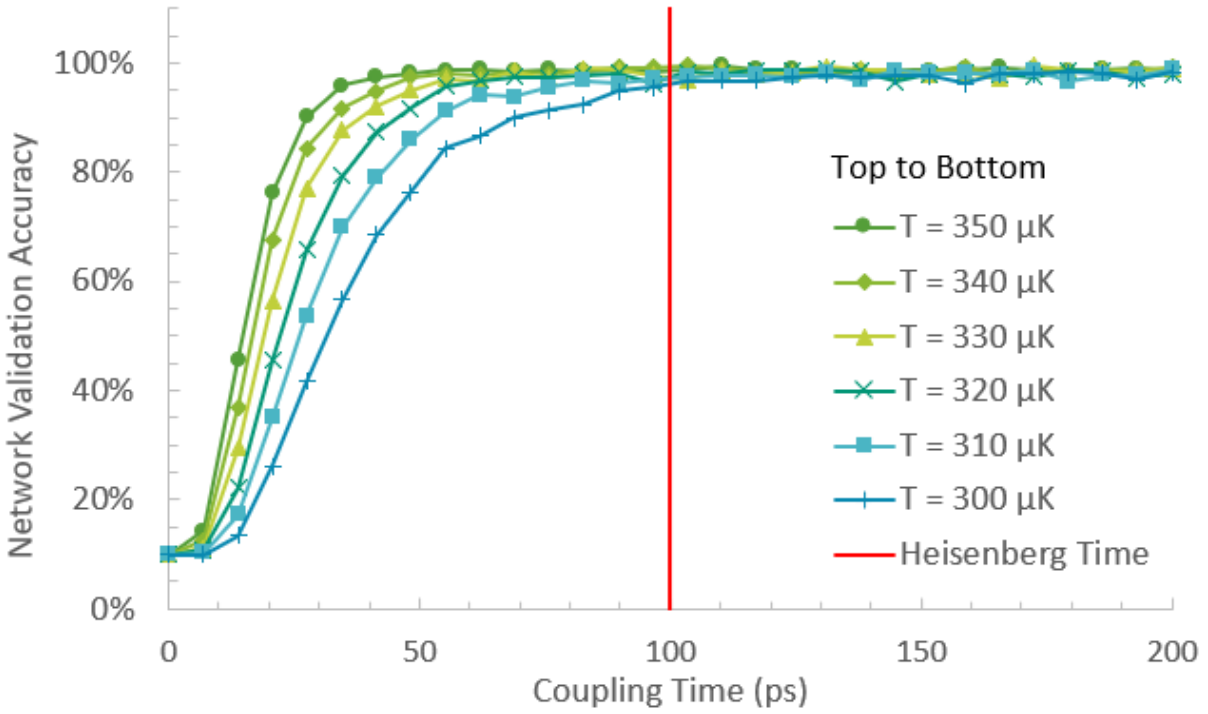

Figure 4.7: Accuracy of a neural network in predicting the temperature of a quantum field. A neural network trained to predict (through regression) the temperature of a quantum field from local probe data. The network was trained on labeled data corresponding to field temperatures from a range $T \pm 10\%$. The fraction of the validation data which the network labeled correctly to within $\pm 1\%$ is plotted as function of the duration of the probe's interaction with the field. A point plotted at time t indicates the network's accuracy given measurements taken at $N_{\text{TIMES}} = 10$ measurement times between t and the previous plot point. The network was trained on $n_{\text{train}} = 7500$ examples from each range. Each example summarizes $N_{\text{TOM}} = 10^{20}$ measurements of each of the probe's quadratures ($\hat{q}_{\text{D}}$, $\hat{r}_{\text{D}}$ and $\hat{p}_{\text{D}}$) at each measurement time. The vertical red line is the probe's Heisenberg time ω_{D}^{-1}.

4.9 A non-Gaussian Example: Distinction between a Fock State and a Phase-Averaged Coherent State

In this section we show that we can extend our results for scenarios in which we to no rely on 1) the Gaussianity of the probe/field states or, 2) the UV cutoff/bandlimit/discretization

taken in the main text. In this example, we will also show how to trivially extend the formalism of the main text to include the fourth moments of the probe system. A relevant problem in experimental quantum optics is to be able to tell apart Fock states (like a single photon state) from low amplitude coherent states (produced by stimulated emission) when the expectation of the number of photons in the state is the same.

Consider a massless scalar field in a $1+1$ dimensional cavity of length L with Dirichlet boundary conditions. It will be useful for us to take the following mode decomposition of the field operator,

$$\hat{\phi}(t,\boldsymbol{x}) = \sqrt{\frac{2}{L}} \sum_{m=1}^{\infty} \frac{\sin(\omega_m x)}{\sqrt{\omega_m}} \left(\hat{q}_m \cos(\omega_m t) + \hat{p}_m \sin(\omega_m t)\right), \tag{4.40}$$

where dimensionless quadrature operators $\hat{q}_n$ and $\hat{p}_m$ satisfy canonical commutation relations $[\hat{q}_n, \hat{p}_m] = \mathrm{i}\delta_{nm}$ and where $\omega_m = \pi m/L$. Note we have taken $\hbar = c = 1$ in this section.

We will take the field state to be the vacuum for all modes except for the lowest frequency one (the $m = 1$ mode). We will try to determine the initial state of the $m = 1$ mode by measuring a probe coupled locally to the field in the center of the cavity. We take the $m = 1$ mode to be in either a) a Fock state $|N\rangle$ with N excitations, or b) a phase-averaged coherent state with N excitations on average. That is, a coherent state $|\alpha\rangle$ for some $\alpha \in \mathbb{C}$ with $|\alpha|^2 = \langle\hat{n}\rangle = N$ but with an unknown phase. Note that, as we will see, neither of these states are Gaussian. The Wigner function for a Fock state is,

$$W_{\text{Fock}}(q,p;N) = \frac{(-1)^N}{\pi} L_N(2(q^2+p^2))\, e^{-(q^2+p^2)} \tag{4.41}$$

where $L_N(x)$ is the N^{th} Laguerre polynomial. For the unknown phase coherent state, the fact that we do not know (therefore average over) the phase makes this a non-Gaussian state. The Wigner function of a phase-averaged coherent state (PAC) is

$$W_{\text{PAC}}(q,p;N) = \frac{1}{\pi}\int_0^{2\pi} \frac{\mathrm{d}\theta}{2\pi}\, e^{-(q-\sqrt{N}\cos(\theta))^2-(p-\sqrt{N}\sin(\theta))^2}. \tag{4.42}$$

Moreover, we note that these two states have exactly the same first and second moments:

$$\langle\hat{q}\rangle_{\text{Fock;N}} = \langle\hat{p}\rangle_{\text{Fock;N}} = 0, \quad \langle\hat{q}\,\hat{p}\rangle_{\text{Fock;N}} = 0, \tag{4.43}$$

$$\langle\hat{q}^2\rangle_{\text{Fock;N}} = \langle\hat{p}^2\rangle_{\text{Fock;N}} = \langle\hat{n}+1/2\rangle_{\text{Fock;N}} = N+1/2, \tag{4.44}$$

and,

$$\langle \hat{q} \rangle_{\text{PAC;N}} = \langle \hat{p} \rangle_{\text{PAC;N}} = 0, \quad \langle \hat{q}\,\hat{p} \rangle_{\text{PAC;N}} = 0, \tag{4.45}$$

$$\langle \hat{q}^2 \rangle_{\text{PAC;N}} = \langle \hat{p}^2 \rangle_{\text{PAC;N}} = \langle \hat{n} + 1/2 \rangle_{\text{PAC;N}} = N + 1/2. \tag{4.46}$$

Thus no analysis of these two field states in terms of the first and second moments of these states can differentiate them; these field states can only be distinguished by methods that are sensitive to their third and higher order moments.

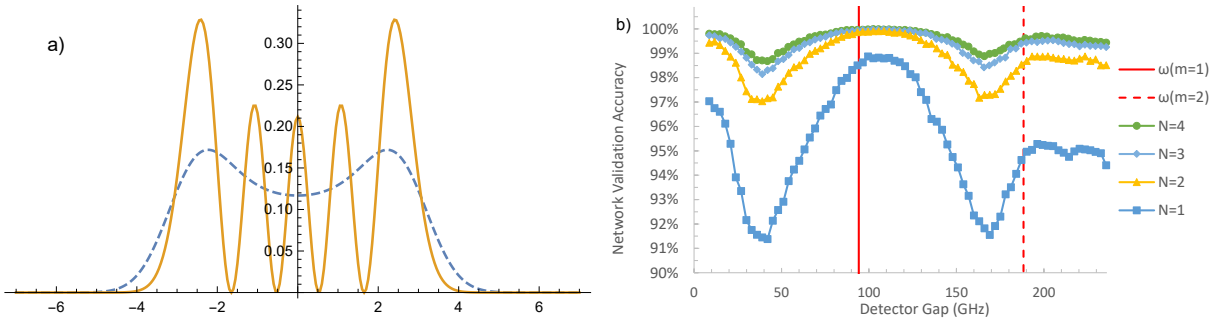

Figure 4.8: Marginal distributions for a Fock state and a phase averaged coherent states and the accuracy of a neural network to distinguish both.
a) The marginal distributions for the $N = 4$ Fock state (solid) and the phase averaged coherent state with $|\alpha|^2 = 4$ (dashed). The distributions are not Gaussian, and they have the same mean and variance, making them impossible to distinguish with simple statistical analysis of first and second moments. b) The validation accuracy of a neural network trained to distinguish two field states from the measurements of a local detector coupled to the field. In particular, the network differentiates vacuum cavity states with the following two modifications: 1) the lowest field mode is in an N-particle Fock state or 2) the lowest field mode is in a coherent state with expectation $\langle \hat{n}_1 \rangle = N$ particles and unknown phase.

It is a non-trivial task to determine in which of these states the field is. Suppose that (forgoing the localized probe system temporarily) we are somehow able to measure one of the quadrature operators of the lowest mode (e.g., $\hat{q}_1$) directly. The outcome of this measurement would be selected from the marginal distributions of $W_{\text{Fock}}(q, p; N)$ and $W_{\text{PAC}}(q, p; N)$. These are shown in Fig 4.8a for the case of $N = 4$. The total variation distance between these marginals is TV ≈ 0.29 such that best odds one can hope given a single measurement outcome is $(1 + \text{TV})/2 \approx 64.5\%$.

In actuality, we will attempt to distinguish these field states from the probe's response

to the field. This probe will pick up information from all of the field modes, much of which is irrelevant to the task at hand. Our machine learning algorithm will need to learn to distinguish the irrelevant noise from these other modes from the (already weak) signal from the $m = 1$ mode.

As in Section 4.2, we take the probe to be a harmonic oscillator coupled to the field through

$$\hat{\mathcal{H}}_{\text{INT}} = \lambda\, \chi(t) \int_{-\infty}^{\infty} \mathrm{d}\boldsymbol{x}\, F(\boldsymbol{x})\, \hat{q}_{\text{D}} \otimes \hat{\phi}(t, \boldsymbol{x}). \tag{4.47}$$

Unlike in the previous examples (Eq. (4.6)) we now consider a switching function $\chi(t) = \delta(t) + \delta(t - t_m)$ where t_m is a time just before we measure the probe. Otherwise the measurement procedure is identical as described in Section 4.4. Specifically, the probe undergoes a strong sudden interaction with the field $t = 0$. Then both the probe and field evolve freely for a time t_m. The probe undergoes another strong sudden interaction with the field at $t = t_m$. Finally, we measure one of the probe operators ($\hat{q}_{\text{D}}$, $\hat{p}_{\text{D}}$ or $\hat{r}_{\text{D}}$). This measurement procedure is repeated N_{TOM} times for each probe operator and at each of the N_{TIMES} measurement time t_m. It is important to note that since the field state is not Gaussian, these probe measurement values will not be distributed normally. The distributions they are drawn from are ultimately derived from the ones in the above figure and are much noisier due to noise from the other field modes.

As in the main text, we record the sample means and sample variances of these N_{TOM} measurements in our compressed data. However, as discussed above, we will need more than just first and second moments to handle this problem. Thus we additionally include the centered fourth moments of the distribution of sampled data (sample moments),

$$\bar{s}_{4,q}(t) = \frac{1}{N_{\text{TOM}}} \sum_{k=1}^{N_{\text{TOM}}} (q_k(t) - \bar{q}(t))^4, \tag{4.48}$$

$$\bar{s}_{4,r}(t) = \frac{1}{N_{\text{TOM}}} \sum_{k=1}^{N_{\text{TOM}}} (r_k(t) - \bar{r}(t))^4, \tag{4.49}$$

$$\bar{s}_{4,p}(t) = \frac{1}{N_{\text{TOM}}} \sum_{k=1}^{N_{\text{TOM}}} (p_k(t) - \bar{p}(t))^4. \tag{4.50}$$

where $t = t_m$ is one of our measurement times and $\{q_k(t_m)\}$ are the N_{TOM} measurements

of $\hat{q}_{\rm D}$ at $t = t_m$. Likewise for $\{r_k(t_m)\}$ and $\{p_k(t_m)\}$. Thus in total our compressed date is

$$\boldsymbol{x} = \left(\bar{q}(t), \bar{r}(t), \bar{p}(t), \bar{s}_q^2(t), \bar{s}_r^2(t), \bar{s}_p^2(t), s_{4,q}(t), s_{4,r}(t), s_{4,p}(t) \quad \text{for } t = T_{\rm MIN}, T_{\rm MIN}+\Delta t, \ldots, T_{\rm MAX}\right), \tag{4.51}$$

which has dimension $9 \times N_{\rm TIMES}$. As in the main text, we then trained our neural network on many examples of this compressed data until it can accurately classify whether any given data came from an interaction with a Fock state or a coherent state. We used exactly the same neural network architecture, loss function and optimization method. We show how to generate the different sample moments in Appendix A.5.2.

We considered an optical cavity of length $L = 1$ cm and a probe with a Gaussian smearing function of width $\sigma = 0.1$ mm connected to the center of the cavity, at $x = L/2 = 0.5$ cm. As discussed above, in each run of the experiment the probe strongly interacts with the cavity at two times: first at $t = T_{min} = 0$ then at $t = T_{min} + n\,\Delta t$ for $n = 1, 2, \ldots, N_{\rm TIMES}$ with $\Delta t = 6.67$ ps. As $N_{\rm TIMES} = 10$ then we have that $T_{max} = 66.7$ ps.

Fig 4.8b shows the validation accuracy of the neural network given different values for the probe's frequency, $\omega_{\rm D}$. All of the points are calculated with the same tomography, $N_{\rm TOM} = 5000$. This shows that the neural network can successfully distinguish between a Fock state and a phase-averaged coherent state given sample fourth moments. This plot also provides some physical insight. At resonance, i.e. when the probe frequency is the same as the frequency of the mode of interest (in Fig 4.8b, a solid vertical line corresponds to $\omega_{\rm D} = \omega_1 = \pi/L = 94.2$ GHz) we obtain an improvement in the accuracy of the neural network. Furthermore, a second peak at double the frequency of the first mode (in Fig 4.8b, the dashed vertical line in the figure, corresponding to $\omega_{\rm D} = 2\,\omega_1 = 188.4$ GHz). This is expected since for those values of the gap since resonant detectors are more sensitive to getting excited by capturing field excitations. We see the peaks in the accuracy occur at the first and second mode resonance of the detector gap. Moreover, it is noteworthy that the classification task appears to become easier with an increasing number of excitations, N, where PACs and Fock states become more and more distinguishable.

4.10 Conclusions

In this chapter, we proposed the use of machine learning techniques to process outcomes of local probes coupled to a quantum field as a context-free tool to learn about different features of the field.

As proof-of-principle, we studied a one-dimensional scalar field. We showed how using

the same measurement protocol on a single probe and the same type of neural network, one can learn about different features of the field, namely its boundary conditions (which is a non-local feature) and its temperature. Our results showed that the network could distinguish boundary conditions "without light", i.e. for the vacuum state of the field and before light has bounced off the boundaries. To obtain the effective speed of a signal in the lattice, and thus check how much the discretization of the field had affected the dispersion relation, we trained the network for a second classification problem. The neural network needed to distinguish between a field that had been perturbed at the boundary and a field that had not. We used the Hellinger distance to track the performance of the binary classification of boundary conditions and the binary classification for the signalling or not signalling field. We obtained that performance of the networks was inside the bounds provided for the optimal performance of any classification algorithm.

For the thermometry case, our results showed that the network could predict the temperature of the field before the detector thermalized with the field at temperatures relevant for semiconducting circuits, which is the setting that motivates our choice of parameters. Both the results we obtained were not entirely surprising: it is a well-known fact that fields store scrambled information about their features locally accessible in a large region of spacetime [100, 86, 78, 147, 70, 145]). The novelty of this result was the broad applicability of the tools. Usually, one has to adapt measurement protocols and analysis techniques to study different features of the field. By placing all the complexity on the neural network, the translation from probes to claims about the features of the fields becomes much easier.

Finally, we discussed a third case for which we did not discretize the field: distinguishing between a state in which for all modes the initial state is the vacuum and the first mode is either a Fock state with N excitations and a phase-averaged coherent state with N excitations on average. This allows us to clear any doubts about whether our results would work in the absence of UV cutoffs. Also, in this case, we did not have the Gaussian formalism to study the evolution of the system. Therefore, the problem becomes more complicated: the information obtained by the probe is no longer encoded solely in its first and second moments. Our results show that the network could differentiate the two states better when the number of excitations N was higher. Finally, we observed that at resonance, i.e. when the probe frequency and the frequency of the first mode coincided. We interpreted this result as an increased ability of the detector to detect field excitations when in resonance.

Finally, we discuss the broader implication of these results in Chapter 5.

Chapter 5

Conclusions and Outlook

5.1 Cancelling the harvesting of correlations

In Chapter 3 we studied how the presence of N interloper detectors affected the ability for two target detectors, controlled by Alice and Bob, to harvest correlations from a coherent state of a free scalar massless field. The action of coupling a single interloper detector to the field provoked the "flooding" of Bob's detector with entropy. Thus, any correlation harvesting protocol between Bob and any other detector coupled to the field would be sabotaged.

This result implies that we may be able to isolate a particular detector. For example, if we want Bob's detector to only "collect" properties of the field, we could use an interloper detector to prevent Bob from entangling to any other system. A setting in which this isolation would be useful is in the probing of gravitational waves. Since the detection of gravitational waves is so challenging, one would desire to isolate the detector's response from noise. Another extension in the area of general relativity would be to study this phenomenon in curved spacetimes.

We also observed that the presence of many interloper detectors exponentially suppressed the amount of correlation harvested by Alice and Bob. This result was very preliminary and depended heavily on the Dirac-delta coupling of our choice. This result could be extended by using more realistic coupling schemes. It would also be very interesting to consider correlated interloper detectors. Using realistic couplings and correlated detectors, we could obtain some insight into whether macroscopic detectors are able to harvest correlations. In particular, it would be interesting to study the ability of two conglomerations or "clouds" of detectors to harvest entanglement or correlations. Combining this study

with relativistic quantum optics [74], this project could be useful for trapped-ion settings or optical lattices. For example, the platform of trapped ions naturally provides coupling (and thus entanglement) between the ions due to the electromagnetic interactions between them. In fact, one of the technical challenges of this platform is actually "stopping" such entanglement, and it requires individual addressing of the ions with beams. If we could "kick" the electromagnetic field at the right moment, with the right strength, we may be able to break this natural entanglement between the ions.

All these previous ideas are long-term oriented. However, there are several short-term attainable continuations of this project. The first one would be to not use single delta-Dirac couplings for the detectors. As we discussed in Chapter 3, this type of interaction hinders the possibility of entanglement harvesting. Therefore, an extension of this work would be to consider that each detector couples twice to the field with delta-Dirac couplings. According to the no-go theorem [118] discussed in Chapter 3, this setting would allow for entanglement harvesting. Another positive aspect is that it may be possible to obtain analytic formulas for such coupling choices. Alternatively, one could obtain perturbative results for couplings of finite duration.

5.2 Machine learning QFT from local probes

In Chapter 4, we proposed the use of machine learning techniques to process outcomes of local probes coupled to a quantum field as a context-free tool to learn about different features of the field.

As proof-of-principle, we studied a toy model: we use one detector to probe a one-dimensional scalar field. We show how using the same measurement protocol on a single probe and the same type of neural network, one can learn about different features of the field, namely its boundary conditions (which is a non-local feature) and its temperature. Our results showed that the network could distinguish boundary conditions "without light", i.e. for the vacuum state of the field and before light has bounced off the boundaries. For the thermometry case, our results showed that the network could predict the temperature of the field before the detector thermalizes with the field.

Both the results we obtained were not entirely surprising: it is a well-known fact that fields store scrambled information about their features locally accessible in a large region of spacetime [100, 86, 78, 147, 70, 145]). The novelty of this result was the broad applicability of the statistical tools. The same type of network and a very similar measurement protocol was also useful to distinguish between a Fock state and an average-coherent state. Usually, one has to adapt measurement protocols and analysis techniques to study different features

of the field. By placing all the complexity on the neural network, the translation from probes to claims about the features of the fields becomes much easier.

This paves the way to the use of machine learning techniques in more complicated scenarios such as distinguishing gravitational backgrounds [95, 122], global state tomography [131] with local probes, acknowledging entanglement in analog Hawking radiation [125], and even new experimental proposals seeking direct evidence of untested QFT phenomena such as the Unruh effect [133]. Finally, the techniques developed here are directly translatable to their use in many-body quantum physics, where they can be used to address the problem of measuring many-body observables with local probes in, e.g., quantum phase transitions [143].

Finally, in relation to the results in Chapter 3, it would be interesting to combine machine learning techniques with correlation harvesting protocols. Some work has already been done in this direction. In [144], the authors found, analytically, that exploiting the correlation in the noise present in the field they could improve their harvesting protocol. Also, it was proposed in [6] that a CNN (convolutional neural network) would be able to exploit the noise correlations to better tolerate the noise present in data. The type of noise studied and generated in [6] could be understood as a simulation of quantum fluctuations of a Klein-Gordon field in two dimensions. It seems plausible then that by combining machine learning techniques and learning from the noise correlations, one would be able to improve the harvesting protocols. Also, machine learning could be useful in the quest of entangling macroscopic detectors, made out of 'clouds" of correlated microscopic detectors. In principle, the presence of many microscopic detectors could be very noisy. Maybe by using machine learning, we could exploit the correlations in the noise to achieve the task of harvesting correlations from a field using macroscopic detectors.

References

[1] G. Aad, T. Abajyan, B. Abbott, J. Abdallah, S. Abdel Khalek, A.A. Abdelalim, O. Abdinov, R. Aben, B. Abi, M. Abolins, and et al. Observation of a new particle in the search for the standard model higgs boson with the atlas detector at the lhc. *Physics Letters B*, 716(1):1–29, Sep 2012.

[2] Gerardo Adesso. Entanglement of gaussian states, 2007.

[3] Gerardo Adesso, Thomas R Bromley, and Marco Cianciaruso. Measures and applications of quantum correlations. *Journal of Physics A: Mathematical and Theoretical*, 49(47):473001, 2016.

[4] Aida Ahmadzadegan, Fatemeh Lalegani, Achim Kempf, and Robert B. Mann. Probing geometric information using the unruh effect in the vacuum. *Phys. Rev. D*, 100:085013, Oct 2019.

[5] Aida Ahmadzadegan, Eduardo Martín-Martínez, and Robert B. Mann. Cavities in curved spacetimes: The response of particle detectors. *Phys. Rev. D*, 89:024013, Jan 2014.

[6] Aida Ahmadzadegan, Petar Simidzija, Ming Li, and Achim Kempf. Learning to utilize correlated auxiliary classical or quantum noise, 2020.

[7] Álvaro M. Alhambra, Achim Kempf, and Eduardo Martín-Martínez. Casimir forces on atoms in optical cavities. *Physical Review A*, 89(3), Mar 2014.

[8] Mazhar Ali, A. Rau, and G. Alber. Erratum: Quantum discord for two-qubit x states [phys. rev. a 81, 042105 (2010)]. *Phys. Rev. A*, 82, 12 2010.

[9] Mazhar Ali, ARP Rau, and Gernot Alber. Quantum discord for two-qubit x states. *Physical Review A*, 81(4):042105, 2010.

[10] M.H. Anderson, J.R. Ensher, M.R. Matthews, C.E. Wieman, and E.A. Cornell. Observation of Bose-Einstein condensation in a dilute atomic vapor. *Science*, 269:198–201, 1995.

[11] Markus Ansmann, H Wang, Radoslaw C Bialczak, Max Hofheinz, Erik Lucero, M Neeley, AD O'Connell, D Sank, M Weides, J Wenner, AN Cleland, and John M Martinis. Violation of bell's inequality in josephson phase qubits. *Nature*, 461(7263):504—506, September 2009.

[12] Frank Arute, Kunal Arya, Ryan Babbush, Dave Bacon, Joseph C. Bardin, Rami Barends, Rupak Biswas, Sergio Boixo, Fernando G. S. L. Brandao, David A. Buell, Brian Burkett, Yu Chen, Zijun Chen, Ben Chiaro, Roberto Collins, William Courtney, Andrew Dunsworth, Edward Farhi, Brooks Foxen, Austin Fowler, Craig Gidney, Marissa Giustina, Rob Graff, Keith Guerin, Steve Habegger, Matthew P. Harrigan, Michael J. Hartmann, Alan Ho, Markus Hoffmann, Trent Huang, Travis S. Humble, Sergei V. Isakov, Evan Jeffrey, Zhang Jiang, Dvir Kafri, Kostyantyn Kechedzhi, Julian Kelly, Paul V. Klimov, Sergey Knysh, Alexander Korotkov, Fedor Kostritsa, David Landhuis, Mike Lindmark, Erik Lucero, Dmitry Lyakh, Salvatore Mandrà, Jarrod R. McClean, Matthew McEwen, Anthony Megrant, Xiao Mi, Kristel Michielsen, Masoud Mohseni, Josh Mutus, Ofer Naaman, Matthew Neeley, Charles Neill, Murphy Yuezhen Niu, Eric Ostby, Andre Petukhov, John C. Platt, Chris Quintana, Eleanor G. Rieffel, Pedram Roushan, Nicholas C. Rubin, Daniel Sank, Kevin J. Satzinger, Vadim Smelyanskiy, Kevin J. Sung, Matthew D. Trevithick, Amit Vainsencher, Benjamin Villalonga, Theodore White, Z. Jamie Yao, Ping Yeh, Adam Zalcman, Hartmut Neven, and John M. Martinis. Quantum supremacy using a programmable superconducting processor. *Nature*, 574(7779):505–510, Oct 2019.

[13] Neil Ashby. Relativity in the global positioning system. *Living Reviews in Relativity*, 6(1):1, Jan 2003.

[14] Alain Aspect, Jean Dalibard, and Gérard Roger. Experimental test of bell's inequalities using time-varying analyzers. *Phys. Rev. Lett.*, 49:1804–1807, Dec 1982.

[15] Alain Aspect, Philippe Grangier, and Gérard Roger. Experimental tests of realistic local theories via bell's theorem. *Phys. Rev. Lett.*, 47:460–463, Aug 1981.

[16] Alain Aspect, Philippe Grangier, and Gérard Roger. Experimental realization of einstein-podolsky-rosen-bohm gedankenexperiment: A new violation of bell's inequalities. *Phys. Rev. Lett.*, 49:91–94, Jul 1982.

[17] Jacob D. Bekenstein. Black holes and entropy. *Phys. Rev. D*, 7:2333–2346, Apr 1973.

[18] Dionigi M T Benincasa, Leron Borsten, Michel Buck, and Fay Dowker. Quantum information processing and relativistic quantum fields. *Class. Quantum Gravity*, 31(7):075007, mar 2014.

[19] C. H. Bennett and G. Brassard. Quantum cryptography: Public key distribution and coin tossing. In *Proceedings of IEEE International Conference on Computers, Systems, and Signal Processing*, page 175, India, 1984.

[20] A. Bhattacharyya. On a measure of divergence between two multinomial populations. *Sankhya*, 7(4):401–406, 1946.

[21] B.H. Bransden, C.J. Joachain, and T.J. Plivier. *Physics of Atoms and Molecules*. Pearson Education. Prentice Hall, 2003.

[22] Eric G. Brown. Thermal amplification of field-correlation harvesting. *Phys. Rev. A*, 88:062336, Dec 2013.

[23] Eric G Brown, William Donnelly, Achim Kempf, Robert B Mann, Eduardo Martín-Martínez, and Nicolas C Menicucci. Quantum seismology. *New Journal of Physics*, 16(10):105020, oct 2014.

[24] Eric G. Brown, Eduardo Martín-Martínez, Nicolas C. Menicucci, and Robert B. Mann. Detectors for probing relativistic quantum physics beyond perturbation theory. *Phys. Rev. D*, 87:084062, Apr 2013.

[25] C. R. Cabrera, L. Tanzi, J. Sanz, B. Naylor, P. Thomas, P. Cheiney, and L. Tarruell. Quantum liquid droplets in a mixture of bose-einstein condensates. *Science*, 359(6373):301–304, 2018.

[26] Juan Carrasquilla and Roger G Melko. Machine learning phases of matter. *Nat. Phys.*, 13:431, feb 2017.

[27] Qing Chen, Chengjie Zhang, Sixia Yu, X. X. Yi, and C. H. Oh. Quantum discord of two-qubitxstates. *Physical Review A*, 84(4), Oct 2011.

[28] W. G. Cochran. The distribution of quadratic forms in a normal system, with applications to the analysis of covariance. *Mathematical Proceedings of the Cambridge Philosophical Society*, 30(2):178–191, 1934.

[29] Roger Colbeck and Renato Renner. No extension of quantum theory can have improved predictive power. *Nature Communications*, 2(1), Aug 2011.

[30] A. Decelle, V. Martin-Mayor, and B. Seoane. Learning a local symmetry with neural networks. *Phys. Rev. E*, 100:050102, Nov 2019.

[31] B. DeWitt. General Relativity: an Einstein Centenary Survey. In Hawking, S. and Israel, W., editor, *General Relativity: an Einstein Centenary Survey*. Cambridge University Press, Cambridge, 1979.

[32] Persi Diaconis, Susan Holmes, and Richard Montgomery. Dynamical bias in the coin toss. *SIAM Review*, 49(2):211–235, 2007.

[33] D. H. Douglass and R. Meservey. Energy gap measurements by tunneling between superconducting films. i. temperature dependence. *Phys. Rev.*, 135:A19–A23, Jul 1964.

[34] Fay Dowker. Useless qubits in "relativistic quantum information". 2011.

[35] F. J. Dyson. The radiation theories of tomonaga, schwinger, and feynman. *Phys. Rev.*, 75:486–502, Feb 1949.

[36] Paul Ehrenfest. Welche züge der lichtquantenhypothese spielen in der theorie der wärmestrahlung eine wesentliche rolle? *Annalen der Physik*, 341(11):91–118, 1911.

[37] A. Einstein. Über einen die Erzeugung und Verwandlung des Lichtes betreffenden heuristischen Gesichtspunkt. *Annalen der Physik*, 322(6):132–148, January 1905.

[38] A. Einstein, M. Born, H. Born, and I. Born. *The Born-Einstein Letters: Correspondence Between Albert Einstein and Max and Hedwig Born from 1916-1955, with Commentaries by Max Born*. Macmillan, 1971.

[39] A. Einstein, B. Podolsky, and N. Rosen. Can quantum-mechanical description of physical reality be considered complete? *Phys. Rev.*, 47:777–780, May 1935.

[40] Christopher J. Fewster and Rainer Verch. Quantum fields and local measurements, 2018.

[41] R. A. Fisher. On the Mathematical Foundations of Theoretical Statistics. *Philos. Trans. Royal Soc. A*, 222:309–368, 1922.

[42] P Forn-Díaz, J. J. García-Ripoll, B Peropadre, J.-L. Orgiazzi, M. A. Yurtalan, R Belyansky, C. M. Wilson, and A Lupascu. Ultrastrong coupling of a single artificial atom to an electromagnetic continuum in the nonperturbative regime. *Nat. Phys.*, 13:39, oct 2016.

[43] Nicolai Friis, Marcus Huber, Ivette Fuentes, and David Edward Bruschi. Quantum gates and multipartite entanglement resonances realized by nonuniform cavity motion. *Phys. Rev. D*, 86:105003, Nov 2012.

[44] F. Galve, G. L. Giorgi, and R. Zambrini. Orthogonal measurements are almost sufficient for quantum discord of two qubits. *EPL (Europhysics Letters)*, 96(4):40005, nov 2011.

[45] Christof Gattringer and Christian B. Lang. Quantum chromodynamics on the lattice. *Lect. Notes Phys.*, 788:1–343, 2010.

[46] Walther Gerlach and Otto Stern. Der experimentelle Nachweis der Richtungsquantelung im Magnetfeld. *Zeitschrift fur Physik*, 9(1):349–352, December 1922.

[47] Davide Girolami and Gerardo Adesso. Quantum discord for general two-qubit states: Analytical progress. *Physical Review A*, 83(5), May 2011.

[48] Ian Goodfellow, Yoshua Bengio, and Aaron Courville. *Deep Learning*. MIT Press, Cambridge, US, 2016. http://www.deeplearningbook.org.

[49] Christopher E Granade, Christopher Ferrie, Nathan Wiebe, and D G Cory. Robust online hamiltonian learning. *New J. Phys*, 14(10):103013, oct 2012.

[50] Daniel Grimmer, Eric Brown, Achim Kempf, Robert B Mann, and Eduardo Martín-Martínez. A classification of open gaussian dynamics. *Journal of Physics A: Mathematical and Theoretical*, 51(24):245301, May 2018.

[51] Daniel Grimmer, Irene Melgarejo-Lermas, and Eduardo Martin-Martinez. Machine learning quantum field theory with local probes, 2019.

[52] Daniel Grimmer, Irene Melgarejo-Lermas, and Eduardo Martín-Martínez. https://github.com/BarrioRQI/MachineLearningQFT, 2019.

[53] S. Hamieh, R. Kobes, and H. Zaraket. Positive-operator-valued measure optimization of classical correlations. *Phys. Rev. A*, 70:052325, Nov 2004.

[54] S. W. Hawking. Gravitational radiation from colliding black holes. *Phys. Rev. Lett.*, 26:1344–1346, May 1971.

[55] G. C. Hegerfeldt. Causality, particle localization and positivity of the energy. *Lecture Notes in Physics*, page 238–245.

[56] Leah Henderson and Vlatko Vedral. Classical, quantum and total correlations. *Journal of physics A: mathematical and general*, 34(35):6899, 2001.

[57] Alexander Hentschel and Barry C. Sanders. Efficient algorithm for optimizing adaptive quantum metrology processes. *Phys. Rev. Lett.*, 107:233601, Nov 2011.

[58] Lee Hodgkinson and Jorma Louko. Static, stationary, and inertial unruh-dewitt detectors on the btz black hole. *Phys. Rev. D*, 86:064031, Sep 2012.

[59] Masahiro Hotta. Quantum measurement information as a key to energy extraction from local vacuums. *Physical Review D*, 78(4), Aug 2008.

[60] Masahiro Hotta and Koji Yamaguchi. Strong Chaos of Fast Scrambling Yields Order: Emergence of Decoupled Quantum Information Capsules. *arXiv e-prints*, page arXiv:1906.04990, Jun 2019.

[61] J.-T. Hsiang and B. L. Hu. Distance and coupling dependence of entanglement in the presence of a quantum field. *Phys. Rev. D*, 92:125026, Dec 2015.

[62] B. L. Hu and A. Matacz. Quantum brownian motion in a bath of parametric oscillators: A model for system-field interactions. *Phys. Rev. D*, 49:6612–6635, Jun 1994.

[63] R.L. Hudson. When is the wigner quasi-probability density non-negative? *Reports on Mathematical Physics*, 6(2):249 – 252, 1974.

[64] Robert H. Jonsson, Eduardo Martín-Martínez, and Achim Kempf. Information transmission without energy exchange. *Physical Review Letters*, 114(11), Mar 2015.

[65] P.L. KNIGHT and L. ALLEN. Chapter 3 - absorption and emission of radiation. In P.L. KNIGHT and L. ALLEN, editors, *Concepts of Quantum Optics*, pages 27 – 43. Pergamon, 1983.

[66] Jun-ichirou Koga, Gen Kimura, and Kengo Maeda. Quantum teleportation in vacuum using only unruh-dewitt detectors. *Physical Review A*, 97(6), Jun 2018.

[67] John B. Kogut. An introduction to lattice gauge theory and spin systems. *Rev. Mod. Phys.*, 51:659–713, Oct 1979.

[68] Shingo Kukita and Yasusada Nambu. Harvesting large scale entanglement in de sitter space with multiple detectors. *Entropy*, 19(9):449, Aug 2017.

[69] T. D. Ladd, F. Jelezko, R. Laflamme, Y. Nakamura, C. Monroe, and J. L. O'Brien. Quantum computers. *Nature*, 464(7285):45–53, Mar 2010.

[70] K A Landsman, C Figgatt, T Schuster, N M Linke, B Yoshida, N Y Yao, and C Monroe. Verified quantum information scrambling. *Nature*, 567(7746):61–65, 2019.

[71] Georges Lemaître. Cosmological application of relativity. *Rev. Mod. Phys.*, 21:357–366, Jul 1949.

[72] Ulf Leonhardt. *Essential Quantum Optics: From Quantum Measurements to Black Holes*. Cambridge University Press, 2010.

[73] Shih-Yuin Lin and B. L. Hu. Backreaction and the unruh effect: New insights from exact solutions of uniformly accelerated detectors. *Phys. Rev. D*, 76:064008, Sep 2007.

[74] Richard Lopp and Eduardo Martín-Martínez. Light, matter, and quantum randomness generation: A relativistic quantum information perspective. *Optics Communications*, 423:29–47, Sep 2018.

[75] Krzysztof Lorek, Daniel Pecak, Eric G. Brown, and Andrzej Dragan. Extraction of genuine tripartite entanglement from the vacuum. *Phys. Rev. A*, 90:032316, Sep 2014.

[76] Xiao-Ming Lu, Jian Ma, Zhengjun Xi, and Xiaoguang Wang. Optimal measurements to access classical correlations of two-qubit states. *Physical Review A*, 83(1), Jan 2011.

[77] E. Lubkin. Entropy of an n-system from its correlation with a k-reservoir. *Journal of Mathematical Physics*, 19:1028–1031, May 1978.

[78] Juan Maldacena, Stephen H. Shenker, and Douglas Stanford. A bound on chaos. *J. High Energy Phys.*, 2016(8):106, Aug 2016.

[79] R B Mann and T C Ralph. Relativistic quantum information. *Classical and Quantum Gravity*, 29(22):220301, oct 2012.

[80] Eduardo Martín-Martínez. Causality issues of particle detector models in qft and quantum optics. *Phys. Rev. D*, 92:104019, Nov 2015.

[81] Eduardo Martín-Martínez, Eric G. Brown, William Donnelly, and Achim Kempf. Sustainable entanglement production from a quantum field. *Phys. Rev. A*, 88:052310, Nov 2013.

[82] Eduardo Martín-Martínez, Ivette Fuentes, and Robert B. Mann. Using berry's phase to detect the unruh effect at lower accelerations. *Phys. Rev. Lett.*, 107:131301, Sep 2011.

[83] Eduardo Martín-Martínez, Miguel Montero, and Marco del Rey. Wavepacket detection with the unruh-dewitt model. *Physical Review D*, 87(6), Mar 2013.

[84] Eduardo Martín-Martínez, T. Rick Perche, and Bruno de S. L. Torres. General relativistic quantum optics: Finite-size particle detector models in curved spacetimes. *Phys. Rev. D*, 101:045017, Feb 2020.

[85] Eduardo Martín-Martínez and Pablo Rodriguez-Lopez. Relativistic quantum optics: The relativistic invariance of the light-matter interaction models. *Phys. Rev. D*, 97:105026, May 2018.

[86] Eduardo Martín-Martínez, Alexander R. H. Smith, and Daniel R. Terno. Spacetime structure and vacuum entanglement. *Phys. Rev. D*, 93:044001, Feb 2016.

[87] Eduardo Martín-Martínez. Causality issues of particle detector models in qft and quantum optics. *Physical Review D*, 92(10), Nov 2015.

[88] Eduardo Martín-Martínez, T. Rick Perche, and Bruno de S. L. Torres. Broken covariance of particle detector models in relativistic quantum information, 2020.

[89] Serge Massar and Philippe Spindel. Einstein-podolsky-rosen correlations between two uniformly accelerated oscillators. *Phys. Rev. D*, 74:085031, Oct 2006.

[90] J. Maziero, L. C. Celeri, and R. M. Serra. Symmetry aspects of quantum discord. 2010.

[91] Emma McKay, Adrian Lupascu, and Eduardo Martín-Martínez. Finite sizes and smooth cutoffs in superconducting circuits. *Phys. Rev. A*, 96:052325, Nov 2017.

[92] Kavan Modi, Aharon Brodutch, Hugo Cable, Tomasz Paterek, and Vlatko Vedral. The classical-quantum boundary for correlations: discord and related measures. 2012.

[93] Yuto Mori, Kouji Kashiwa, and Akira Ohnishi. Application of a neural network to the sign problem via the path optimization method. *Prog. Theor. Exp. Phys.*, 2018(2), 02 2018.

[94] Amos Nathan. On sampling a function and its derivatives. *Information and Control*, 22(2):172 – 182, 1973.

[95] Keith K. Ng, Robert B. Mann, and Eduardo Martín-Martínez. Equivalence principle and qft: Can a particle detector tell if we live inside a hollow shell? *Phys. Rev. D*, 94:104041, Nov 2016.

[96] Keith K. Ng, Robert B. Mann, and Eduardo Martín-Martínez. Over the horizon: Distinguishing the schwarzschild spacetime and the $\mathbb{RP}^3$ spacetime using an unruh-dewitt detector. *Phys. Rev. D*, 96:085004, Oct 2017.

[97] Michael A Nielsen and Isaac L Chuang. *Quantum information and quantum computation*, volume 2. 2000.

[98] Harold Ollivier and Wojciech H Zurek. Quantum discord: a measure of the quantumness of correlations. *Physical review letters*, 88(1):017901, 2001.

[99] Alvaro Ortega, Emma McKay, Álvaro M. Alhambra, and Eduardo Martín-Martínez. Work distributions on quantum fields. *Phys. Rev. Lett.*, 122:240604, Jun 2019.

[100] Don N. Page. Information in black hole radiation. *Phys. Rev. Lett.*, 71:3743–3746, Dec 1993.

[101] Maria Papageorgiou and Jason Pye. Impact of relativity on particle localizability and ground state entanglement. *Journal of Physics A: Mathematical and Theoretical*, 52(37):375304, Aug 2019.

[102] Daniel P. Petersen and David Middleton. Sampling and reconstruction of wave-number-limited functions in n-dimensional euclidean spaces. *Information and Control*, 5(4):279 – 323, 1962.

[103] Max Planck. Ueber das gesetz der energieverteilung im normalspectrum. *Annalen der Physik*, 309(3):553–563, 1901.

[104] Alejandro Pozas-Kerstjens and Eduardo Martín-Martínez. Harvesting correlations from the quantum vacuum. *Phys. Rev. D*, 92:064042, Sep 2015.

[105] Alejandro Pozas-Kerstjens and Eduardo Martín-Martínez. Entanglement harvesting from the electromagnetic vacuum with hydrogenlike atoms. *Phys. Rev. D*, 94:064074, Sep 2016.

[106] Jason Pye, William Donnelly, and Achim Kempf. Locality and entanglement in bandlimited quantum field theory. *Physical Review D*, 92(10), Nov 2015.

[107] Yihui Quek, Stanislav Fort, and Hui Khoon Ng. Adaptive Quantum State Tomography with Neural Networks. *arXiv e-prints*, page arXiv:1812.06693, Dec 2018.

[108] Michael Redhead. More ado about nothing. *Foundations of Physics*, 25(1):123–137, Jan 1995.

[109] Benni Reznik. Entanglement from the vacuum. *Foundations of Physics*, 33(1):167–176, 2003.

[110] Benni Reznik, Alex Retzker, and Jonathan Silman. Violating bell's inequalities in vacuum. *Phys. Rev. A*, 71:042104, Apr 2005.

[111] Allison Sachs, Robert B. Mann, and Eduardo Martín-Martínez. Entanglement harvesting and divergences in quadratic unruh-dewitt detector pairs. *Phys. Rev. D*, 96:085012, Oct 2017.

[112] Grant Salton, Robert B Mann, and Nicolas C Menicucci. Acceleration-assisted entanglement harvesting and rangefinding. *New Journal of Physics*, 17(3):035001, mar 2015.

[113] Bonny L. Schumaker. Quantum mechanical pure states with gaussian wave functions. *Phys. Rep.*, 135(6):317 – 408, 1986.

[114] Marlan O. Scully and M. Suhail Zubairy. *Quantum Optics*. Cambridge University Press, 1997.

[115] Phiala E. Shanahan, Daniel Trewartha, and William Detmold. Machine learning action parameters in lattice quantum chromodynamics. *Phys. Rev. D*, 97:094506, May 2018.

[116] Peter W. Shor. Polynomial-time algorithms for prime factorization and discrete logarithms on a quantum computer. *SIAM Journal on Computing*, 26(5):1484–1509, Oct 1997.

[117] Shabnam Siddiqui and Chandralekha Singh. How diverse are physics instructors' attitudes and approaches to teaching undergraduate level quantum mechanics? *European Journal of Physics*, 38(3):035703, mar 2017.

[118] Petar Simidzija, Robert H. Jonsson, and Eduardo Martín-Martínez. General no-go theorem for entanglement extraction. *Physical Review D*, 97(12), Jun 2018.

[119] Petar Simidzija and Eduardo Martín-Martíne. Nonperturbative analysis of entanglement harvesting from coherent field states. *Physical Review D*, 96(6), Sep 2017.

[120] Petar Simidzija and Eduardo Martín-Martínez. All coherent field states entangle equally. *Physical Review D*, 96(2), Jul 2017.

[121] Petar Simidzija and Eduardo Martín-Martínez. Harvesting correlations from thermal and squeezed coherent states. *Phys. Rev. D*, 98:085007, Oct 2018.

[122] Alexander R H Smith and Robert B Mann. Looking inside a black hole. *Class. Quantum Gravity*, 31(8):082001, apr 2014.

[123] Rafael D. Sorkin. Impossible measurements on quantum fields. 1993.

[124] Greg Ver Steeg and Nicolas C. Menicucci. Entangling power of an expanding universe. *Phys. Rev. D*, 79:044027, Feb 2009.

[125] Jeff Steinhauer. Observation of quantum Hawking radiation and its entanglement in an analogue black hole. *Nat. Phys.*, 12:959, aug 2016.

[126] Nadine Stritzelberger, Laura J. Henderson, Valentina Baccetti, Nicolas C. Menicucci, and Achim Kempf. Entanglement harvesting with coherently delocalized matter, 2020.

[127] Stephen J. Summers and Reinhard Werner. The vacuum violates bell's inequalities. *Physics Letters A*, 110(5):257 – 259, 1985.

[128] Stephen J. Summers and Reinhard Werner. Bell's inequalities and quantum field theory. i. general setting. *Journal of Mathematical Physics*, 28(10):2440–2447, 1987.

[129] Shin Takagi. Vacuum Noise and Stress Induced by Uniform Acceleration: Hawking-Unruh Effect in Rindler Manifold of Arbitrary Dimension. *Prog. Theor. Phys. Supp.*, 88:1–142, 03 1986.

[130] E. S. Tiunov, V. V. Tiunova, A. E. Ulanov, A. I. Lvovsky, and A. K. Fedorov. Experimental quantum homodyne tomography via machine learning. *arXiv e-prints*, page arXiv:1907.06589, Jul 2019.

[131] Giacomo Torlai, Guglielmo Mazzola, Juan Carrasquilla, Matthias Troyer, Roger Melko, and Giuseppe Carleo. Neural-network quantum state tomography. *Nat. Phys.*, 14(5):447–450, 2018.

[132] Jose Trevison, Koji Yamaguchi, and Masahiro Hotta. Pure state entanglement harvesting in quantum field theory. *Progress of Theoretical and Experimental Physics*, 2018(10), Oct 2018.

[133] W. G. Unruh. Notes on black-hole evaporation. *Phys. Rev. D*, 14:870–892, Aug 1976.

[134] W. G. Unruh. Particle detectors and black holes. In *1st Marcel Grossmann Meeting on General Relativity*, volume 1, pages 527–536, January 1977.

[135] W. G. Unruh and W. H. Zurek. Reduction of a wave packet in quantum brownian motion. *Phys. Rev. D*, 40:1071–1094, Aug 1989.

[136] William G. Unruh and Robert M. Wald. What happens when an accelerating observer detects a rindler particle. *Phys. Rev. D*, 29:1047–1056, Mar 1984.

[137] Antony Valentini. Non-local correlations in quantum electrodynamics. *Physics Letters A*, 153(6):321 – 325, 1991.

[138] V. Vedral. Classical correlations and entanglement in quantum measurements. *Phys. Rev. Lett.*, 90:050401, Feb 2003.

[139] G. Vidal, J. I. Latorre, E. Rico, and A. Kitaev. Entanglement in quantum critical phenomena. *Physical Review Letters*, 90(22), Jun 2003.

[140] A Wallraff, D I Schuster, A Blais, L Frunzio, R.-S Huang, J Majer, S Kumar, S M Girvin, and R J Schoelkopf. Strong coupling of a single photon to a superconducting qubit using circuit quantum electrodynamics. *Nature*, 431(7005):162–167, 2004.

[141] Christian Weedbrook, Stefano Pirandola, Raúl García-Patrón, Nicolas J. Cerf, Timothy C. Ralph, Jeffrey H. Shapiro, and Seth Lloyd. Gaussian quantum information. *Rev. Mod. Phys.*, 84:621–669, May 2012.

[142] Steven Weinberg. *The Quantum Theory of Fields*, volume 1. Cambridge University Press, 1995.

[143] Zhenyu Xu and Adolfo del Campo. Probing the full distribution of many-body observables by single-qubit interferometry. *Phys. Rev. Lett.*, 122:160602, Apr 2019.

[144] Koji Yamaguchi, Aida Ahmadzadegan, Petar Simidzija, Achim Kempf, and Eduardo Martín-Martínez. Superadditivity of channel capacity through quantum fields. *Physical Review D*, 101(10), May 2020.

[145] Koji Yamaguchi, Naoki Watamura, and Masahiro Hotta. Quantum information capsule and information delocalization by entanglement in multiple-qubit systems. *Phys. Lett. A*, 383(12):1255 – 1259, 2019.

[146] Juan Yin, Yuan Cao, Yu-Huai Li, Sheng-Kai Liao, Liang Zhang, Ji-Gang Ren, Wen-Qi Cai, Wei-Yue Liu, Bo Li, Hui Dai, Guang-Bing Li, Qi-Ming Lu, Yun-Hong Gong, Yu Xu, Shuang-Lin Li, Feng-Zhi Li, Ya-Yun Yin, Zi-Qing Jiang, Ming Li, Jian-Jun Jia, Ge Ren, Dong He, Yi-Lin Zhou, Xiao-Xiang Zhang, Na Wang, Xiang Chang, Zhen-Cai Zhu, Nai-Le Liu, Yu-Ao Chen, Chao-Yang Lu, Rong Shu, Cheng-Zhi Peng, Jian-Yu Wang, and Jian-Wei Pan. Satellite-based entanglement distribution over 1200 kilometers. *Science*, 356(6343):1140–1144, 2017.

[147] Beni Yoshida and Alexei Kitaev. Efficient decoding for the Hayden-Preskill protocol, 2017.

[148] Kai Zhou, Gergely Endrődi, Long-Gang Pang, and Horst Stöcker. Regressive and generative neural networks for scalar field theory. *Phys. Rev. D*, 100:011501, Jul 2019.

APPENDICES

Appendix A

Non-perturbative calculations for correlation cancellation

A.1 Calculating non-perturbative time evolution unitary

Starting from equation (3.5) and using the time switching functions $\chi_\nu(t) = \eta_\nu \delta(t - t_\nu)$ we have

$$\begin{aligned}
\hat{U} &= \mathcal{T} \exp\left[-\mathrm{i}\int_{-\infty}^{\infty} \mathrm{d}t \hat{H}(t)\right] = \mathcal{T} \exp\left[-\mathrm{i}\sum_{\nu=1}^{N} \hat{H}_\nu\right] \\
&= \sum_{n=0}^{\infty} \frac{1}{n!} \sum_{m_i, \sum m_i = n} \frac{n!}{m_1! m_2! \dots m_N!} (-\mathrm{i}\hat{H}_N)^{m_N} (-\mathrm{i}\hat{H}_{N-1})^{m_{N-1}} \dots (-\mathrm{i}\hat{H}_1)^{m_1} \\
&= \Big(\sum_{m_N=0}^{\infty} \frac{1}{m_N!} (-\mathrm{i}\hat{H}_N)^{m_N})\Big)\Big(\sum_{m_{N-1}=0}^{\infty} \frac{1}{m_{N-1}!} (-\mathrm{i}\hat{H}_{N-1})^{m_{N-1}})\Big) \dots \Big(\sum_{m_1=0}^{\infty} \frac{1}{m_1!} (-\mathrm{i}\hat{H}_1)^{m_1})\Big) \\
&= \hat{U}_N \hat{U}_{N-1} \dots \hat{U}_1,
\end{aligned} \tag{A.1}$$

where $\hat{H}_\nu = \lambda_\nu \hat{\mu}_\nu(t_\nu) \otimes \int \mathrm{d}^n \boldsymbol{x} F_\nu(\boldsymbol{x} - \boldsymbol{x}_\nu) \hat{\phi}(t_\nu, \boldsymbol{x})$. Also we have defined $\hat{U}_\nu = \exp\Big[-\mathrm{i}\hat{H}_\nu\Big]$.

Note that, to write the second line, we have assumed that $t_1 \leq t_2 \leq \dots \leq t_N$, to perform the time ordering. Plugging in the expression of the field from Eq. (2.6) we get

$$\hat{H}_\nu = \lambda_\nu \hat{\mu}_\nu(t_\nu) \otimes \int \mathrm{d}^n \boldsymbol{x} F_\nu(\boldsymbol{x} - \boldsymbol{x}_\nu) \int \mathrm{d}^n \boldsymbol{k} \frac{1}{\sqrt{2(2\pi)^n |\boldsymbol{k}|}} \Big[\hat{a}^\dagger_{\boldsymbol{k}} e^{\mathrm{i}(|\boldsymbol{k}| t_\nu - \boldsymbol{k}\cdot\boldsymbol{x})} + \hat{a}_{\boldsymbol{k}} e^{-\mathrm{i}(|\boldsymbol{k}| t_\nu - \boldsymbol{k}\cdot\boldsymbol{x})} \Big]. \tag{A.2}$$

Using the Fourier transformation of $F_\nu(\boldsymbol{x}-\boldsymbol{x}_\nu)$ from (3.17), we can perform the integration over $\boldsymbol{x}$ in the above expression to obtain

$$\hat{H}_\nu = \lambda_\nu \hat{\mu}_\nu(t_\nu) \otimes \int \mathrm{d}^n \boldsymbol{k} \frac{1}{\sqrt{2|\boldsymbol{k}|}} \Big[\tilde{F}_\nu(-\boldsymbol{k}) \hat{a}^\dagger_{\boldsymbol{k}} e^{\mathrm{i}(|\boldsymbol{k}| t_\nu - \boldsymbol{k}\cdot\boldsymbol{x}_\nu)} + \tilde{F}_\nu(\boldsymbol{k}) \hat{a}_{\boldsymbol{k}} e^{-\mathrm{i}(|\boldsymbol{k}| t_\nu - \boldsymbol{k}\cdot\boldsymbol{x}_\nu)} \Big]. \tag{A.3}$$

Using $\beta_\nu(\boldsymbol{k})$ from equation (3.16), we may now rewrite $\hat{U}_\nu$ as

$$\hat{U}_\nu = \exp\left[\hat{\mu}_\nu \otimes \int \mathrm{d}^n \boldsymbol{k} \big[\beta_\nu(\boldsymbol{k}) \hat{a}^\dagger_{\boldsymbol{k}} - \beta_\nu(\boldsymbol{k})^* \hat{a}_{\boldsymbol{k}} \big] \right]. \tag{A.4}$$

Observe that $\hat{\mu}_\nu^2 = \mathbb{1}$. Keeping this in mind, we may expand the exponential in $\hat{U}_\nu$ to obtain

$$\hat{U}_\nu = \frac{1 + \hat{\mu}_\nu}{2} \otimes \hat{D}_{\beta_\nu(\boldsymbol{k})} + \frac{1 - \hat{\mu}_\nu}{2} \otimes \hat{D}_{-\beta_\nu(\boldsymbol{k})}. \tag{A.5}$$

In the $\{|s_\nu\rangle\}$ basis, as given in (3.11), it is easy to see that

$$\begin{aligned} \hat{m}_\nu(t_\nu) &= |1_\nu\rangle\langle 1_\nu| - |-1_\nu\rangle\langle -1_\nu| = \hat{S}^\nu_3, \\ \hat{\mu}_\nu(t_\nu) &= \mathbb{1}_1 \otimes \cdots \otimes \mathbb{1}_{\nu-1} \otimes \hat{S}^\nu_3 \otimes \ldots \mathbb{1}_N. \end{aligned} \tag{A.6}$$

Using this in the expression for $\hat{U}_\nu$ we obtain equation (3.13)

$$\hat{U}_\nu = \sum_{s_\nu} \hat{P}_{s_\nu} \otimes \hat{D}_{s_\nu \beta_\nu(\boldsymbol{k})} \quad s_\nu = -1, 1. \tag{A.7}$$

Here, $\hat{P}_{s_\nu} = \mathbb{1}_1 \otimes \cdots \otimes \mathbb{1}_{\nu-1} \otimes |s_\nu\rangle\langle s_\nu| \otimes \ldots \mathbb{1}_N$ is the projector on to the $|s_\nu\rangle$ subspace.

The unitary operator for the entire interaction $\hat{U}_\nu$ is thus a product of the individual

unitaries $\hat{U}_\nu$ as obtained in equation (3.12). It can be further written as

$$\hat{U} = \hat{U}_N \hat{U}_{N-1} \dots \hat{U}_1 = \sum_{\{s_1, s_2, \dots s_N\}} \hat{P}_{s_N} \dots \hat{P}_{s_1} \otimes \hat{D}_{s_N \beta_N(\boldsymbol{k})} \dots \hat{D}_{s_1 \beta_1(\boldsymbol{k})}. \tag{A.8}$$

The summation is over all the possible N-tuples $\{s_1, s_2, \dots, s_N\}$, where each s_ν takes the value 1 or -1. In equation (2.12), we obtain an expression for the product of two displacement operators. Using it repeatedly, we can obtain the product of N displacement operators,

$$\hat{D}_{s_N \beta_N(\boldsymbol{k})} \dots \hat{D}_{s_1 \beta_1(\boldsymbol{k})} = \hat{D}_{s_N \beta_N(\boldsymbol{k}) + \dots + s_1 \beta_1(\boldsymbol{k})} \exp\left[\mathrm{i}\, \mathrm{Im} \sum_{j \geq i} s_j s_i T_{ij} \right], \tag{A.9}$$

where

$$T_{ij} = \frac{\zeta_{ij}}{4} + \mathrm{i}\frac{\xi_{ij}}{4} := \int \mathrm{d}^n \boldsymbol{k} \beta_j(\boldsymbol{k}) \beta_i^*(\boldsymbol{k}). \tag{A.10}$$

The evaluation of T_{ij} depends on the kind of smearing function we chose. We provide an expression for ξ_{ij} and ζ_{ij} for a hard-sphere smearing function and a Gaussian smearing function in Appendix A.5.

A.2 Calculation of state of detectors

Initially all the detectors are in their respective ground state, $|g_\nu\rangle$, and the field in a coherent state, $|\beta_0(\boldsymbol{k})\rangle$, defined in Eq. (3.8). We can write the initial state of all the detectors and the field in the $|s_\nu\rangle$ basis, as given in (3.11), as

$$|\psi_0\rangle = \frac{1}{\sqrt{2}}\big(|1_1\rangle + |-1_1\rangle \big) \otimes \dots \otimes \frac{1}{\sqrt{2}}\big(|1_N\rangle + |-1_N\rangle \big) \otimes |\beta_0(\boldsymbol{k})\rangle = \frac{1}{\sqrt{2^N}} \sum_{\vec{s}'} |\vec{s}'\rangle \otimes \hat{D}_{\beta_0(\boldsymbol{k})} |0\rangle . \tag{A.11}$$

The final state of the detector and the fields thus is,

$$\begin{aligned} |\psi\rangle = \hat{U} |\psi_0\rangle &= \frac{1}{\sqrt{2^N}} \sum_{\vec{s}} \hat{P}_{s_N} \dots \hat{P}_{s_1} \otimes \hat{D}_{s_N \beta_N(\boldsymbol{k})} \dots \hat{D}_{s_1 \beta_1(\boldsymbol{k})} \sum_{\vec{s}'} |\vec{s}\rangle \otimes \hat{D}_{\beta_0(\boldsymbol{k})} |0\rangle \\ &= \frac{1}{\sqrt{2^N}} \sum_{\vec{s}'} |\vec{s}\rangle \otimes \hat{D}_{s_N \beta_N(\boldsymbol{k})} \dots \hat{D}_{s_1 \beta_1(\boldsymbol{k})} \hat{D}_{\beta_0(\boldsymbol{k})} |0\rangle . \end{aligned} \tag{A.12}$$

Using equation (A.9) to evaluate the product of the displacement operators, we retrieve Eq. (3.18),

$$|\psi\rangle = \frac{1}{\sqrt{2^N}} \sum_{\vec{s}} \exp\left[\mathrm{i} \sum_{i=0}^{N} \sum_{j\geq i}^{N} s_j s_i \,\mathrm{Im}(T_{ij})\right] |\vec{s}\rangle \otimes |\sum_{i=0} s_i \beta_i(\boldsymbol{k})\rangle \,. \tag{A.13}$$

As explained in the text, the first sum is over the possible sets $\{s_1, \ldots, s_N\}$, the second and third sum are over the indices i that run from 0 to N, with the understanding that $s_0 = 1$. Now that we have found the final joint detector and field state, we can trace out the field degree of freedom to obtain the state of the detectors,

$$\hat{\rho} = \mathrm{Tr}[|\psi\rangle\langle\psi|] = \frac{1}{2^N} \sum_{\vec{s},\vec{s}'} |\vec{s}\rangle\langle\vec{s}'| \mathrm{i} \sum_{i=0}^{N} \sum_{j\geq i}^{N} s_j s_i \,\mathrm{Im}(T_{ij})] \exp\left[-\mathrm{i} \sum_{i=0}^{N} \sum_{j\geq i}^{N} s'_j s'_i \,\mathrm{Im}(T_{ij})\right] \otimes \tag{A.14}$$

$$\left|\sum_{i=0} s'_i \beta_i(\boldsymbol{k}) \sum_{i=0} s_i \beta_i(\boldsymbol{k})\right\rangle. \tag{A.15}$$

We use Eq. (2.14) to calculate the inner product of the coherent states in Eq. (A.14). It turns out to be

$$\left\langle \sum_{i=0} s'_i \beta_i(\boldsymbol{k}) \middle| \sum_{i=0} s_i \beta_i(\boldsymbol{k}) \right\rangle = \exp\left[-\frac{1}{2} \sum_{i=0,j=0}^{N} T_{ij}(s_i s_j + s'_i s'_j - 2 s'_i s_j)\right]. \tag{A.16}$$

Using the above expression in Eq. (A.14), and after performing some algebraic simplifications, we obtain the state of all the detectors in Eq. (3.20) as

$$\hat{\rho}_{\mathrm{D}} = \frac{1}{2^N} \sum_{\vec{s},\vec{s}'} |\vec{s}\rangle\langle\vec{s}'| \exp\left[\sum_{i=0}^{N} T_{ii}(s_i s'_i - 1) + \sum_{i=0}^{N} \sum_{j<i}^{N} (T_{ij} s_j - T_{ji} s'_j)(s'_i - s_i)\right]. \tag{A.17}$$

The joint state of any two detectors (say A and B) is readily obtained from (3.20) by tracing over all other detectors i, such that $i \in \{1, 2, \ldots, N\}$ and $i \neq \mathrm{A}, i \neq \mathrm{B}$. Without loss of generality, let's assume that $A < B$. Performing the partial trace, we obtain

$$\hat{\rho}^{\mathrm{AB}} = \sum_{s_{\mathrm{A}}, s_{\mathrm{B}}, s'_{\mathrm{A}}, s'_{\mathrm{B}}} |s_{\mathrm{A}}, s_{\mathrm{B}}\rangle\langle s'_{\mathrm{A}}, s'_{\mathrm{B}}| \Theta(s_{\mathrm{A}}, s_{\mathrm{B}}, s'_{\mathrm{A}}, s'_{\mathrm{B}}) \exp[\mathrm{i}\theta_0(s_{\mathrm{A}}, s_{\mathrm{B}}, s'_{\mathrm{A}}, s'_{\mathrm{B}})] \prod_{j\neq a,b,j=1}^{N} \cos\theta_j(s_{\mathrm{A}}, s_{\mathrm{B}}, s'_{\mathrm{A}}, s'_{\mathrm{B}}), \tag{A.18}$$

where,

$$\Theta(s_{\rm A}, s_{\rm B}, s'_{\rm A}, s'_{\rm B}) = \frac{1}{4}\exp[T_{\rm AA}(s_{\rm A}s'_{\rm A}-1) + T_{\rm BB}(s_{\rm B}s'_{\rm B}-1) + (s_{\rm B}-s'_{\rm B})(T_{\rm AB}s'_{\rm A} - T_{\rm BA}s_{\rm A})],$$
$$\theta_j(s_{\rm A}, s_{\rm B}, s'_{\rm A}, s'_{\rm B}) = \left\{ \begin{array}{ll} 2(s_{\rm B}-s'_{\rm B})\,{\rm Im}[T_{j{\rm B}}] + 2(s_{\rm A}-s'_{\rm A})\,{\rm Im}[T_{ja}] & \forall\ 0 \le j < {\rm A} \\ 2(s_{\rm B}-s'_{\rm B})\,{\rm Im}[T_{j{\rm B}}] & \forall\ {\rm A} < j < {\rm B} \\ 0 & \forall\ j > {\rm B} \end{array} \right\}. \tag{A.19}$$

In this paper we only consider the first and the last detector as our targets for correlation harvesting. Thus we consider a particular case of the above, where A is the first detector to interact with the field and B is the last detector to interact with the field, with N detectors interacting in between. The state of the detectors A and B given in (3.21) is then readily obtained from Eqs. (A.18) and (A.19). The density matrix of the target detectors (3.21) written in the basis $\{|-1_{\rm A}\rangle|-1_{\rm B}\rangle, |-1_{\rm A}\rangle|1_{\rm B}\rangle, |1_{\rm A}\rangle|-1_{\rm B}\rangle, |1_{\rm A}\rangle|1_{\rm B}\rangle\}$ is given as follows:

$$\rho_{\rm AB} = \frac{1}{4}\begin{pmatrix} 1 & \rho_{12} & \rho_{13} & \rho_{14} \\ \rho^*_{12} & 1 & \rho_{23} & \rho_{24} \\ \rho^*_{13} & \rho^*_{23} & 1 & \rho_{34} \\ \rho^*_{14} & \rho^*_{24} & \rho^*_{34} & 1 \end{pmatrix}, \tag{A.20}$$

where we consider $\zeta := \zeta_{\rm BB} = \zeta_{\rm AA}$ and have the following matrix entries:

$$\rho_{12} = \exp\left[-\frac{\zeta}{2} - {\rm i}\xi_{0{\rm B}} + {\rm i}\xi_{\rm AB}\right]\prod_{j=1}^{N}\cos(\xi_{j{\rm B}}), \qquad \rho_{13} = \exp\left[-\frac{\zeta}{2} - {\rm i}\xi_{0{\rm A}}\right],$$
$$\rho_{23} = \exp[-\zeta + \zeta_{\rm AB} + {\rm i}\xi_{0{\rm B}} - {\rm i}\xi_{0{\rm A}}]\prod_{j=1}^{N}\cos(\xi_{j{\rm B}}), \qquad \rho_{24} = \exp\left[-\frac{\zeta}{2} - {\rm i}\xi_{0{\rm A}}\right],$$
$$\rho_{14} = \exp[-\zeta - \zeta_{\rm AB} - {\rm i}\xi_{0{\rm A}} - {\rm i}\xi_{0{\rm B}}]\prod_{j=1}^{N}\cos(\xi_{j{\rm B}}), \quad \rho_{34} = \exp\left[-\frac{\zeta}{2} - {\rm i}\xi_{0{\rm B}} - {\rm i}\xi_{\rm AB}\right]\prod_{j=1}^{N}\cos(\xi_{j{\rm B}}) \tag{A.21}$$

A.3 Calculating observable correlations

Here we calculate the correlations $\Gamma(\hat{S}^{\rm A}_m, \hat{S}^{\rm B}_n)$ for $m, n \in \{1, 2, 3\}$. We can write the operators $\hat{S}^{\nu}_i$ in the basis. For example,

$$\hat{S}^{\rm A}_1 = (|-1_{\rm A}\rangle\langle 1_{\rm A}| + |1_{\rm A}\rangle\langle -1_{\rm A}|) \otimes \mathbb{1}_{\rm B} = \begin{pmatrix} 0 & 0 & 1 & 0 \\ 0 & 0 & 0 & 1 \\ 1 & 0 & 0 & 0 \\ 0 & 1 & 0 & 0 \end{pmatrix}, \tag{A.22}$$

$$\hat{S}^{\rm B}_1 = \mathbb{1}_{\rm A} \otimes (|-1_{\rm B}\rangle\langle 1_{\rm B}| + |1_{\rm B}\rangle\langle -1_{\rm B}|) = \begin{pmatrix} 0 & 1 & 0 & 0 \\ 1 & 0 & 0 & 0 \\ 0 & 0 & 0 & 1 \\ 0 & 0 & 1 & 0 \end{pmatrix}. \tag{A.23}$$

Similarly we can write matrix forms for other operators. Now we can calculate $\Gamma(\hat{S}^{\rm A}_1, \hat{S}^{\rm B}_1)$ using the density matrix (A.20) and the matrix forms of the appropriate $\hat{S}^{\nu}_m$. For example, the correlation $\Gamma(\hat{S}^{\rm B}_1, \hat{S}^{\rm A}_1)$ is given by:

$$\Gamma(\hat{S}^{\rm A}_1, \hat{S}^{\rm B}_1) = {\rm Tr}[\rho_{\rm AB} S^{\rm A}_1 S^{\rm B}_1] - {\rm Tr}[\rho_{\rm AB} S^{\rm B}_1]\,{\rm Tr}[\rho_{\rm AB} S^{\rm A}_1] = \tag{A.24}$$

$$\frac{1}{2}({\rm Re}[\rho_{23}] + {\rm Re}[\rho_{14}]) - \frac{1}{2}({\rm Re}[\rho_{12}])({\rm Re}[\rho_{13}] + {\rm Re}[\rho_{24}]). \tag{A.25}$$

We calculate the other correlations in a similar fashion, and the expression for them in terms of the elements of the density matrix ρ_{ab} are given below:

$$\Gamma(\hat{S}^{\rm A}_1, \hat{S}^{\rm B}_2) = \frac{1}{2}({\rm Im}[\rho_{14}] + {\rm Re}[\rho_{23}]) - \frac{1}{2}({\rm Im}[\rho_{12}])({\rm Re}[\rho_{13}] + {\rm Re}[\rho_{24}]), \tag{A.26}$$

$$\Gamma(\hat{S}^{\rm A}_1, \hat{S}^{\rm B}_3) = \frac{1}{2}({\rm Re}[\rho_{24}] - {\rm Re}[\rho_{13}]), \tag{A.27}$$

$$\Gamma(\hat{S}^{\rm A}_2, \hat{S}^{\rm B}_1) = \frac{1}{2}({\rm Im}[\rho_{23}] + {\rm Im}[\rho_{14}]) - \frac{1}{2}({\rm Re}[\rho_{12}])({\rm Im}[\rho_{13}] + {\rm Im}[\rho_{24}]), \tag{A.28}$$

$$\Gamma(\hat{S}^{\rm A}_2, \hat{S}^{\rm B}_2) = \frac{1}{2}({\rm Re}[\rho_{23}] - {\rm Re}[\rho_{14}]) - \frac{1}{2}({\rm Im}[\rho_{12}])({\rm Im}[\rho_{13}] + {\rm Im}[\rho_{24}]), \tag{A.29}$$

$$\Gamma(\hat{S}^{\rm A}_2, \hat{S}^{\rm B}_3) = \frac{1}{2}({\rm Im}[\rho_{24}] - {\rm Im}[\rho_{13}]), \tag{A.30}$$

$$\Gamma(\hat{S}^{\rm A}_3, \hat{S}^{\rm B}_1) = \Gamma(\hat{S}^{\rm A}_3, \hat{S}^{\rm B}_2) = \Gamma(\hat{S}^{\rm A}_3, \hat{S}^{\rm B}_3) = 0. \tag{A.31}$$

Using the density matrix elements from Eq. (A.21), and the expressions for various $\Gamma(\hat{S}^{\rm A}_m, \hat{S}^{\rm B}_n)$ given above, we can evaluate the expression for correlation between any two

local operators $\hat{\mathcal{O}}^{\mathrm{A}}$ and $\hat{\mathcal{O}}^{\mathrm{B}}$ in Eq. (3.41) to obtain the general expression for $\Gamma(\hat{\mathcal{O}}^{\mathrm{A}}, \hat{\mathcal{O}}^{\mathrm{B}})$, Eq. (3.42).

A particularly interesting correlation to calculate is the correlation between the Hamiltonians of the detectors A and B. Note that for any detector ν, its Hamiltonian is given by:

$$\hat{H}_\nu = \Omega_\nu \left|e_\nu\right\rangle\!\left\langle e_\nu\right| = \frac{\Omega_\nu}{2}\hat{\mathbb{1}} + \frac{-\Omega_\nu}{2}\hat{S}_1^\nu. \tag{A.32}$$

Thus, in Eq. (3.42) we use $\zeta = \zeta_{\mathrm{BB}} = \zeta_{\mathrm{AA}}$, $a_1 = \frac{-\Omega_{\mathrm{A}}}{2}$, $b_1 = \frac{-\Omega_{\mathrm{B}}}{2}$ and $a_2 = a_3 = b_2 = b_3 = 0$, to obtain,

$$\Gamma(\hat{H}_{\mathrm{A}}, \hat{H}_{\mathrm{B}}) = \left(\frac{\Omega_{\mathrm{B}}}{2}\right)\left(\frac{\Omega_{\mathrm{A}}}{2}\right)\left(\prod_j \cos\xi_{j\mathrm{B}}\right)e^{-\zeta}\Big[(\cosh\zeta_{\mathrm{AB}} - \cos\xi_{\mathrm{AB}})\cos\xi_{0\mathrm{B}} + \sinh\zeta_{\mathrm{AB}}\sin\xi_{0\mathrm{B}}\Big]. \tag{A.33}$$

A.4 Calculating quantum discord

The calculation of quantum discord (3.58) involves the calculation of classical correlation and mutual information. The calculation of mutual information (3.44) turns out to be relatively simpler as it only depends on the eigenvalues of the joint density matrix and the density matrices of reduced subsystems. For classical correlation (3.47) however, analytical expressions occur only in a few cases such as for X-state density matrices [9], as the optimisation over the set of von Neumann measurements is harder in general. When the initial state of the field is the vacuum state (i.e $T_{0\nu}$ =0), the density matrix of target detectors indeed turns out to be an X-state in the basis

$$\{\left|g_{\mathrm{A}}\right\rangle\left|g_{\mathrm{B}}\right\rangle, e^{i\Omega_{\mathrm{B}}t_{\mathrm{B}}}\left|g_{\mathrm{A}}\right\rangle\left|e_{\mathrm{B}}\right\rangle, e^{i\Omega_{\mathrm{A}}t_{\mathrm{A}}}\left|e_{\mathrm{A}}\right\rangle\left|g_{\mathrm{B}}\right\rangle, e^{i\Omega_{\mathrm{A}}t_{\mathrm{A}}}e^{i\Omega_{\mathrm{B}}t_{\mathrm{B}}}\left|e_{\mathrm{A}}\right\rangle\left|e_{\mathrm{B}}\right\rangle\} \tag{A.34}$$

. we write the matrix form σ_{ab} of the state $\hat{\rho}_{\mathrm{AB}}$ (3.21) in this basis as:

$$\sigma_{\mathrm{AB}} = \begin{pmatrix} \sigma_{11} & 0 & 0 & \sigma_{14} \\ 0 & \sigma_{22} & \sigma_{23} & 0 \\ 0 & \sigma_{23}^* & \sigma_{33} & 0 \\ \sigma_{14}^* & 0 & 0 & \sigma_{44} \end{pmatrix} \tag{A.35}$$

Defining $\zeta \coloneqq \zeta_{\mathrm{BB}} = \zeta_{\mathrm{AA}}$, the matrix elements are:

$$\sigma_{11} = \frac{1}{4}\big[1 + \mathrm{e}^{-\frac{\zeta}{2}} + \mathrm{e}^{-\frac{\zeta}{2}} \cos\xi_{\mathrm{AB}} \prod_{j=1}^{N} \cos(\xi_{j\mathrm{B}}) + \mathrm{e}^{-\zeta} \cosh\zeta_{\mathrm{AB}} \prod_{j=1}^{N} \cos(\xi_{j\mathrm{B}})\big], \tag{A.36}$$

$$\sigma_{22} = \frac{1}{4}\big[1 + \mathrm{e}^{-\frac{\zeta}{2}} - \mathrm{e}^{-\frac{\zeta}{2}} \cos\xi_{\mathrm{AB}} \prod_{j=1}^{N} \cos(\xi_{j\mathrm{B}}) - \mathrm{e}^{-\zeta} \cosh\zeta_{\mathrm{AB}} \prod_{j=1}^{N} \cos(\xi_{j\mathrm{B}})\big], \tag{A.37}$$

$$\sigma_{33} = \frac{1}{4}\big[1 - \mathrm{e}^{-\frac{\zeta}{2}} + \mathrm{e}^{-\frac{\zeta}{2}} \cos\xi_{\mathrm{AB}} \prod_{j=1}^{N} \cos(\xi_{j\mathrm{B}}) - \mathrm{e}^{-\zeta} \cosh\zeta_{\mathrm{AB}} \prod_{j=1}^{N} \cos(\xi_{j\mathrm{B}})\big], \tag{A.38}$$

$$\sigma_{44} = \frac{1}{4}\big[1 - \mathrm{e}^{-\frac{\zeta}{2}} - \mathrm{e}^{-\frac{\zeta}{2}} \cos\xi_{\mathrm{AB}} \prod_{j=1}^{N} \cos(\xi_{j\mathrm{B}}) + \mathrm{e}^{-\zeta} \cosh\zeta_{\mathrm{AB}} \prod_{j=1}^{N} \cos(\xi_{j\mathrm{B}})\big], \tag{A.39}$$

$$\sigma_{14} = -\frac{1}{4}\mathrm{e}^{-\zeta}[\mathrm{i}\mathrm{e}^{\frac{\zeta}{2}} \sin\xi_{\mathrm{AB}} + \sinh\zeta_{\mathrm{AB}}] \prod_{j=1}^{N} \cos(\xi_{j\mathrm{B}}), \tag{A.40}$$

$$\sigma_{23} = \frac{1}{4}\mathrm{e}^{-\zeta}[\mathrm{i}\mathrm{e}^{\frac{\zeta}{2}} \sin\xi_{\mathrm{AB}} + \sinh\zeta_{\mathrm{AB}}] \prod_{j=1}^{N} \cos(\xi_{j\mathrm{B}}). \tag{A.41}$$

We show here the calculation of classical correlation and mutual information subsequently.

A.4.1 Mutual information

Recall that the definition of mutual information is given by Eq. (3.44). To calculate it, we use the matrix form σ_{ab} of the state $\hat{\rho}_{\mathrm{AB}}$ It is given by

$$\mathcal{I}(\sigma_{\mathrm{AB}}) = S(\sigma_{\mathrm{A}}) + S(\sigma_{\mathrm{B}}) + \sum_{j=0}^{3} \lambda_j \log_2 \lambda_j. \tag{A.42}$$

Here λ_j are the eigenvalues of the matrix σ_{AB} We first compute $S(\sigma_{\mathrm{A}})$ and $S(\sigma_{\mathrm{B}})$, the entropies of each of the reduced states:

$$S(\sigma_{\mathrm{A}}) = -[(\sigma_{11} + \sigma_{22}) \log_2(\sigma_{11} + \sigma_{22}) + (\sigma_{33} + \sigma_{44}) \log_2(\sigma_{33} + \sigma_{44})], \tag{A.43}$$

$$S(\sigma_{\mathrm{B}}) = -[(\sigma_{11} + \sigma_{33}) \log_2(\sigma_{11} + \sigma_{33}) + (\sigma_{22} + \sigma_{44}) \log_2(\sigma_{22} + \sigma_{44})]. \tag{A.44}$$

It's straightforward to obtain:

$$\sigma_{11}+\sigma_{33}=\frac{1}{2}\left(1+\mathrm{e}^{-\frac{\zeta}{2}}\cos\xi_{\mathrm{AB}}\prod_{j=1}^{N}\cos(\xi_{j\mathrm{B}})\right),\qquad \sigma_{11}+\sigma_{22}=\frac{1}{2}(1+\mathrm{e}^{-\frac{\zeta}{2}}),\tag{A.45}$$

$$\sigma_{22}+\sigma_{44}=\frac{1}{2}\left(1-\mathrm{e}^{-\frac{\zeta}{2}}\cos\xi_{\mathrm{AB}}\prod_{j=1}^{N}\cos(\xi_{j\mathrm{B}})\right),\qquad \sigma_{33}+\sigma_{44}=\frac{1}{2}(1-\mathrm{e}^{-\frac{\zeta}{2}}).\tag{A.46}$$

Using the following definition of $g(x)$ (3.46) we obtain

$$S(\sigma_{\mathrm{B}})=g\left(\mathrm{e}^{-\frac{\zeta}{2}}\cos\xi_{\mathrm{AB}}\prod_{j=1}^{N}\cos(\xi_{j\mathrm{B}})\right),\qquad S(\sigma_{\mathrm{A}})=g(\mathrm{e}^{-\frac{\zeta}{2}}).\tag{A.47}$$

We calculate now the term $\sum_{j=0}^{3}\lambda_j\log_2\lambda_j$. From [9] we note that

$$\lambda_0=\frac{1}{2}(a_1+a_2),\quad \lambda_1=\frac{1}{2}(a_1-a_2),\quad \lambda_2=\frac{1}{2}(b_1+b_2),\quad \lambda_3=\frac{1}{2}(b_1-b_2),\tag{A.48}$$

$$a_1=\sigma_{11}+\sigma_{44}=\frac{1}{2}\left(1+\mathrm{e}^{-\zeta}\cosh\zeta_{\mathrm{AB}}\prod_{j=1}^{N}\cos(\xi_{j\mathrm{B}})\right),\tag{A.49}$$

$$a_2=\sqrt{(\sigma_{11}-\sigma_{44})^2+4|\sigma_{14}|^2}=\tag{A.50}$$

$$\frac{\mathrm{e}^{-\zeta/2}}{2}\sqrt{1+2\cos\xi_{\mathrm{AB}}\prod_{j=1}^{N}\cos(\xi_{j\mathrm{B}})+\left(1+e^{-\zeta}\sinh^2\zeta_{\mathrm{AB}}\right)\left(\prod_{j=1}^{N}\cos(\xi_{j\mathrm{B}})\right)^2},\tag{A.51}$$

$$b_1=\sigma_{22}+\sigma_{33}=\frac{1}{2}\left(1-\mathrm{e}^{-\zeta}\cosh\zeta_{\mathrm{AB}}\prod_{j=1}^{N}\cos(\xi_{j\mathrm{B}})\right),\tag{A.52}$$

$$b_2=\sqrt{(\sigma_{22}-\sigma_{33})^2+4|\sigma_{23}|^2}=\tag{A.53}$$

$$\frac{\mathrm{e}^{-\zeta/2}}{2}\sqrt{1-2\cos\xi_{\mathrm{AB}}\prod_{j=1}^{N}\cos(\xi_{j\mathrm{B}})+\left(1+e^{-\zeta}\sinh^2\zeta_{\mathrm{AB}}\right)\left(\prod_{j=1}^{N}\cos(\xi_{j\mathrm{B}})\right)^2}.\tag{A.54}$$

The term $\sum_{j=0}^{3}\lambda_j\log_2\lambda_j$ can be manipulated to the form it has in Eq. (A.56). For example the first two terms in the sum can be written as

$$\begin{aligned}\lambda_0 \log_2 \lambda_0 + \lambda_1 \log_2 \lambda_1 &= \frac{a_1+a_2}{2}\log_2\Big(\frac{a_1+a_2}{2}\Big) + \frac{a_1-a_2}{2}\log_2\Big(\frac{a_1-a_2}{2}\Big) \\ &= a_1\Big(\frac{1+a_2/a_1}{2}\log_2\Big(\frac{a_1+a_2}{2}\Big) + \frac{1-a_2/a_1}{2}\log_2\Big(\frac{a_1-a_2}{2}\Big)\Big) = \\ &= a_1\log_2(a_1) + a_1\Big(\frac{1+a_2/a_1}{2}\log_2\Big(\frac{1+a_2/a_1}{2}\Big) + \\ &\quad \frac{1-a_2/a_1}{2}\log_2\Big(\frac{1-a_2/a_1}{2}\Big)\Big) = a_1\log_2(a_1) - a_1 g(a_2/a_1).\end{aligned} \tag{A.55}$$

Similarly, $\lambda_2 \log_2 \lambda_2 + \lambda_3 \log_2 \lambda_3 = b_1 \log_2(b_1) - b_1 g(b_2/b_1)$. Therefore we obtain

$$-S(\hat{\rho}_{\text{AB}}) = \sum_{j=0}^{3} \lambda_j \log_2 \lambda_j = a_1 \log_2(a_1) + b_1 \log_2(b_1) - a_1 g(a_2/a_1) - b_1 g(b_2/b_1). \tag{A.56}$$

Hence from Eqs. (A.47) and (A.56) we retrieve Eqs. (3.45) and (3.46).

A.4.2 Classical correlation

Here we follow the approach in [9] to calculate the classical correlation $\mathcal{C}(\hat{\rho})$. Recall that it is defined (3.47) as

$$\mathcal{C}(\hat{\rho}_{\text{AB}}) = S(\hat{\rho}_{\text{A}}) - \inf_{\{\hat{M}_k\}} S(\hat{\rho}_{\text{AB}}|\{\hat{M}_k\}) = S(\hat{\rho}_{\text{A}}) - \inf_{\{\hat{M}_k\}} \sum_{k\in\{0,1\}} p_k S(\hat{\rho}^{(k)}_{\text{AB}}). \tag{A.57}$$

Here M_k are von Neumann measurements on the B subsystem; $M_0 = \hat{V}\,|g_{\text{B}}\rangle\,\langle g_{\text{B}}|\,\hat{V}^\dagger$ and $M_1 = \hat{V}\,|e_{\text{B}}\rangle\,\langle e_{\text{B}}|\,\hat{V}^\dagger$ where $\hat{V} \in SU(2)$

$$\hat{\rho}^{(k)}_{\text{AB}} = \frac{1}{p_k}(\mathbb{1}\otimes\hat{M}_k)\hat{\rho}_{\text{AB}}(\mathbb{1}\otimes\hat{M}_k), \qquad p_k = \text{Tr}\Big[(\mathbb{1}\otimes\hat{M}_k)\hat{\rho}_{\text{AB}}(\mathbb{1}\otimes M_k)\Big]. \tag{A.58}$$

Each $\hat{V} \in SU(2)$ can be written as $\hat{V} = t\mathbb{1} + i\vec{y}.\vec{\sigma}$, where $t, y_1, y_2, y_3 \in \mathbb{R}$ satisfy $t^2 + y_1^2 + y_2^2 + y_3^2 = 1$ and $\vec{\sigma}$ denotes the triad of Pauli operators $(\sigma_x, \sigma_y, \sigma_z)$. As there is a one-one relation between $SU(2)$ and the set of von Neumann measurements $\{\hat{M}_k\}$, the latter can be characterised by the 3 parameter set of *SU(2)* operators. Thus we can simply minimise $S(\hat{\rho}_{\text{AB}}|\{\hat{M}_k\})$ over the possible range of parameters t, y_1, y_2, y_3. To perform our

calculations we use the matrix $\sigma_{\rm AB}$ and all the results are in terms of its matrix elements. We define the 3 parameters $k = t^2 + y_3^2, m = (ty_1 + y_2y_3)^2, n = (ty_2 - y_1y_3)(ty_1 + y_2y_3)$ and $l = y_1^2 + y_2^2 = 1 - k$, which yields a simpler relation for $S(\hat{\rho}_{\rm AB}|\{\hat{M}_k\})$. The probability of an outcome $\hat{\rho}_{\rm AB}^{(k)}$ is given by

$$\begin{aligned} p_0 &= [(\sigma_{11} + \sigma_{33})k + (\sigma_{22} + \sigma_{44})l], \\ p_1 &= [(\sigma_{11} + \sigma_{33})l + (\sigma_{22} + \sigma_{44})k]. \end{aligned} \tag{A.59}$$

The von Neumann entropies of the measurement outcomes $\sigma_{\rm AB}^{(i)}$ are given by

$$S(\sigma_{\rm AB}^{(0)}) = g(\theta), \qquad S(\sigma_{\rm AB}^{(1)}) = g(\theta'). \tag{A.60}$$

Note that, $g(x)$ has been defined in Eq. (3.46). θ and θ' in the above equation are given by

$$\theta = \sqrt{\frac{[(\sigma_{11} - \sigma_{33})k + (\sigma_{22} - \sigma_{44})l]^2 + \Theta}{[(\sigma_{11} + \sigma_{33})k + (\sigma_{22} + \sigma_{44})l]^2}}, \qquad \theta' = \sqrt{\frac{[(\sigma_{11} - \sigma_{33})l + (\sigma_{22} - \sigma_{44})k]^2 + \Theta}{[(\sigma_{11} + \sigma_{33})l + (\sigma_{22} + \sigma_{44})k]^2}}. \tag{A.61}$$

where $\Theta = 4kl[|\sigma_{14}|^2 + |\sigma_{23}|^2 + 2\,\mathrm{Re}(\sigma_{14}\sigma_{23}^*)] - 16m\,\mathrm{Re}(\sigma_{14}\sigma_{23}^*) + 16n\,\mathrm{Im}(\sigma_{14}\sigma_{23}^*)$, according to [8].

According to [9], the minimum value of $S(\hat{\rho}_{\rm AB}|\{\hat{M}_k\})$ occurs in one of the following cases : 1) $k = 1, l = 0 (m = 0, n = 0)$ or 2) $k = l = \frac{1}{2}, m \in \{0, \frac{1}{4}\}, n \in \{0, \pm\frac{1}{8}\}$. First we look at the case $k = l = 1/2$. It is easy to see that for this case, $p_0 = p_1 = 1/2$ and $\theta = \theta' = \sqrt{[\sigma_{11} + \sigma_{22} - \sigma_{33} - \sigma_{44}]^2 + 4\Theta}$. Thus, we need to simply minimise $g(\theta)$. For positive $\theta, g(\theta)$ is a monotonically decreasing function. Thus we simply must chose the maximum value of θ out of the 6 possibilities for m and n. Using the elements of the density matrix from (A.36), we find that

$$\theta = e^{-\zeta/2}\sqrt{1 + 4me^{-\zeta}[\sinh^2\zeta_{\rm AB} + e^{\zeta}\sin^2\xi_{\rm AB}]\left(\prod_{j=1}^{N}\cos(\xi_{j\rm B})\right)^2}. \tag{A.62}$$

Clearly, theta increases with m, so $m = 1/4$ is the appropriate choice. Thus, when $k = l = 1/2$ we have

$$S(\hat{\rho}_{\rm AB}|\{\hat{M}_k\}) = g\left(e^{-\zeta/2}\sqrt{1 + e^{-\zeta}[\sinh^2\zeta_{\rm AB} + e^{\zeta}\sin^2\xi_{\rm AB}]\left(\prod_{j=1}^{N}\cos(\xi_{j\rm B})\right)^2}\right). \tag{A.63}$$

Now, we look at the case when $k = 1, l = 0$. This is same as the case $k = 0, l = 1$. In either cases, $m = n = 0$. Thus $\Theta = 0$. By simply substituting the values of the density matrix elements, we get,

$$\begin{aligned}
&S(\hat{\rho}_{\text{AB}}|\{\hat{M}_k\}) = p_0 g(\theta_0) + p_1 g(\theta_1), \\
&p_0 = \frac{1}{2}(1 + e^{-\zeta/2} \cos\xi_{\text{AB}} \prod_{j=1}^{N} \cos(\xi_{j\text{B}})), \\
&p_1 = \frac{1}{2}(1 - e^{-\zeta/2} \cos\xi_{\text{AB}} \prod_{j=1}^{N} \cos(\xi_{j\text{B}})), \\
&\theta_0 = \frac{\left|\mathrm{e}^{-\zeta/2} + \mathrm{e}^{-\zeta} \cosh\zeta_{\text{AB}} \prod_{j=1}^{N} \cos(\xi_{j\text{B}})\right|}{2p_0}, \\
&\theta_1 = \frac{\left|\mathrm{e}^{-\zeta/2} - \mathrm{e}^{-\zeta} \cosh\zeta_{\text{AB}} \prod_{j=1}^{N} \cos(\xi_{j\text{B}})\right|}{2p_1}
\end{aligned} \tag{A.64}$$

Chosing the minimum out of the two values of $S(\hat{\rho}_{\text{AB}}|\{\hat{M}_k\})$ from Eq. (A.63) and (A.64), we get the formula for classical correlation mentioned in Eq. (3.53).

A.4.3 Optimality of discord formula

To check whether the discord formula is correct we need to prove that one of two conditions for a two-qubit system is correct [27]. To check those conditions we first have to transform our density matrix (A.35) to a real matrix via a local unitary operation.

One unitary that succeeds in this transformation is $U_{\text{A}} \otimes \mathbb{1}_{\text{B}}$, with

$$U_{\text{A}} = \begin{pmatrix} u_{00} & 0 \\ 0 & u_{11} \end{pmatrix}. \tag{A.65}$$

The only condition needed is that $|u_{00}| = |u_{11}| = 1$ and that $\text{Im}(u_{00} u_{11}^* \sigma_{23}) = 0$. Therefore one possible choice is $u_{11} = 1$ and

$$u_{00} = \frac{\sinh\zeta_{\text{AB}} - \mathrm{i}\mathrm{e}^{\frac{\zeta}{2}} \sin\xi_{\text{AB}}}{\sqrt{\sinh^2\zeta_{\text{AB}} + \mathrm{e}^{\zeta} \sin^2\xi_{\text{AB}}}} \tag{A.66}$$

In that case, the density matrix (A.35) transforms to:

$$\sigma_{\text{AB}} = \begin{pmatrix} \sigma_{11} & 0 & 0 & -|\sigma_{23}| \\ 0 & \sigma_{22} & |\sigma_{23}| & 0 \\ 0 & |\sigma_{23}| & \sigma_{33} & 0 \\ -|\sigma_{23}| & 0 & 0 & \sigma_{44} \end{pmatrix} \tag{A.67}$$

with the same matrix entries than in the previous appendix.

In that case, it is easy to check from [27] the two following conditions, corresponding to σ_z^{A} or σ_x^{A} being the optimal measurement respectively:

$$4(|\sigma_{23}|^2) \leq (\sigma_{11} - \sigma_{22})(\sigma_{44} - \sigma_{33}), \tag{A.68}$$

$$|\sqrt{\sigma_{11}\sigma_{44}} - \sqrt{\sigma_{22}\sigma_{33}}| \leq 2|\sigma_{23}|. \tag{A.69}$$

It is simple to check with our values that the first condition is always false, independent of parameters. The second condition though, for the cases we study, is always met. In this appendix we plot function $f(\sigma_{ij}) = \left|\sqrt{\sigma_{11}\sigma_{44}} - \sqrt{\sigma_{22}\sigma_{33}}\right| - 2|\sigma_{23}|$ for the different values that we consider in Fig. A.1, A.2 and A.3.

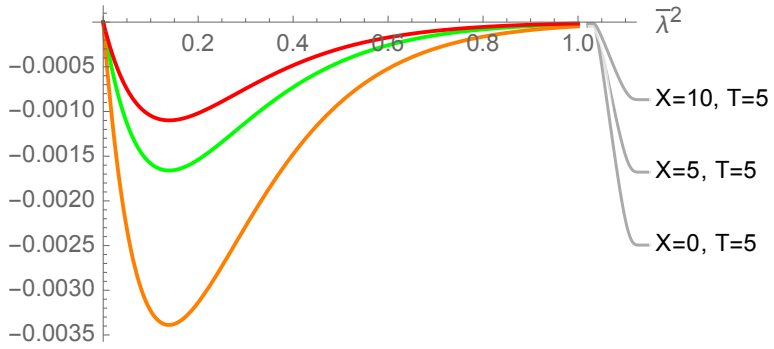

Figure A.1: Plot of function $f(\sigma_{ij})$ for different coupling strengths.
The smearing function has been chosen to be 3-dimensional hard-sphere with radius equal to $\sigma = 1$, as given in (3.33). The initial state of the field is the vacuum. The function is negative so the formula for quantum discord is optimal for this range of parameters.

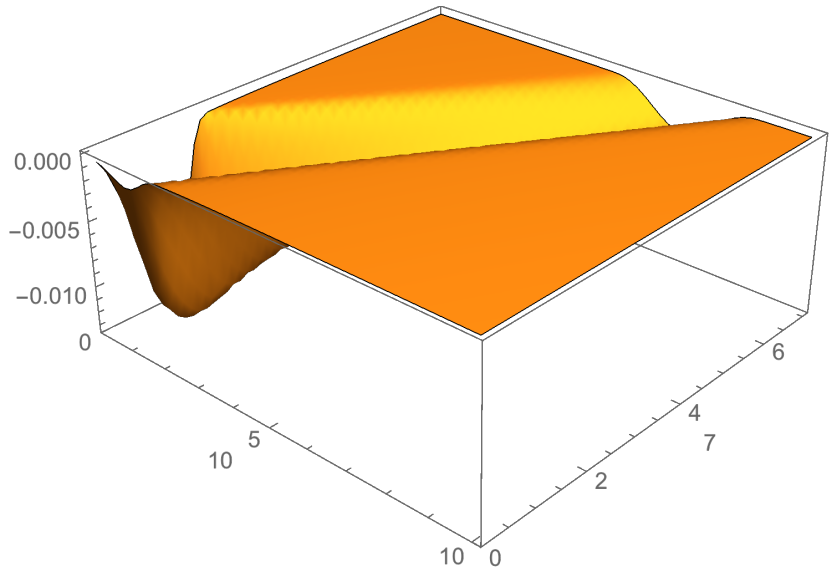

Figure A.2: Plot of function $f(\sigma_{ij})$ depending on relative position of the detectors A and B.
Coupling strength is set to $\tilde{\lambda}^2 = 1$. The smearing function has been chosen to be 3-dimensional hard-sphere with radius equal to $\sigma = 1$, as given in (3.33). We consider a scenario in which there are no other detectors, presents, i.e., $\xi_{\text{IB}} = 0$. We consider that the initial state of the field is the vacuum state. Plotted from $X = 0$ to $X = 10\sigma$ The initial state of the field is the vacuum. The function is negative so the formula for quantum discord is optimal for this range of parameters.

A.5 Calculation of T_{ij}

Here we intend to evaluate the integral in the definition of T_{ij} in (A.10). Recall, that

$$\begin{aligned} \beta_\nu(\boldsymbol{k}) &= -\mathrm{i}\tilde{\lambda}_\nu \frac{\tilde{F}_\nu(-\boldsymbol{k})}{\sqrt{2|\boldsymbol{k}|}} e^{\mathrm{i}(|\boldsymbol{k}|t_\nu - \boldsymbol{k}\cdot\boldsymbol{x_\nu})}, \\ T_{ij} &= \frac{\zeta_{ij}}{4} + \mathrm{i}\frac{\xi_{ij}}{4} := \int \mathrm{d}^n\boldsymbol{k}\beta_i^*(\boldsymbol{k})\beta_j(\boldsymbol{k}). \end{aligned} \tag{A.70}$$

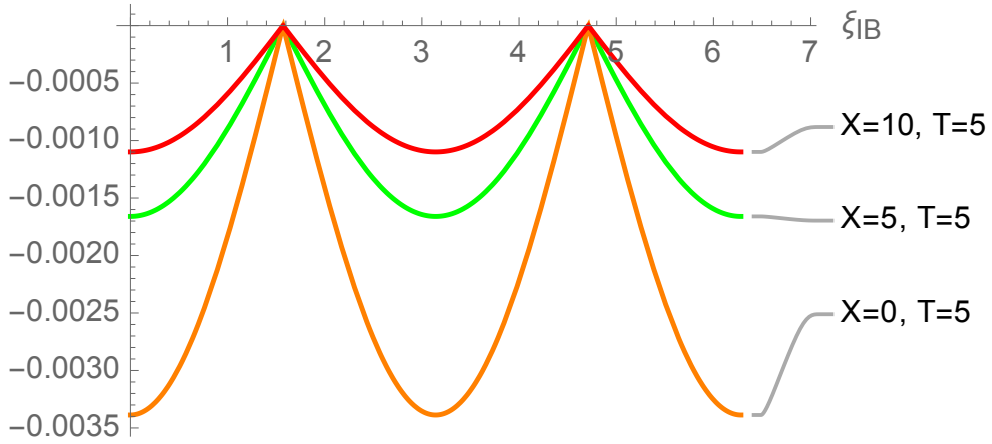

Figure A.3: Dependence of $f(\sigma_{ij})$ with respect to ξ_{IB}.
We consider a scenario in which there is a single interloper detector, I, and we analyze the dependence of $f(\sigma_{ij})$ with respect to ξ_{IB} (for the rest of the detectors, $\xi_{\text{JB}} = 0$). The term ξ_{IB} depends on the coupling strength of the middle detector and the relative position between detector I and the last detector, B. Coupling strength is set to $\bar{\lambda}^2 = 0.2$. The smearing function has been chosen to be 3-dimensional hard-sphere with radius equal to $\sigma = 1$, as given in (3.33). We consider that the initial state of the field is the vacuum state. The function is negative so the formula for quantum discord is optimal for this range of parameters.

Plugging $\beta_\nu(\boldsymbol{k})$ back in the expression for T_{ij}, we see that the required integral can be cast in the following form, ignoring the constants.

$$T_{ij} = \tilde{\lambda}_i \tilde{\lambda}_j \int \mathrm{d}^n \boldsymbol{k} \frac{\tilde{F}_i(\boldsymbol{k}) \tilde{F}_j(-\boldsymbol{k})}{2|\boldsymbol{k}|} e^{\mathrm{i}(|\boldsymbol{k}|T - \boldsymbol{k}\cdot\boldsymbol{X})}, \tag{A.71}$$

where $\boldsymbol{X} = \boldsymbol{x_j} - \boldsymbol{x_i}$ and $T = t_j - t_i$.

We note that when we have identical detectors (hence smearing functions of all detectors are same), T_{ii} is constant, independent of the parameters of the detector. It can be readily seen by substituting $\boldsymbol{X} = 0$ and $T = 0$, in the above expression. Thus we define the constant $\zeta := 4T_{ii}$.

The product of the two Fourier transforms $\tilde{F}_i(-\boldsymbol{k})\tilde{F}_j(\boldsymbol{k})$ can be written as the Fourier transform of a convolution(we are assuming that $\tilde{F}$ is a real function), in the following

way:

$$\tilde{F}_i(-\boldsymbol{k})\tilde{F}_j(\boldsymbol{k}) = \frac{1}{\sqrt{(2\pi)^n}} \int\int \mathrm{d}^n\boldsymbol{x'}\mathrm{d}^n\boldsymbol{z'} F_j(\boldsymbol{z'})F_i(\boldsymbol{x'}+\boldsymbol{z'})e^{\mathrm{i}\boldsymbol{k}\cdot\boldsymbol{x'}}. \tag{A.72}$$

Plugging it into equation (A.71) we get the expression

$$T_{ij} = \frac{\tilde{\lambda}_i\tilde{\lambda}_j}{\sqrt{(2\pi)^n}} \int\int \mathrm{d}^n\boldsymbol{x'}\mathrm{d}^n\boldsymbol{z'}\ F_j(\boldsymbol{z'})F_i(\boldsymbol{x'}+\boldsymbol{z'}) \int \mathrm{d}^n\boldsymbol{k} \frac{e^{\mathrm{i}|\boldsymbol{k}|T+\mathrm{i}\boldsymbol{k}\cdot(\boldsymbol{x'}-\boldsymbol{X})}}{2|\boldsymbol{k}|}. \tag{A.73}$$

The integral over $\boldsymbol{k}$ can be partially simplified using the properties of Bessel functions of the first kind, $J_n(x)$,

$$\int \mathrm{d}^n\boldsymbol{k} \frac{e^{\mathrm{i}|\boldsymbol{k}|T+\mathrm{i}\boldsymbol{k}\cdot(\boldsymbol{x'}-\boldsymbol{X})}}{2|\boldsymbol{k}|} = \frac{\sqrt{(2\pi)^n}}{2} \int_0^\infty \mathrm{d}k \left(\frac{k}{|\boldsymbol{x'}-\boldsymbol{X}|}\right)^{\frac{n}{2}-1} J_{\frac{n}{2}-1}\Big(k|\boldsymbol{x'}-\boldsymbol{X}|\Big)e^{\mathrm{i}kT}, \tag{A.74}$$

where $k = |\boldsymbol{k}|$. We perform the above integral for the specific case of 3 spatial dimensions ($n = 3$), in which case the required Bessel function is $J_{1/2}(x) = \sqrt{\frac{2}{\pi x}}\sin x$. Thus for $n = 3$, Eq. (A.74) becomes

$$\int \mathrm{d}^3\boldsymbol{k} \frac{e^{\mathrm{i}|\boldsymbol{k}|T+\mathrm{i}\boldsymbol{k}\cdot(\boldsymbol{x'}-\boldsymbol{X})}}{2|\boldsymbol{k}|} = \frac{2\pi}{|\boldsymbol{x'}-\boldsymbol{X}|} \int_0^\infty \mathrm{d}k\ \sin\left(k|\boldsymbol{x'}-\boldsymbol{X}|\right)e^{\mathrm{i}kT}. \tag{A.75}$$

To calculate the above, we make use of the following identities:

$$\begin{aligned} e^{\mathrm{i}k\alpha} &= \cos k\alpha + \mathrm{i}\sin k\alpha, \\ \int_0^\infty dk \cos k\alpha &= \pi\delta(\alpha), \\ \int_0^\infty dk \sin k\alpha &= \left\{ \begin{array}{ll} \frac{1}{\alpha} & \alpha \neq 0 \\ 0 & \alpha = 0 \end{array} \right\}. \end{aligned} \tag{A.76}$$

Now, we can write $\sin\left(k|\boldsymbol{x'}-\boldsymbol{X}|\right)$ using $e^{\mathrm{i}k|\boldsymbol{x'}-\boldsymbol{X}|}$ and using the above identities, we find out that:

$$\int \mathrm{d}^3\boldsymbol{k} \frac{e^{\mathrm{i}|\boldsymbol{k}|T+\mathrm{i}\boldsymbol{k}\cdot(\boldsymbol{x'}-\boldsymbol{X})}}{2|\boldsymbol{k}|} = \frac{2\pi}{|\boldsymbol{x'}-\boldsymbol{X}|} \left[\frac{|\boldsymbol{x'}-\boldsymbol{X}|}{|\boldsymbol{x'}-\boldsymbol{X}|^2 - T^2} + \mathrm{i}\frac{\pi}{2}\Big[\delta\Big(|\boldsymbol{x'}-\boldsymbol{X}|-T\Big) - \delta\Big(|\boldsymbol{x'}-\boldsymbol{X}|+T\Big)\Big]\right]. \tag{A.77}$$

Note that since $|\boldsymbol{x'}-\boldsymbol{X}|$ is always non-negative, hence only one of the Dirac deltas in the imaginary part will contribute to T_{ij}, depending upon the sign of T.

We have thus performed the k integral for a 3-D space. This integration doesn't depend on the choice of smearing functions of the detector. From this point on, we need to consider specific examples of smearing functions to compute T_{ij} using Eqs. (A.73) and (A.77).

A.5.1 Hard sphere smearing function

First we consider the smearing function to be a normalised hard sphere for a 3 dimensional case:

$$F(\boldsymbol{x}) = \left\{ \begin{array}{ll} \frac{3}{4\pi\sigma^3} & |\boldsymbol{x}| \leq \sigma \\ 0 & |\boldsymbol{x}| > \sigma \end{array} \right\}, \tag{A.78}$$

where $F(\boldsymbol{x})$ is 0 outside a sphere of radius σ centered at the origin.

Imaginary part

For the case of 3 spatial dimensions, ξ_{ij} which is 4 times the imaginary part of T_{ij} is calculated from Eqs. (A.77) and (A.73), and is given by:

$$\xi_{ij} = \tilde{\lambda}_i \tilde{\lambda}_j \sqrt{2\pi} \int\int \mathrm{d}^3\boldsymbol{x'}\, d^3\mathbf{z'}\, F_j(\boldsymbol{z'}) F_i(\boldsymbol{x'} + \boldsymbol{z'}) \frac{T\delta(|\boldsymbol{x'} - \boldsymbol{X}| - |T|)}{|T||\boldsymbol{x'} - \boldsymbol{X}|}. \tag{A.79}$$

Plugging this smearing function into the above, we notice that the integral over $\boldsymbol{z}$ is simply the volume of intersection between two n-spheres of radius σ separated by a distance x'. Thus the $\boldsymbol{z'}$ integral is easily performed, and in particular the for the 3 dimensional case it turns out to be $\frac{3}{8\pi\sigma^3}(1 - \frac{x'}{2\sigma})^2(2 + \frac{x'}{2\sigma})$ when $x' \leq 2\sigma$ (i.e when there is some intersection between the spheres) and 0 otherwise. Using this we get

$$\xi_{ij} = \tilde{\lambda}_i \tilde{\lambda}_j \frac{3\sqrt{2\pi}}{8\pi\sigma^3} \int_{x' \leq 2\sigma} \mathrm{d}^3\boldsymbol{x'} \Big(1 - \frac{x'}{2\sigma}\Big)^2 \Big(2 + \frac{x'}{2\sigma}\Big) \frac{T\delta(|\boldsymbol{x'} - \boldsymbol{X}| - |T|)}{|T||\boldsymbol{x'} - \boldsymbol{X}|}. \tag{A.80}$$

To calculate the above we use spherical coordinates and use the variable substitution $\boldsymbol{r} = \boldsymbol{x'} - \boldsymbol{X}$. Without loss of generality, we can choose $\boldsymbol{X} = (0, 0, |\boldsymbol{X}|)$. We observe that the original volume of integration is a sphere with radius 2σ centered in $-\boldsymbol{X}$. To get a clearer picture of the integral we can use spherical coordinates, and parametrize $\boldsymbol{r}$ as $\boldsymbol{r} = r(\cos\phi \sin\theta, \sin\phi \sin\theta, \cos\theta)$ with $\phi \in (0, 2\pi)$ and $\theta \in (0, \pi)$. We observe that

$$|\boldsymbol{r} + \boldsymbol{X}|^2 = r^2 + 2r|\boldsymbol{X}| \cos\theta + |\boldsymbol{X}|^2. \tag{A.81}$$

Since we have the term $\delta(r - |T|)$, the volume of integration parametrized by r, ϕ, θ will become an area parametrized by ϕ, θ. This area will be the intersection of a shell centered in $\mathbf{0} = (0, 0, 0)$ with radius $|T|$ (called S henceforth) and the sphere with radius 2σ centered in $-\boldsymbol{X}$ (called C henceforth). Clearly, the integral will be 0 whenever there is no part of the shell S inside the Sphere C. Thus we need to carefully evaluate the integral depending upon whether S is partially or completely inside C.

Let us first consider the case when $|T| \geq 2\sigma$. In picture A.4 we represent this situation:

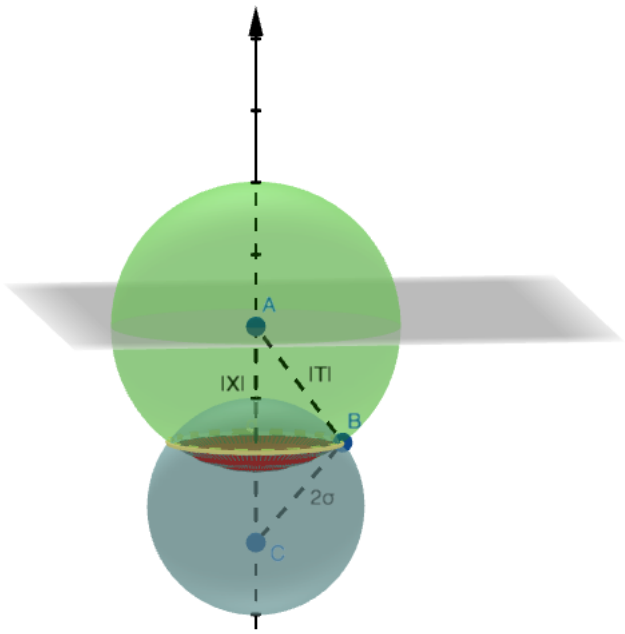

Figure A.4: Auxiliary schematic
The origin of coordinates is the point A and the axis represented is axis z. We have the original volume of integration, the blue sphere. Since we have the term $\delta(r - |T|)$ we see that the integration area will only be the the red one.

Looking at the picture it is evident that this integral is non-trivial iff $|T| - 2\sigma \leq |\boldsymbol{x}| \leq$

$|T|+2\sigma$. Otherwise, S is either completely outside C or engulfs C. Either way, there is no part of S inside C. However, when this condition is satisfied, there is a partial intersection between S and C. The integral, taking the Dirac delta, and considering the symmetry in the x-z axis, thus becomes:

$$\xi_{ij} = \tilde{\lambda}_i\tilde{\lambda}_j\frac{3T\sqrt{2\pi}}{4\sigma^3}\times \tag{A.82}$$

$$\int_{\theta_0}^{\theta_1=\pi} \mathrm{d}\theta\sin\theta\left(1-\frac{\sqrt{|T|^2+2|T||\boldsymbol{X}|\cos\theta+|\boldsymbol{X}|^2}}{2\sigma}\right)^2\left(2+\frac{\sqrt{|T|^2+2|T||\boldsymbol{X}|\cos\theta+|\boldsymbol{X}|^2}}{2\sigma}\right), \tag{A.83}$$

where $\cos\theta_0 = \cos(\pi - \angle BAC) = -\cos(\angle BAC) = \dfrac{4\sigma^2 - |\boldsymbol{X}|^2 - |T|^2}{2|\boldsymbol{X}||T|}$. Choosing now the change of coordinates $\epsilon = \frac{|T|^2+2|T||\boldsymbol{X}|\cos\theta+|\boldsymbol{X}|^2}{4\sigma^2}$ we obtain

$$\mathrm{d}\epsilon = \frac{-2|T||\boldsymbol{X}|\sin\theta}{4\sigma^2}\mathrm{d}\theta, \tag{A.84}$$

$$\theta_0 \to \epsilon_0 = 1, \tag{A.85}$$

$$\theta_1 \to \delta_- = \left(\frac{|\boldsymbol{X}|-|T|}{2\sigma}\right)^2. \tag{A.86}$$

We obtain then

$$\begin{aligned}\xi_{ij} &= -\tilde{\lambda}_i\tilde{\lambda}_j\frac{3\sqrt{2\pi}}{2\sigma|\boldsymbol{X}|}\int_1^{\delta_-} d\epsilon(1-\epsilon^{1/2})^2(2+\epsilon^{1/2}) = \frac{4\pi\sigma^2}{|\boldsymbol{X}|}(2\epsilon - 2\epsilon^{3/2} + \frac{2}{5}\epsilon^{5/2})\Big|_{\delta_-}^1 \\ \implies \xi_{ij} &= \lambda_i\lambda_j\frac{3\sqrt{2\pi}}{\sigma|\boldsymbol{X}|}(\frac{1}{5} - \delta_- + \delta_-^{3/2} - \frac{1}{5}\delta_-^{5/2}),\end{aligned} \tag{A.87}$$

where we recall that $\delta_- = \left(\frac{|\boldsymbol{X}|-|T|}{2\sigma}\right)^2$.

Now we consider the case when $|T| < 2\sigma$. When $2\sigma - |T| \leq |\boldsymbol{x}| \leq |T| + 2\sigma$, there is a partial intersection between S and C. Thus the calculations in the previous case hold exactly in the same fashion. Now, when $|\boldsymbol{x}| < 2\sigma - |T|$, S is completely engulfed by C. For this case we need to evaluate the integral in (A.82), within the limits 0 to π. Thus ξ_{ij} for this case turns out to be

$$\xi_{ij} = \tilde{\lambda}_i\tilde{\lambda}_j\frac{3\sqrt{2\pi}}{\sigma|\boldsymbol{X}|}(\delta_+ - \delta_+^{3/2} + \frac{1}{5}\delta_+^{5/2} - \delta_- + \delta_-^{3/2} - \frac{1}{5}\delta_-^{5/2}), \tag{A.88}$$

where $\delta_- = \left(\frac{|\boldsymbol{X}|-|T|}{2\sigma}\right)^2$ and $\delta_+ = \left(\frac{|\boldsymbol{X}|+|T|}{2\sigma}\right)^2$.

A.5.2 How to generate moments for a non-Gaussian state

In order to generate moments non-Gaussian states we need to do the following:

1. Calculate the distributions of the discussed sample means, sample second moments, and sample fourth moments (non centered) are selected from.
2. By central limit theorem these sample statistics distributions are determined by the first eight moments of the underlying distribution (the marginals of the final probe state Wigner function).
3. Using parts Gaussian formalism, these final probe moments are given by a symplectic transformation of the initial probe-field moments.
4. The moments of the initial probe-field state are simple (but not Gaussian).

We will discuss these tasks in reverse order.

The initial probe-field Wigner function is

$$W(q_{\rm D}, p_{\rm D}, q_1, p_1, q_2, p_2, \ldots; N) = W_{\rm Vac}(q_{\rm D}, p_{\rm D}) \times (W_{\rm Fock}(q_1, p_1; N)) \times \Pi_{n=2}^{\infty} W_{\rm Vac}(q_n, p_n) \tag{A.89}$$

or

$$W(q_{\rm D}, p_{\rm D}, q_1, p_1, q_2, p_2, \ldots; N) = W_{\rm Vac}(q_{\rm D}, p_{\rm D}) \times W_{\rm PAC}(q_1, p_1; N) \times \Pi_{n=2}^{\infty} W_{\rm Vac}(q_n, p_n) \tag{A.90}$$

where $q_{\rm D}$ and $p_{\rm D}$ are the probe variables and where $W_{\rm Vac}(q,p) = e^{-q^2-p^2}/\pi$. Note the probe and all of the modes are uncorrelated from each other. Thus all "cross moments" separate. For example as $\langle q_4 p_4^2 q_6^3 p_6^5\rangle = \langle q_4 p_4^2\rangle\langle q_6^3 p_6^5\rangle$. Note that these averages are taken w.r.t. the Wigner function, to translate operator averages to Wigner function averages you need to permute the operators into the right order.

The statistics of the vacuum Wigner function are

$$\langle q^2\rangle_{\rm Vac} = 1/2, \quad \langle q^4\rangle_{\rm Vac} = 3/4, \quad \langle q^6\rangle_{\rm Vac} = 15/8, \quad \langle q^8\rangle_{\rm Vac} = 105/16, \tag{A.91}$$

with $\langle p^n \rangle = \langle q^n \rangle$ and $\langle p^n q^m \rangle = \langle p^n \rangle \langle q^m \rangle$ and odd moments vanishing.

The statistics $(\langle q^0 \rangle_N,\ \langle q^2 \rangle_N,\ \langle q^4 \rangle_N,\ \langle q^6 \rangle_N,\ \langle q^8 \rangle_N)$ of the Fock state Wigner function are given by the following table:

$$\begin{pmatrix} N=0: & 1 & \frac{1}{2} & \frac{3}{4} & \frac{15}{8} & \frac{105}{16} \\ N=1: & 1 & \frac{3}{2} & \frac{15}{4} & \frac{105}{8} & \frac{945}{16} \\ N=2: & 1 & \frac{5}{2} & \frac{39}{4} & \frac{375}{8} & \frac{4305}{16} \\ N=3: & 1 & \frac{7}{2} & \frac{75}{4} & \frac{945}{8} & \frac{13545}{16} \\ N=4: & 1 & \frac{9}{2} & \frac{123}{4} & \frac{1935}{8} & \frac{33705}{16} \end{pmatrix} \tag{A.92}$$

with $\langle p^n \rangle = \langle q^n \rangle$ and $\langle p^n q^m \rangle = \langle p^n \rangle \langle q^m \rangle$ and odd moments vanishing.

The statistics $(\langle q^0 \rangle_N,\ \langle q^2 \rangle_N,\ \langle q^4 \rangle_N,\ \langle q^6 \rangle_N,\ \langle q^8 \rangle_N)$ of the Phase-Averaged Coherenet state Wigner function are given by the following table:

$$\begin{pmatrix} N=0: & 1 & \frac{1}{2} & \frac{3}{4} & \frac{15}{8} & \frac{105}{16} \\ N=1: & 1 & \frac{3}{2} & \frac{21}{4} & \frac{215}{8} & \frac{2835}{16} \\ N=2: & 1 & \frac{5}{2} & \frac{51}{4} & \frac{715}{8} & \frac{12425}{16} \\ N=3: & 1 & \frac{7}{2} & \frac{93}{4} & \frac{1635}{8} & \frac{34755}{16} \\ N=4: & 1 & \frac{9}{2} & \frac{147}{4} & \frac{3095}{8} & \frac{77385}{16} \end{pmatrix} \tag{A.93}$$

with $\langle p^n \rangle = \langle q^n \rangle$ and $\langle p^n q^m \rangle = \langle p^n \rangle \langle q^m \rangle$ and odd moments vanishing. Note that zeroth and second moments match (first and second column) as does the vaccuum state (first row).

Next let's see how to translate these moments of the initial field-probe state to the moments of the final probe state. The key insight for this step is that while the states are not Gaussian, the dynamics still is. The unitary for the interaction between the probe and the field is given in the interaction picture by

$$\hat{U}(t) = \hat{U}_{\text{int}}(t)\ \hat{U}_{\text{int}}(0) \tag{A.94}$$

where

$$\hat{U}_{\text{int}}(t) = \exp\left(-\mathrm{i}\lambda\ (\hat{q}_{\text{D}} \cos(\Omega t) + \hat{p}_{\text{D}} \sin(\Omega t)) \otimes \int \mathrm{d}\boldsymbol{x}\, F(\boldsymbol{x})\, \hat{\phi}(t, \boldsymbol{x})\right) \tag{A.95}$$

$$= \exp\left(-\mathrm{i}\lambda\ \frac{1}{2} \hat{\boldsymbol{X}}^{\intercal} \mathcal{H}(t) \hat{\boldsymbol{X}}\right). \tag{A.96}$$

where

$$\hat{\boldsymbol{X}} \coloneqq (\hat{q}_{\mathrm{D}}, \hat{p}_{\mathrm{D}}, \hat{q}_1, \hat{p}_1, \hat{q}_2, \hat{p}_2, \dots)^{\intercal}. \tag{A.97}$$

and

$$\mathcal{H}(t) = \boldsymbol{u}(t)\boldsymbol{v}(t)^{\intercal} + \boldsymbol{v}(t)\boldsymbol{u}(t)^{\intercal}; \tag{A.98}$$
$$\boldsymbol{u}(t) = (\cos(\Omega t), \sin(\Omega t), 0, 0, \dots)^{\intercal} \tag{A.99}$$
$$\boldsymbol{v}(t) = (0, 0, F_1 \cos(\omega_1 t), F_1 \sin(\omega_1 t), F_2 \cos(\omega_2 t), F_2 \sin(\omega_2 t), \dots)^{\intercal}. \tag{A.100}$$

where $F_n = \sqrt{2/L} \int \mathrm{d}x F(x) \sin(\omega_n x)$. Note that $\hat{U}_{\mathrm{int}}(t)$ is a Gaussian unitary transformation and therefore so too is $\hat{U}(t)$.

Gaussian unitary transformations correspond to symplectic transformations in phase space,

$$\hat{U}_{\mathrm{G}}^{\dagger} \hat{\boldsymbol{X}} \hat{U}_{\mathrm{G}} = S\hat{\boldsymbol{X}} + \boldsymbol{d}\hat{\mathbb{1}} \tag{A.101}$$

for some S with $S\Omega S^{\intercal} = \Omega$ where Ω is the symplectic form. Note that in the above equation $\hat{U}_{\mathrm{G}}$ is a linear map on the system's Hilbert space and acts on $\hat{\boldsymbol{X}}$ component-wise. On the other hand, S is a linear map on the system's phase space and acts on $\hat{\boldsymbol{X}}$ as a phase space vector, yielding linear combinations of its (operator-valued) components.

Note that this is true even when the state is non-Gaussian. The effect that a Gaussian unitary has on a state's Wigner function (even a non-Gaussian Wigner function) is,

$$\rho \to \hat{U}_{\mathrm{G}}\, \rho\, \hat{U}_{\mathrm{G}}^{\dagger} \quad \equiv \quad \hat{\boldsymbol{X}} \to \hat{U}_{\mathrm{G}}^{\dagger}\, \hat{\boldsymbol{X}}\, \hat{U}_{\mathrm{G}} = S\, \hat{\boldsymbol{X}} + \boldsymbol{d}\hat{\mathbb{1}} \quad \equiv \quad W(\boldsymbol{X}) \to W(S\boldsymbol{X} + \boldsymbol{d}). \tag{A.102}$$

Corresponding to the $U(t)$ given above we have

$$S(t) = S_{\mathrm{int}}(t)\, S_{\mathrm{int}}(0) \tag{A.103}$$

where

$$S_{\mathrm{int}}(t) = \exp(\lambda\, \Omega\, \mathcal{H}(t)). \tag{A.104}$$

This symplectic transformation is easy to compute. First note that $\Omega\mathcal{H}(t)$ is nilpotent,

that is, $(\Omega\mathcal{H}(t))^2 = 0$ since,

$$(\Omega\mathcal{H}(t))^2 = \Omega(\boldsymbol{u}(t)\boldsymbol{v}(t)^\intercal + \boldsymbol{v}(t)\boldsymbol{u}(t)^\intercal)\Omega(\boldsymbol{u}(t)\boldsymbol{v}(t)^\intercal + \boldsymbol{v}(t)\boldsymbol{u}(t)^\intercal) \tag{A.105}$$

$$= \Omega(\boldsymbol{u}(t)\boldsymbol{v}(t)^\intercal\Omega\boldsymbol{u}(t)\boldsymbol{v}(t)^\intercal + \boldsymbol{v}(t)\boldsymbol{u}(t)^\intercal\Omega\boldsymbol{u}(t)\boldsymbol{v}(t)^\intercal + \boldsymbol{u}(t)\boldsymbol{v}(t)^\intercal\Omega\boldsymbol{v}(t)\boldsymbol{u}(t)^\intercal + \tag{A.106}$$

$$+ \boldsymbol{v}(t)\boldsymbol{u}(t)^\intercal\Omega\boldsymbol{v}(t)\boldsymbol{u}(t)^\intercal) = 0 \tag{A.107}$$

since

$$\boldsymbol{v}(t)^\intercal\Omega\boldsymbol{u}(t) = 0, \quad \boldsymbol{u}(t)^\intercal\Omega\boldsymbol{u}(t) = 0, \quad \boldsymbol{v}(t)^\intercal\Omega\boldsymbol{v}(t) = 0, \quad \boldsymbol{u}(t)^\intercal\Omega\boldsymbol{v}(t) = 0. \tag{A.108}$$

Since $\Omega\mathcal{H}(t)$ is nilpotent we have

$$S_{\text{int}}(t) = \mathbb{1} + \Omega\mathcal{H} \tag{A.109}$$

$$= \mathbb{1} + \lambda\,\Omega\,(\boldsymbol{u}(t)\boldsymbol{v}(t)^\intercal + \boldsymbol{v}(t)\boldsymbol{u}(t)^\intercal) \tag{A.110}$$

$$\tag{A.111}$$

and

$$S_{\text{int}}^{-1}(t) = \mathbb{1} - \Omega\mathcal{H} \tag{A.112}$$

$$= \mathbb{1} - \lambda\,\Omega\,(\boldsymbol{u}(t)\boldsymbol{v}(t)^\intercal + \boldsymbol{v}(t)\boldsymbol{u}(t)^\intercal). \tag{A.113}$$

As was discussed above these symplectic transformations are useful because they tell us how the Wigner function evolves. We can use this to determine the moments of the final probe distribution from the initial probe field moments. The probe's Wigner function after an interaction of duration t is,

$$W_{\text{D}}(q,p) = \int \mathrm{d}\boldsymbol{x}\, W(S(t)(q,p,\boldsymbol{x})) \tag{A.114}$$

$$\tag{A.115}$$

where $\boldsymbol{x} = (q_1, p_1, q_2, p_2)$ runs over all the field variables. We can extend the integral to be over all of phase space $\boldsymbol{X} = (q_{\text{D}}, p_{\text{D}}, q_1, p_1, q_2, p_2)$ by adding in delta functions as

$$W_{\text{D}}(q,p) = \int \mathrm{d}\boldsymbol{X}\delta(q - q_{\text{D}})\,\delta(p - p_{\text{D}})\,W(S(t)\boldsymbol{X})). \tag{A.116}$$

Next we define the vectors $\boldsymbol{q}_0 = (1,0,0,\dots)^\intercal$ and $\boldsymbol{p}_0 = (0,1,0,\dots)^\intercal$ such that $q_0 = \boldsymbol{q}_0^\intercal\boldsymbol{X}$

and $p_0 = \boldsymbol{p}_0^\intercal \boldsymbol{X}$. In this way we have

$$W_{\mathrm{D}}(q,p) = \int \mathrm{d}\boldsymbol{X} \delta(\boldsymbol{q}_0^\intercal \boldsymbol{X} - q)\, \delta(\boldsymbol{p}_0^\intercal \boldsymbol{X} - p)\, W(S(t)\boldsymbol{X})) \tag{A.117}$$

Finally we can do a change of coordinates $\boldsymbol{X} \to \boldsymbol{Y} = S(t)\boldsymbol{X}$. Note that $S(t)$ has determinant 1 so no Jacobian factor arises. Doing this change of variables we have,

$$W_{\mathrm{D}}(q,p) = \int \mathrm{d}\boldsymbol{Y} \delta(\boldsymbol{q}_0^\intercal\, S(t)^{-1}\boldsymbol{Y} - q)\, \delta(\boldsymbol{p}_0^\intercal\, S(t)^{-1}\boldsymbol{Y} - p)\, W(\boldsymbol{Y}). \tag{A.118}$$

Thus the probe's final Wigner function has been written in terms of the initial probe field Wigner function. We can use this to compute the moments of the final probe state. Let us first do the second moments before attempting the higher ones.

The second moments of $\hat{q}_{\mathrm{D}}$ in the final probe state is

$$\begin{aligned}
\langle \hat{q}_{\mathrm{D}}(t)^2 \rangle &= \int \mathrm{d}q \int \mathrm{d}p\; q^2\, W_{\mathrm{D}}(q,p) && \text{(A.119)}\\
&= \int \mathrm{d}q \int \mathrm{d}p\; q^2 \int \mathrm{d}\boldsymbol{Y} \delta(\boldsymbol{q}_0^\intercal\, S(t)^{-1}\boldsymbol{Y} - q)\, \delta(\boldsymbol{p}_0^\intercal\, S(t)^{-1}\boldsymbol{Y} - p)\, W(\boldsymbol{Y}) && \text{(A.120)}\\
&= \int \mathrm{d}\boldsymbol{Y} (\boldsymbol{q}_0^\intercal\, S(t)^{-1}\boldsymbol{Y})^2\; W(\boldsymbol{Y}) && \text{(A.121)}\\
&= \int \mathrm{d}\boldsymbol{Y}\; (\boldsymbol{q}_0^\intercal S(t)^{-\intercal}\boldsymbol{Y})(\boldsymbol{Y}^\intercal S(t)^{-1}\boldsymbol{q}_0)\; W(\boldsymbol{Y}) && \text{(A.122)}\\
&= \boldsymbol{q}_0^\intercal S(t)^{-\intercal} \left(\int \mathrm{d}\boldsymbol{Y}\; \boldsymbol{Y}\boldsymbol{Y}^\intercal\; W(\boldsymbol{Y}) \right) S(t)^{-1}\boldsymbol{q}_0 && \text{(A.123)}\\
&= \boldsymbol{q}_0^\intercal S(t)^{-\intercal} \sigma_0 S(t)^{-1}\boldsymbol{q}_0 && \text{(A.124)}\\
& && \text{(A.125)}
\end{aligned}$$

where σ_0 is the covariance matrix of the initial probe-field state. Note that the initial probe-field state is not Gaussian, but it still has a matrix of second moments. Similarly,

$$\langle \hat{p}_{\mathrm{D}}(t)^2 \rangle = \boldsymbol{p}_0^\intercal S(t)^{-\intercal} \sigma_0 S(t)^{-1}\boldsymbol{p}_0 \tag{A.126}$$

$$\langle \hat{r}_{\mathrm{D}}(t)^2 \rangle = \frac{1}{2}(\boldsymbol{q}_0 + \boldsymbol{p}_0)^\intercal S(t)^{-\intercal} \sigma_0 S(t)^{-1}(\boldsymbol{q}_0 + \boldsymbol{p}_0). \tag{A.127}$$

Thus we can determine the second moments of the final probe state from the second moments of the initial field-probe state. All we need to do this is 1) the initial covariance matrix, σ_0 which we can construct from the second moments discussed above, and 2)

the vectors $Q(t) \coloneqq S(t)^{-1}\boldsymbol{q}_0$ and $P(t) \coloneqq S(t)^{-1}\boldsymbol{p}_0$ which map onto $\boldsymbol{q}_0$ and $\boldsymbol{p}_0$ for each timepoint. We can compute these from our above discussion as well.

As for higher moments we can follow the next example,

$$\langle \hat{q}_{\mathrm{D}}(t)^4 \rangle = \int \mathrm{d}\boldsymbol{Y} (Q(t)^\intercal \boldsymbol{Y})^4 \; W(\boldsymbol{Y}) \tag{A.128}$$

$$= \int \mathrm{d}\boldsymbol{Y} (\sum_{\ell=0}^{\infty} Q_\ell(t)\, y_\ell)^4 \; W(\boldsymbol{Y}) \tag{A.129}$$

$$= \int \mathrm{d}\boldsymbol{Y} \sum_{i,j,k,\ell=0}^{\infty} Q_i(t)\, Q_j(t)\, Q_k(t)\, Q_\ell(t)\, y_i\, y_j\, y_k\, y_\ell\, W(\boldsymbol{Y}) \tag{A.130}$$

$$= \sum_{i,j,k,\ell=0}^{\infty} Q_i(t)\, Q_j(t)\, Q_k(t)\, Q_\ell(t) \int \mathrm{d}\boldsymbol{Y} y_i\, y_j\, y_k\, y_\ell\, W(\boldsymbol{Y}) \tag{A.131}$$

$$= \sum_{i,j,k,\ell=0}^{\infty} Q_i(t)\, Q_j(t)\, Q_k(t)\, Q_\ell(t)\, S_{4,i,j,k,\ell} \tag{A.132}$$

$$= S_4(Q(t), Q(t), Q(t), Q(t)) \tag{A.133}$$

where $S_{4,i,j,k,\ell} = \int \mathrm{d}\boldsymbol{Y} y_i\, y_j\, y_k\, y_\ell\, W(\boldsymbol{Y}) = \langle y_i\, y_j\, y_k\, y_\ell \rangle$ are the entries of the four tensor S_4. Similarly,

$$\langle \hat{p}_{\mathrm{D}}(t)^4 \rangle = S_4(P(t), P(t), P(t), P(t)) \tag{A.134}$$

$$\langle \hat{r}_{\mathrm{D}}(t)^4 \rangle = \frac{1}{4} S_4(Q(t)+P(t), Q(t)+P(t), Q(t)+P(t), Q(t)+P(t)). \tag{A.135}$$

For the eighth moment, we have the formula

$$\langle \hat{q}_{\mathrm{D}}(t)^8 \rangle = \int \mathrm{d}\boldsymbol{Y} (Q(t)^\intercal \boldsymbol{Y})^8 \; W(\boldsymbol{Y}) \tag{A.136}$$

$$= \sum_{i,j,k,\ell,m,n,o,p=0}^{\infty} Q_i(t)\, Q_j(t)\, Q_k(t)\, Q_\ell(t)\; Q_m(t)\, Q_n(t)\, Q_o(t)\, Q_p(t)\, S_{8,i,j,k,\ell,m,n,o,p} \tag{A.137}$$

$$= S_8(Q(t), Q(t), Q(t), Q(t), Q(t), Q(t), Q(t), Q(t)) \tag{A.138}$$

where $S_{8,i,j,k,\ell,m,n,o,p} = \int \mathrm{d}\boldsymbol{Y} y_i\, y_j\, y_k\, y_\ell\, y_m\, y_n\, y_o\, y_p\, W(\boldsymbol{Y}) = \langle y_i\, y_j\, y_k\, y_\ell\, y_m\, y_n\, y_o\, y_p \rangle$ are the

entries of the four tensor S_8. Similarly,

$$\langle \hat{p}_{\mathrm{D}}(t)^8 \rangle = S_8(P(t), P(t), P(t), P(t), P(t), P(t), P(t), P(t)) \tag{A.139}$$

$$\langle \hat{r}_{\mathrm{D}}(t)^8 \rangle = \frac{1}{4} S_8(R(t), R(t), R(t), R(t), R(t), R(t), R(t), R(t)). \tag{A.140}$$

where $R(t) = Q(t) + P(t)$. Finally, we can determine the distributions to draw the sample mean, sample variance and sample fourth moments according to the following to the following formula for the central limit theorem in the high tomography limit

$$\bar{x^k} \sim \mu_k + \frac{1}{\sqrt{N}} \mathcal{N}(0, \mu_{2k} - \mu_k^2) \tag{A.141}$$

where $\mu_k = \langle \hat{x}^k \rangle$